

# Detailed models of interacting short-period massive binary stars

K. Sen<sup>1,2</sup> \*, N. Langer<sup>1,2</sup>, P. Marchant<sup>3</sup>, A. Menon<sup>1,4</sup>, S. E. de Mink<sup>5,4,6</sup>, A. Schootemeijer<sup>1</sup>, C. Schürmann<sup>1,2</sup>, L. Mahy<sup>7</sup>, B. Hastings<sup>1,2</sup>, K. Nathaniel<sup>1</sup>, H. Sana<sup>3</sup>, C. Wang<sup>1,2</sup>, and X.T. Xu<sup>1,2</sup>

<sup>1</sup> Argelander-Institut für Astronomie, Universität Bonn, Auf dem Hügel 71, 53121 Bonn, Germany

<sup>2</sup> Max-Planck-Institut für Radioastronomie, Auf dem Hügel 69, 53121 Bonn, Germany

<sup>3</sup> Institute of Astronomy, KU Leuven, Celestijnenlaan 200D, 3001 Leuven, Belgium

<sup>4</sup> Astronomical Institute “Anton Pannekoek”, University of Amsterdam, Science Park 904, 1098 XH Amsterdam, The Netherlands

<sup>5</sup> Max Planck Institute for Astrophysics, Karl-Schwarzschild-Strasse 1, 85748 Garching, Germany

<sup>6</sup> Center for Astrophysics, Harvard-Smithsonian, 60 Garden Street, Cambridge, MA 02138, USA

<sup>7</sup> Royal Observatory of Belgium, Avenue circulaire/Ringlaan 3, B-1180 Brussels, Belgium

Received November 3, 2021 / Accepted December 6, 2021

## ABSTRACT

**Context.** The majority of massive stars are part of binary systems. In about a quarter of these, the companions are so close that mass transfer occurs while they undergo core hydrogen burning, first on the thermal and then on the nuclear timescale. The nuclear timescale mass transfer leads to observational counterparts: the semi-detached so-called massive Algol binaries. These systems may provide urgently needed tests of the physics of mass transfer. However, comprehensive model predictions for these systems are sparse.

**Aims.** We use a large grid of detailed evolutionary models of short-period massive binaries and follow-up population synthesis calculations to derive probability distributions of the observable properties of massive Algons and their descendants.

**Methods.** Our results are based on  $\sim 10,000$  binary model sequences calculated with the stellar evolution code MESA, using a metallicity suitable for the Large Magellanic Cloud (LMC), covering initial donor masses between  $10 M_{\odot}$  and  $40 M_{\odot}$  and initial orbital periods above 1.4 d. These models include internal differential rotation and magnetic angular momentum transport, non-conservative mass and angular momentum transfer between the binary components, and time-dependent tidal coupling.

**Results.** Our models imply  $\sim 30$ , or  $\sim 3\%$  of the  $\sim 1,000$ , core hydrogen burning O-star binaries in the LMC to be currently in the semi-detached phase. Our donor models are up to 25 times more luminous than single stars of an identical mass and effective temperature, which agrees with the observed Algons. A comparison of our models with the observed orbital periods and mass ratios implies rather conservative mass transfer in some systems, while a very inefficient one in others. This is generally well reproduced by our spin-dependent mass transfer algorithm, except for the lowest considered masses. The observations reflect the slow increase of the surface nitrogen enrichment of the donors during the semi-detached phase all the way to CNO equilibrium. We also investigate the properties of our models after core hydrogen depletion of the donor star, when these models correspond to Wolf-Rayet or helium+OB star binaries.

**Conclusions.** A dedicated spectroscopic survey of massive Algol systems may allow to derive the dependence of the efficiency of thermal timescale mass transfer on the binary parameters, as well as the efficiency of semiconvective mixing in the stellar interior. This would be a crucial step towards reliable binary models up to the formation of supernovae and compact objects.

**Key words.** stars: massive – stars: evolution – binaries: close – Stars: abundances – Stars: statistics

## 1. Introduction

In the last two decades, it has been well established that massive stars are preferentially born as members of binary or multiple systems (Vanbeveren et al. 1998; Sana et al. 2012, 2013; Kobulnicky et al. 2014; Moe & Di Stefano 2017; Banyard et al. 2021). Hence, the study of their evolution is complicated by the fact that they can interact with their companion, which can significantly alter their properties and lead to observable characteristics that differ largely from those obtained from single stars (Podsiadlowski et al. 1992; de Mink et al. 2013; Wang et al. 2020). This complexity makes the modelling of massive binary star evolution challenging, and many aspects of it are not yet well understood (Langer 2012; Crowther 2019).

Since stars tend to expand with age, mass transfer via a Roche-lobe overflow occurs naturally in many close binaries. In the tightest binaries, mass transfer may occur while both stars are

still undergoing core hydrogen burning (Pols 1994; Vanbeveren et al. 1998; Wellstein et al. 2001; de Mink et al. 2007), initiating the so-called Case A mass transfer phase. Case A mass transfer is unique in the sense that it comprises a nuclear timescale mass transfer stage, and it has the massive Algol systems (or contact systems, see Menon et al. 2021) as observational counterparts, where the currently less massive, Roche-lobe filling star is transferring mass to a more massive star in a semi-detached configuration. Mass transfer in massive binaries otherwise (with rare exceptions, such as in Quast et al. 2019) occurs on the much shorter thermal or even dynamical timescale, and it is much less likely to be observed.

In Case A binaries, mass transfer first occurs on the thermal timescale of the donor star in a shrinking binary orbit. After the mass ratio is inverted, the orbit widens as a consequence of mass and angular momentum transfer. Thence, the mass transfer is driven by the slow expansion of the donor star due to core hydrogen burning. This gives rise to the nuclear timescale semi-detached phase, known as the slow Case A

\* email:ksen@astro.uni-bonn.de

mass transfer, with a duration of a considerable fraction of the lifetime of the binary. Since all binaries in this phase previously experienced an intense phase of thermal timescale mass transfer (fast Case A), comparing models with observed semi-detached massive binaries is not only constraining the observable slow mass transfer phase, but also the much less understood thermal timescale mass transfer.

Case A evolution has likely preceded most of the observed short period massive Wolf-Rayet+OB star binaries (Massey 1981; Niemela & Moffat 1982; van der Hucht 2001; Petrovic et al. 2005) and massive black hole binaries such as Cygnus X-1, LMC-X1, and M33 X-7 (Valsecchi et al. 2010; Qin et al. 2019; Langer et al. 2020). Recently, Quast et al. (2019) have shown that nuclear timescale mass transfer can also occur in supergiant X-ray binaries (see also Pavlovskii et al. 2017; Marchant et al. 2021). The short period of many of these post main sequence systems (Walter et al. 2015) implies that many of them evolved previously through Case A mass transfer.

Massive Case A binaries are also thought to contribute to the double neutron star and double black hole binaries population in the Universe (e.g. Kruckow et al. 2018). At low metallicity (less than one-tenth of Solar) and high mass (above  $40 M_{\odot}$ ) however, chemically homogeneous evolution may prevent expansion and mass transfer in short period binaries (de Mink et al. 2009; Marchant et al. 2016; Mandel & de Mink 2016; Hastings et al. 2020), potentially leading to BH mergers observable by gravitational waves (Abbott et al. 2019).

Modern observations of massive star binaries allow to determine the binary and stellar properties of individual systems in great detail (Hilditch et al. 2005; Torres et al. 2010; Martins et al. 2017; Pavlovski et al. 2018; Johnston et al. 2019; Mahy et al. 2020a,b; Janssens et al. 2021). This provides ideal conditions to constrain the uncertain physics assumptions in binary evolution models (Ritchie et al. 2010; Clark et al. 2014; Abdul-Masih et al. 2019). In particular, semi-detached double-lined systems provide a unique opportunity to derive the basic stellar properties of binaries with unprecedented precision, which can be used to test our models of stellar and binary evolution (Pols et al. 1997; Nelson & Eggleton 2001; de Mink et al. 2007, 2009).

Massive binaries with initial orbital periods below roughly 10 d undergo Case A evolution. Based on the period distribution of massive binaries obtained by Sana et al. (2012), this implies that about one quarter of all massive binaries will follow this path. Unfortunately, rapid binary evolutionary codes such as BSE (Binary Star Evolution, Hurley et al. 2002), Binary\_C (Izzard et al. 2006), StarTrack (Belczynski et al. 2008), COMPAS (Compact Object Mergers: Population Astrophysics and Statistics, Stevenson et al. 2017), ComBinE (Kruckow et al. 2018), MOBSE (Massive Objects in Binary Stellar Evolution, Giacobbo et al. 2018), SEVN (Stellar EVolution for N-body, Spera et al. 2019) and COSMIC (Compact Object Synthesis and Monte Carlo Investigation Code, Breivik et al. 2020) can treat Case A evolution only rudimentarily, since the above codes are based on single stars models, and on models of helium stars. However, the internal structure of mass donors in Case A binary models differs largely from both. Our detailed binary models include internal differential rotation and magnetic angular momentum transport in the individual stars, non-conservative mass and angular momentum transfer between the binary components, and time-dependent tidal coupling.

Previous studies of the Case A mass transfer phase of massive binaries based on detailed binary evolution grids identified stellar binary models that can provide a good fit to the

individual observed Algol binary systems (Nelson & Eggleton 2001), and constrain the underlying physics such as mass transfer efficiency as a function of the initial binary parameters (de Mink et al. 2007). The binary models of Eldridge et al. (2017, BPASS- Binary Population and Spectral Synthesis) also include Case A evolution. However, in their models the mass gainers are computed after the calculation of the evolution of the donor stars. Details of the Case A phase are not discussed.

A detailed study of the expected observable characteristics of this phase is lacking in the literature. Others studies on the Case A mass transfer phase focussed on low and intermediate mass stars (Mennekens & Vanbeveren 2017; Negu & Tessema 2018), where evidence for non-conservative mass transfer was found. In this work, we aim to provide a bridge between theory and observations by studying a grid of detailed binary evolution models and providing distributions of observable properties of massive binaries in this stage, that is, the slow Case A mass transfer phase.

For binaries having shorter initial orbital periods, the accretors can also fill their Roche lobes during the slow Case A mass transfer phase, and reach a contact configuration (Pols 1994; Wellstein et al. 2001), with the possibility of starting inverse mass transfer back to the donor while both components are burning hydrogen at their cores. Evolution during the contact phase is investigated in Menon et al. (2021). Our study focusses on the semi-detached configuration during the Case A mass transfer phase.

Section 2 gives a brief overview of the grid of detailed stellar evolution models and important physics assumptions. Section 3 describes the typical evolution of a Case A model and the mass transfer efficiency in our grid of models. Section 4 describes the observable distributions of stellar parameters during the slow Case A mass transfer phase obtained from the binary model grid. The properties of our Case A models after core hydrogen depletion is reported in Sect. 5. We compare our model predictions with the observed massive Algol binaries in the Large Magellanic Cloud (LMC) and the Milky Way in Sect. 6. In Sect. 7, we compare our work with relevant studies in the literature. We then briefly summarise our results and present our take-home messages in Sect. 8.

## 2. Method

### 2.1. The detailed binary evolution grid

To study the properties of Case A mass transfer, we use a dense grid of detailed massive binary evolution models (Marchant 2017) with an initial metallicity and composition representative of young star-forming regions in the LMC. The models were calculated using the 1D stellar evolution code MESA<sup>1</sup> (Modules for Experiments in Stellar Astrophysics, Paxton et al. 2011, 2013, 2015, 2018, version 8845<sup>2</sup>). The stellar and binary physics assumptions are described in detail by Paxton et al. (2015) and Marchant (2017). The most important and relevant ones are discussed in the following paragraphs.

The chemical composition and wind mass loss rates are set as in Brott et al. (2011a): the hydrogen, helium and metal mass fractions used in our models are 0.7391, 0.2562 and 0.0047 respectively. The initial abundances (in units of  $12 + \log(\text{element}/\text{H})$ ) for C, N, O, Mg, Si, Fe adopted are 7.75,

<sup>1</sup> <http://mesa.sourceforge.net/>

<sup>2</sup> Inlists to reproduce the models used in this work can be downloaded from [github.com/orlox/mesa\\_input\\_data/tree/master/2016\\_binary\\_models](https://github.com/orlox/mesa_input_data/tree/master/2016_binary_models)

6.90, 8.35, 7.05, 7.20 and 7.05 respectively. All other elements are solar abundances (Asplund et al. 2005) scaled down by 0.4 dex. The physics of differential rotation and rotational mixing follows that of Heger et al. (2000) while the magnetic angular momentum transport is as in Heger et al. (2005). The mass transfer rates are calculated following Marchant et al. (2016). When only one component of the binary overflows its Roche lobe, the mass transfer rate from the Roche lobe filling star is implicitly calculated so as to make the star just fill its Roche lobe. When both components of the binary fill their Roche lobes, the contact phase is calculated as described in Sect. 2.2 of the same work.

The accretion of angular momentum from the transferred matter follows the implementation of de Mink et al. (2013), which is based on the results of Lubow & Shu (1975) and Ulrich & Burger (1976). A differentiation between disc and ballistic modes of accretion during the mass transfer phases is considered. To determine which mode of accretion occurs, we compare the minimum distance of approach of the accretion stream (Lubow & Shu 1975; Ulrich & Burger 1976)

$$R_{\min} = 0.0425a \left( \frac{M_a}{M_d} + \frac{M_a^2}{M_d^2} \right)^{1/4} \quad (1)$$

to the radius of the accretor star ( $R_a$ ). Here,  $a$  is the orbital separation,  $M_d$  and  $M_a$  are the masses of the initially more massive donor star and initially less massive accretor star respectively. Accretion is assumed to be ballistic when  $R_a > R_{\min}$ , with a specific angular momentum of  $(1.7GM_a R_{\min})^{1/2}$ . Otherwise, accretion is assumed via a Keplerian disc with a specific angular momentum of  $(GM_a R_a)^{1/2}$ .

Equation 1 can be written in terms of orbital period, mass ratio and the mass of the accretor. We find that for an accretion disc to form, the orbital period of the binary during the mass transfer phase has to be longer than 20 d, for a  $10 M_{\odot}$  accretor when assuming a typical mass-radius relation (Gorda & Svechnikov 1998) to estimate the accretor radius. Hence, our Case A models are not expected to form an accretion disc during the slow Case A mass transfer phase. On the other hand, there are some observed Algol binaries that have an accretion disc (Table 2). Investigation into this discrepancy will be interesting, though beyond the scope of our present work.

The rotation periods of both components of the binary are assumed to be synchronised to the orbital period at their zero-age main sequence (ZAMS). Tidal interactions are modelled in a time-dependent fashion following the implementation by Detmers et al. (2008), using a synchronization timescale associated with the dynamical tide model of Zahn (1977), as appropriate for main sequence stars with radiative envelopes.

We use the standard Mixing Length Theory (Böhm-Vitense 1960) to model convection, with a mixing length parameter of  $\alpha_{\text{MLT}} = 1.5$ . The treatment of semiconvection follows Langer (1991) using  $\alpha_{\text{SC}} = 0.01$  and the physics of thermohaline mixing is as in Cantiello & Langer (2010). We implement overshooting as a step function only to the top of the convective core up to 0.335 times the pressure scale height (Brott et al. 2011a). However, overshooting is applied only to layers inside a star which have a near-constant composition (Marchant 2017), implying that composition gradients are taken into account during the rejuvenation process of mass gaining stars (Braun & Langer 1995). The initial composition of the binary models also takes into account the nonsolar abundance ratios of the LMC, as in Brott et al. (2011a). Unlike Brott et al. (2011a) however, we

use custom made OPAL opacity tables (Iglesias & Rogers 1996) in agreement with the initial abundance ratios of the LMC.

The initial donor mass ( $M_d$ ) of the binary models range from 10.0 to 39.8  $M_{\odot}$  in steps of  $\log(M_d/M_{\odot}) = 0.05$ , where the donor star in a binary model is the initially more massive star. The accretor ( $M_a$ ) is the initially less massive star of the model. For every initial mass of the donor, models with different initial mass ratio (defined as  $q = M_a/M_d$ ) ranging from 0.275 to 0.975 (in steps of 0.025) and initial orbital period ( $P_i$ ) from  $\sim 1.41$  d ( $\log P/d = 0.150$ ) to  $\sim 3165$  d ( $\log P/d = 3.500$ ), in steps of  $\Delta \log P_i/d = 0.025$ , are calculated. This current work deals with the properties of models in the grid undergoing Case A mass transfer.

The models are evolved from the start of hydrogen burning and the orbit is assumed to be circular. The spin axes are assumed to be aligned to the orbital axis. This avoids the introduction of six free parameters at ZAMS, namely the initial rotation rates of each component. Admittedly, this assumption has no physical justification in nature, but it has been shown that moderate rotation does not significantly affect the evolution of individual stars (Brott et al. 2011a; Choi et al. 2016) while the fastest rotating stars may be products of binary evolution (de Mink et al. 2013; Wang et al. 2020). More importantly, the initially short-period binary models, that is, most of the Case A models we are dealing with in our study, get tidally locked soon after the beginning of the evolution from ZAMS (de Mink et al. 2009), irrespective of their initial individual stellar spin and direction. The spins of the post Case A models investigated here are influenced by the mass transfer episode where the mass donor fills its Roche volume and the mass gainer is typically spun up due to mass accretion. For similar reasons, the assumption of a circular orbit is not expected to affect our results significantly as our work is focussed on the properties of short-period binaries.

Mass transfer in the binary models is assumed to be conservative except for stellar winds until the accreting star spins up to critical rotation during the mass transfer process. However, Packet (1981) showed that stars only need to accrete a few percent of their total mass to spin up to critical rotation. Further accretion of matter is not possible unless angular momentum is lost by some mechanism. To model this loss of angular momentum when accretors reach critical rotation, the wind mass-loss rate of the accretor is increased to keep  $v_{\text{rot}}/v_{\text{crit}}$  near  $\sim 0.99$ , facilitating mass and angular momentum loss through the increased wind mass loss as described in Langer et al. (2003a) and Petrovic et al. (2005). The amount of specific angular momentum removed from the orbit by the enhanced wind is equal to the specific orbital angular momentum of the accretor. At the same time, we remove the product of the specific spin angular momentum of the accretor at its surface times the mass removed from the system from the spin angular momentum of the accretor (Paxton et al. 2015). Here,  $v_{\text{rot}}$  and  $v_{\text{crit}}$  are the rotational and critical rotational velocities of the star as defined in Langer (1997).

Typically, the models where tidal effects can prevent the rapid spin-up of the accreting star lead to efficient mass transfer (i.e. very short orbital period models). In contrast, longer period models have comparatively much lower mass transfer efficiency. The efficiency of mass transfer is still an unsolved problem in binary evolution, with studies hinting at a decreasing efficiency with increasing orbital period (de Mink et al. 2007).

The assumption of increased mass-loss rates at close to critical rotation leads to a self-consistent way of determining the mass transfer efficiency, although it leads to very high mass-loss rates in models where tidal effects are unable to halt the

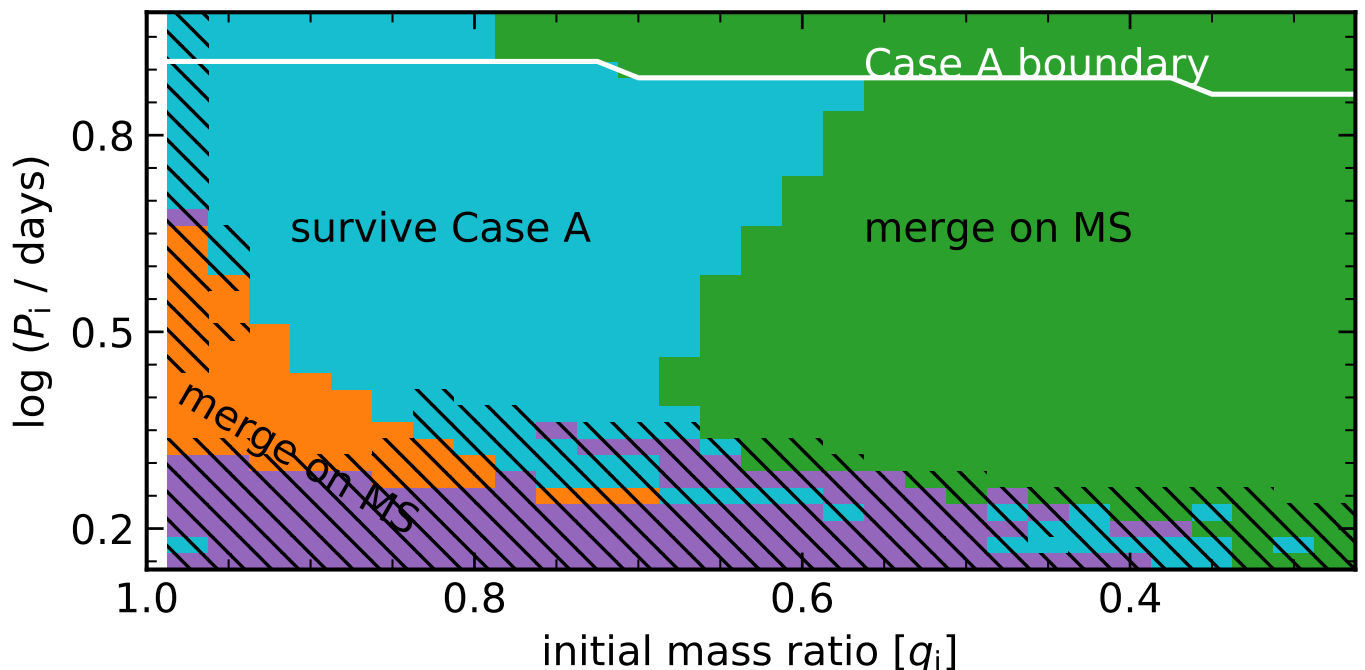


**Fig. 1.** Summary plot of binary models with an initial donor mass of  $22.4 M_{\odot}$ , as a function of the initial binary orbital period and mass ratio. Each pixel in the plot represent the outcome of one binary model with the corresponding orbital period and mass ratio. The white line shows the maximum initial orbital period below which models undergo Case A mass transfer. The light blue coloured models survive the Case A mass transfer phase. The models marked in green are terminated during the fast Case A mass transfer phase. The purple models undergo mass overflow from the L2 Lagrangian point during core hydrogen burning. The orange models undergo inverse mass transfer onto the initially more massive Roche-lobe filling star while it is burning hydrogen, from the initially less massive component that has completed core hydrogen burning. Models that enter into a contact configuration, at any point of time during their main sequence evolution, are marked with hatching.

rapid spin-up to critical rotation. To assess the feasibility of such high mass-loss rates in a model, an upper limit to the mass-loss rate ( $\dot{M}_{\text{upper}}$ ) is calculated. For a radiation-driven wind, the upper limit is found by assuming that the mass that has to be lost is removed from a Keplerian disc whose radius is at most equal to that of the Roche lobe radius of the mass accreting star (with mass  $M_a$ ). Ignoring the donor (with mass  $M_d$ ), the energy per unit mass (or gravitational potential) required to remove mass from the Roche lobe radius of the accretor is  $GM_a/R_{\text{RL},a}$ . Assuming that the luminosity of both stars ( $L_d$  and  $L_a$ ) is used to drive this mass loss, the resulting mass-loss rate is

$$\log \frac{\dot{M}_{\text{upper}}}{M_{\odot}/\text{yr}} = -7.19 + \log \frac{L_d + L_a}{L_{\odot}} - \log \frac{M_a}{M_{\odot}} + \log \frac{R_{\text{RL},a}}{R_{\odot}}. \quad (2)$$

For a typical model in our grid, having  $L_d$ ,  $L_a$ ,  $M_a$  and  $R_{\text{RL},a}$  of  $4570 L_{\odot}$ ,  $3631 L_{\odot}$ ,  $6.25 M_{\odot}$  and  $10 R_{\odot}$  respectively, the maximum mass loss rate ( $\dot{M}_{\text{upper}}$ ) is  $\sim 10^{-3} M_{\odot}/\text{yr}$ .

When the mass-loss rate required in the model exceeds this maximum value that can be powered by the photon energy of both stars, the evolution of the model is stopped. The evolution of contact binaries are modelled as in Marchant et al. (2016) and they are stopped if mass overflow occurs from the L2 Lagrangian point during the contact phase. We also stop the evolution of a model if inverse mass transfer occurs in a binary model with a post main sequence component. We assume that the mass transfer in such models will not be stable and will lead to a common envelope evolution and merge. Otherwise, models are evolved till core carbon exhaustion if they have helium core masses less than  $13 M_{\odot}$  at the end of core helium burning,

and till core helium depletion for models that have helium core mass greater than  $13 M_{\odot}$  (due to numerical issues faced in modelling the more massive stars all the way to core carbon depletion). Our study deals with the properties of binaries where both components are on the main sequence.

## 2.2. Initial binary distribution function

For our population synthesis predictions, each binary model  $m$  in our grid is assigned a weight factor  $W_m$  that depends on the initial donor mass  $M_d$ , the initial mass ratio  $q_i$  and the initial orbital period  $\log P_i$ . For the initial donor mass distribution, we use the Salpeter initial mass function (Salpeter 1955), and the Sana et al. (2012) exponents for the initial mass ratio and orbital period. While the latter have been derived using a modest sample of  $\sim 40$  O-type binaries in the Milky Way, more recent studies of O and B type stars both in the Milky Way and the LMC have failed to reveal any statistically significant differences (Sana et al. 2013; Dunstall et al. 2015; Villaseñor et al. 2021; Banyard et al. 2021). Hence, our adopted values can also be taken as representative of the OB star population at LMC metallicity. As such, we define  $W_m$  as

$$W_m = (\log M_{d,i}/M_{\odot})^{-1.35} * q_i^{-0.10} * (\log P_i/d)^{-0.55}. \quad (3)$$

We obtain histograms for the distribution of an observable  $O_{\text{obs}}$ , defined as the value of the stellar parameter during the contact (cnt) or semi-detached (SD) phase, weighing with the amount of time spent in the cnt or SD phase and the initial binary distribution functions. The number fraction ( $f_{\text{obs,cnt}}$  or  $f_{\text{obs,SD}}$ )

of an observable stellar parameter in a given bin with bin edges  $[O_1, O_2]$  is given by,

$$f_{\text{obs, cnt or SD}}(O_1 < O_{\text{obs}} < O_2) = \frac{\sum_{m=1}^N \delta_{O_1 O_2, m} W_m \Delta t_{\text{cnt or SD, m}}}{\sum_{m=1}^N W_m \Delta t_{\text{cnt or SD, m}}}, \quad (4)$$

where  $m$  is the model number of a particular model in our grid and  $N$  is the total number of models that undergo Case A mass transfer (Case A models).  $\Delta t_{\text{cnt or SD, m}}$  is the total time spent in the contact or semi-detached configuration by model  $m$ .  $\delta_{O_1 O_2, m}$  is equal to 1 when the value of the observable for the model  $m$  is between  $O_1$  and  $O_2$  during the contact or semi-detached phase and zero otherwise.

### 2.3. Binary parameter space

To help understand the general properties of the models undergoing Case A mass transfer and aid in the interpretation of the results of our population synthesis, we briefly describe a slice of our parameter space. Figure 1 shows the evolutionary outcomes up to core hydrogen depletion for models with an initial donor mass of  $22.4 M_{\odot}$  and different initial orbital periods and mass ratios. Models with  $\log(P_i/d) \lesssim 0.9$  undergo Case A mass transfer. The orbital period cut-off below which models undergo Case A mass transfer depends on the initial donor mass, with longer periods binaries able to undergo Case A mass transfer for higher initial donor masses (c.f. Fig. F.1).

Notably, we find by inspection that all our Case A accretors undergo ballistic mass accretion from the donors (see discussion of Eq. 1). We see that only a part of the parameter space survives the Case A mass transfer phase (marked by the lightblue colour). Models with low mass ratios (green) are terminated (and assumed to merge) during the fast Case A mass transfer phase because the combined luminosity of both of stars is insufficient to drive the excess mass-loss rate required to hinder over-critical rotation of the mass accretor, that is, the mass transfer rate in the model exceeds  $\dot{M}_{\text{upper}}$  (given by Eq. 2). They spend  $\sim 5000$  yrs in the fast Case A mass transfer phase before terminating and hence are not expected to significantly change the distribution of the observable properties of semi-detached binaries.

Models with very short orbital periods (purple) enter into a contact configuration during the slow Case A mass transfer and eventually experience L2 overflow. Such binaries are assumed to merge, due to the very low orbital periods. In the orange models, the initially less massive star overtakes the evolution of the mass donor during the slow Case A mass transfer phase and completes core hydrogen burning before the initially more massive star (Pols 1994; Wellstein et al. 2001). As such, a reverse mass transfer is initiated from initially less massive star (that is expanding rapidly after core hydrogen burning), on to the initially more massive Roche-lobe filling star that is still in its main sequence. This inverse mass transfer will likely be unstable and the binary is assumed to merge.

However, the above two types of models (purple and orange) spend up to  $\sim 10$  Myrs in the slow Case A mass transfer phase before they undergo L2 overflow. Hence, the contribution from these short period binaries to the observable properties of Algol binaries cannot be neglected. Similar figures for other initial donor masses are provided in the Appendix (Fig. F.1). Since the radii of more massive donor stars are larger, binaries can undergo Case A mass transfer at longer orbital periods for greater initial donor masses. Moreover, since the luminosity of

stars rises steeply with mass, the upper limit to the maximum mass transfer rate (Eq. 2) also increases for higher initial donor masses. Since this upper limit to the maximum mass transfer rate determines the boundary between systems that merge vs systems that survive the fast Case A mass transfer, more systems survive the Case A mass transfer at higher initial donor masses.

## 3. Case A mass transfer

### 3.1. A Typical example

Figure 2 shows the typical evolution of a short period ( $\sim 2.7$  d) massive binary with initial donor and accretor mass of  $17.80 M_{\odot}$  and  $14.24 M_{\odot}$ , respectively. It encounters mass transfer while both stars are burning hydrogen in their cores (Panel ‘a’). The initially more massive star fills its Roche lobe at  $\sim 9.4$  Myr which initiates mass transfer via Roche-lobe overflow (panel ‘b’). The mass transfer rate rises above  $10^{-4} M_{\odot} \text{yr}^{-1}$  (panel ‘d’) during the so-called fast Case A mass transfer phase which occurs at the thermal timescale of the donor. We see that in this model, the fast Case A mass transfer is not purely conservative as the accretor quickly spins up to critical rotation (evidenced by the sharp increase in the ratio of rotational velocity to synchronous velocity in Panel ‘g’). Only about 20% of the mass lost by the donor is accreted by the companion (Panel ‘c’). The orbital period (solid black line, panel ‘h’), and in turn the orbital separation, first decreases and then increases as the mass ratio gets inverted and keeps diverging from unity.

For comparison, we also show the evolution of the orbital period if the mass transfer was fully conservative (black dashed line). We compute the orbital period ( $P$ ) evolution in the conservative case following (Soberman et al. 1997)

$$\frac{P}{P_i} = \left( \frac{M_{d,i} M_{a,i}}{M_d M_a} \right)^3, \quad (5)$$

where  $P_i$ ,  $M_{d,i}$  and  $M_{a,i}$  are the initial orbital period of the binary, donor mass and accretor mass respectively.  $M_d$ ,  $M_a$  and  $P$  are the masses of the donor, the accretor, and the orbital period at any stage during the conservative mass transfer process. To compute the orbital period under the assumption of conservative mass transfer, we take  $M_d$  from our simulations and compute  $M_a$  assuming the mass transfer process was conservative. Since the mass transfer is non-conservative during the fast Case A phase in this model, the increase in orbital period due to the fast Case A mass transfer is lower than for the conservative mass transfer case.

Following the fast Case A mass transfer episode, the binary enters into a nuclear timescale mass transfer phase where the mass transfer rate is of the order of the nuclear timescale. This phase is known as the slow Case A phase, or the Algol phase (for a more detailed discussion, see Wellstein et al. 2001). In our work, we distinguish between the fast and slow Case A mass transfer phase based on the mass transfer rate in the binary, with the boundary at  $10^{-5} M_{\odot} \text{yr}^{-1}$ .

There is a gradual increase in the surface abundances of helium and nitrogen during the slow Case A phase (panels ‘e’ and ‘f’) as the mass transfer exposes the deeper layers of hydrogen burning processed material of the donor. We also note that most of the mass from the donor is lost during the fast Case A phase (panel ‘c’) and there is a slow loss and gain in mass of the donor and accretor respectively during the slow Case A phase. The amount of mass accreted depends on, amongst other factors, the spin-up of the accretor star in response to the mass accretion.

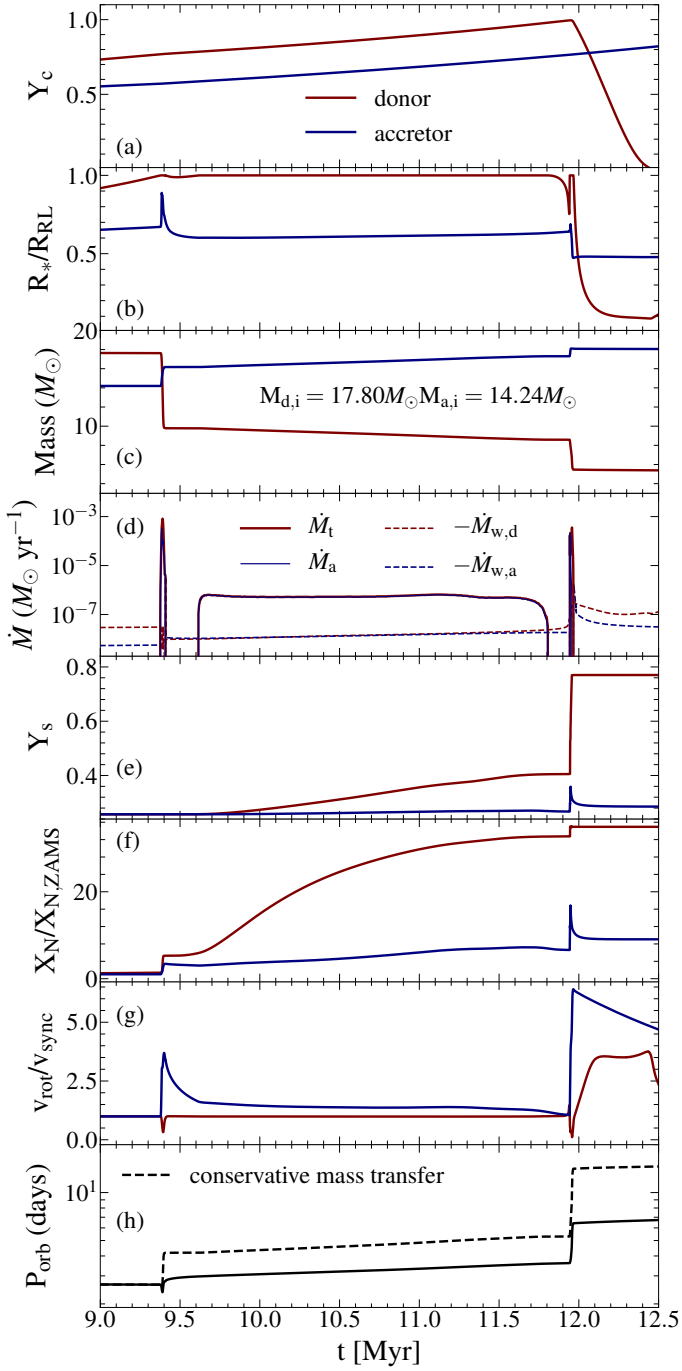


**Fig. 2.** Example of a Case A and Case AB mass transfer episode for a typical binary model in our grid. The initial donor mass, mass ratio and orbital period of the model are  $17.8 M_{\odot}$ ,  $0.8$  and  $\sim 2.7$  d respectively. Various quantities are plotted as function of time, with  $t = 0$  corresponding to the ZAMS stage of both stars. (a): Central helium mass fraction of donor (red) and accretor (blue). (b): Ratio of donor and accretor radius to their Roche lobe radii. (c): Donor and accretor mass. (d): Mass transfer rate  $\dot{M}_t$  (red solid line), effective mass accretion rate  $\dot{M}_a$  (blue solid line), and wind mass loss rates of donor ( $-\dot{M}_{w,d}$ , red dotted line) and accretor ( $-\dot{M}_{w,a}$ , blue dotted line), respectively. (e): Surface helium mass fraction. (f): Surface nitrogen enhancement factor. (g): Ratio of rotational to orbital angular velocity. (h): Orbital period (solid black line), and the orbital period our model would have obtained if the mass transfer would have been fully conservative (dashed black line).

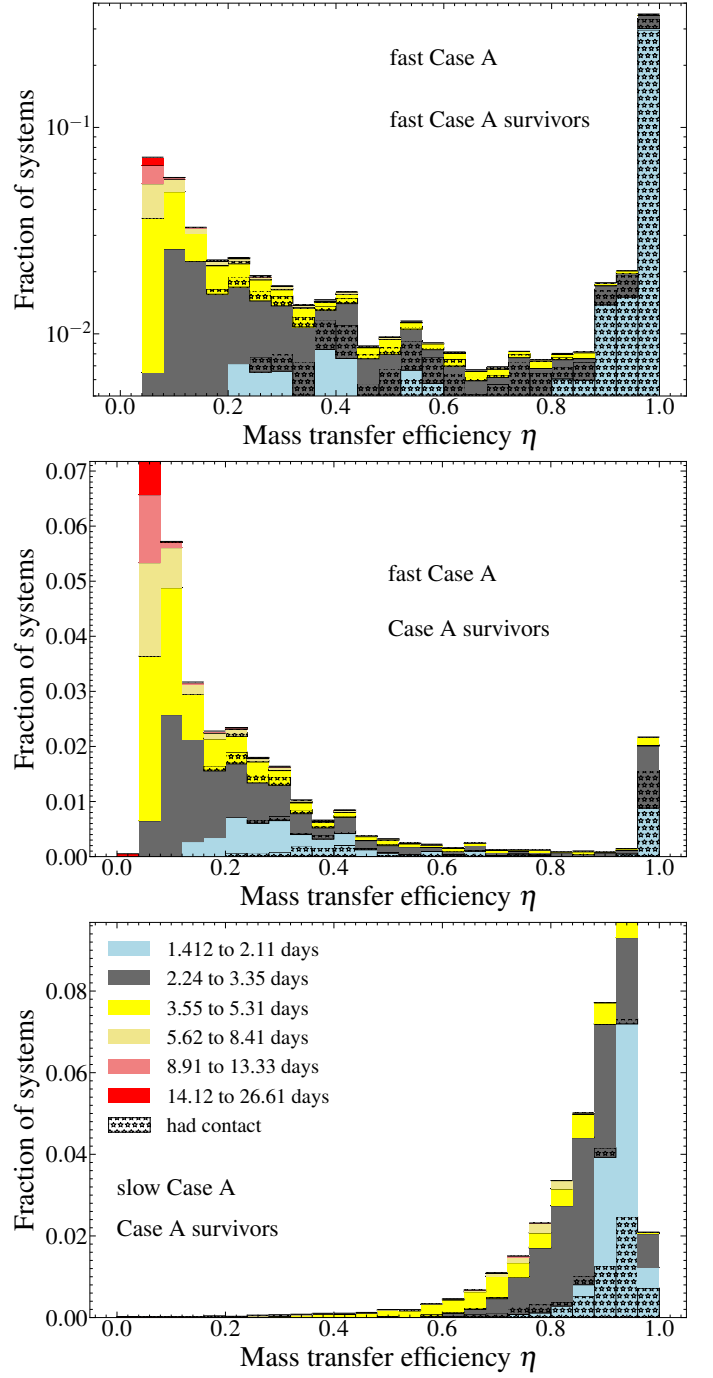


**Fig. 3.** Distribution of the time-averaged mass transfer efficiency during fast (top two panels) and slow (bottom panel) Case A mass transfer. The top plot includes all models that survive fast Case A mass transfer phase (i.e. light blue, orange and purple models in Fig. 1), while the middle panel includes only those models that survive also the slow Case A mass transfer phase (light blue models in Fig. 1). The colour coding is with respect to the initial orbital period of the binary model. The histograms are weighted with the birth probability of the binaries, and with the amount of time spent in the respective Case A mass transfer phase. The ordinate values are normalised to unity such that the value for each bin gives the weighted fraction of models that have their mass transfer efficiency between those bin edges during fast/slow Case A mass transfer. The fraction of models in any bin that undergo a contact phase are marked with star hatching.

At the end of core hydrogen exhaustion, the remaining hydrogen envelope in the mass donor starts to expand and refill its Roche lobe. This leads to the onset of another thermal timescale mass transfer phase, that is, the Case AB phase, where most of the remaining hydrogen envelope is removed from the mass donor and the surface nitrogen abundance reaches the CNO equilibrium value and the surface helium mass fraction reaches  $\sim 0.77$ . Since the mass ratio increasingly diverges away from unity to higher values, the orbital period of the binary also increases during this mass transfer phase.

We define Case A mass transfer to be occurring in our binary models when there is a non-zero mass transfer rate in the binary model and the Roche lobe filling star is still burning hydrogen at its centre. This means that, in addition to the fast and slow Case A phases, main sequence contact models and inverse mass transfer during core hydrogen burning from the initially less massive component to the initially more massive star will also be part of the Case A mass transfer phase. The corresponding configuration of a binary model where one star (both stars) fills its (their) Roche lobe(s) is called the semi-detached (contact) configuration.

One important point to keep in mind, however, is that for inverse slow Case A mass transfer from an initially less massive accretor, we do not change the notation of ‘donor’ and ‘accretor’ in our results. As such, we use the word ‘donor’ to denote the initially more massive star that fills its Roche lobe first, and ‘accretor’ to denote the initially less massive accretor star. Nevertheless, we point out whenever the contribution from inverse mass transfer binaries to the general population of slow Case A binaries is present.

### 3.2. Mass transfer efficiency in our models

Here, we define and analyse the mass transfer efficiency during the fast and slow Case A mass transfer in our binary models. To avoid misunderstandings, it needs to be carefully defined, since both binary components may also lose mass to a stellar wind. Notably, the mass transfer efficiency in our models is a function of time, and below, we evaluate their time-averaged mass transfer efficiency during fast and slow Case A mass transfer.

When we designate the donor’s wind mass-loss rate as  $\dot{M}_{w,d}$ , and the rate of mass transfer via Roche-lobe overflow as  $\dot{M}_t$ , the total mass-loss rate from the donor stars is

$$\dot{M}_d = \dot{M}_{w,d} - \dot{M}_t, \quad (6)$$

where we define the mass transfer rate as a positive quantity and wind mass loss rate as a negative quantity. During fast Case A mass transfer, it is  $\dot{M}_t \gg -\dot{M}_{w,d}$ , such that the wind mass-loss rate from the donor is insignificant (c.f., Panel ‘d’ of Fig. 2). During the slow Case A mass transfer phase however, wind mass loss and mass transfer rate can become comparable for the most massive donors in our grid. For a model with  $(M_{d,i}, P_i, q_i) = (39.8 M_\odot, 6.3 \text{ d}, 0.800)$ , we find that  $\sim 0.5 M_\odot$  of mass are lost from the donor via its stellar wind during the slow Case A mass transfer phase, while  $\sim 2 M_\odot$  of mass are transferred via the first Lagrangian point during the same time.

The mass change of the accretor is obtained by subtracting its wind mass loss from the amount transferred, that is,  $\dot{M}_a = \dot{M}_t + \dot{M}_{w,a}$ , where  $\dot{M}_a$  is the total rate of change of mass of the accretor and  $\dot{M}_{w,a}$  is the wind mass-loss rate of the accretor. Here, the steep increase in wind mass loss for accretors rotating near critical rotation can become important. As explained in

Sect. 2.1, this effect can lead to highly non-conservative mass transfer in our models, such that the term  $\dot{M}_{w,a}$  can exceed the wind mass-loss rate of slowly rotating models by orders of magnitude. This happens for spun-up mass gainers near critical rotation, where the mass loss which prevents it from rotating faster than critical. For fully spun-up accretors, it is  $\dot{M}_{w,a} \approx -\dot{M}_t$ .

As we model inefficient accretion like a stellar wind, we do not differentiate between the ordinary stellar wind and the mass loss required to prevent over-critical rotation in defining our mass transfer efficiency  $\eta$ , and set

$$\eta = \frac{\dot{M}_a}{\dot{M}_t}. \quad (7)$$

In this way, the mass transfer efficiency can range from 0 for critically rotating accretors to  $\sim 1$  for tidally locked and/or slowly rotating accretors.

Figure 3 shows the time-averaged mass transfer efficiencies during fast (top and middle panel) and slow Case A (bottom panel). The top panel shows the mass transfer efficiencies of all our systems that survive fast Case A mass transfer as a binary. It excludes models that we expect to merge very soon after the onset of the fast mass transfer (models marked in green in Fig. 1). We see that mass transfer efficiencies, from fully conservative to fully non-conservative are realised by our models. While the distribution is rather flat for most of the mass transfer efficiency range, it shows distinct peaks near  $\eta = 1$  and  $\eta = 0.05$ .

About  $\sim 35\%$  of our models undergo nearly conservative fast Case A mass transfer. The initial period information (colour coding in Fig. 3) reveals that this happens for the shortest period binaries in our model grid. These systems remain effectively tidally locked at all times, such that their accretors are not spun up. On the other hand, models with initial orbital periods larger than  $\sim 4 \text{ d}$  show mass transfer efficiencies below 40%, and the initially widest binaries evolve with accretion efficiencies below  $\sim 15\%$ . This reflects the decreasing strength of the tidal interaction for larger orbital separations.

The middle panel of Fig. 3 shows the mass transfer efficiency during fast Case A for models that also survive the slow Case A mass transfer phase without merging. Of these, we find that 99.2% also survive the ensuing Case AB mass transfer. Models in our grid that survive the entire Case A mass transfer typically have low average fast Case A mass transfer efficiencies. Comparing the top and middle panels, we see that a large number of models that undergo conservative fast Case A mass transfer merge during the slow Case A mass transfer phase. These models, originating from very short initial periods that eventually undergo L2 overflow, actually spend a considerable amount of time in the slow Case A mass transfer phase before merging (compare peak at mass transfer efficiency near unity between the left and right panel). We find that some of these models also go through a nuclear-timescale contact phase before merging (see also Menon et al. 2021). Quantitatively, the weighted fraction of Case A models contributing to the middle panel is  $\sim 63\%$  smaller than that in the top panel.

The time-averaged mass transfer efficiency during slow Case A mass transfer, for the models which survive the slow Case A (bottom panel of Fig. 3), is generally high. The slow Case A mass transfer occurs at the nuclear timescale and the mass transfer rate is also much lower, of the order of  $10^{-7} M_\odot/\text{yr}$ . For the model with  $(M_{d,i}, P_i, q_i) = (39.8 M_\odot, 6.3 \text{ d}, 0.800)$ , we find that  $\sim 0.3 M_\odot$  of mass are lost from the accretor via stellar winds during the slow Case A mass transfer phase. Hence, the mass accreted by the mass gainer during the slow Case A mass

transfer phase in this model is  $\sim 1.7 M_{\odot}$ . The mass transfer efficiency of this binary during slow Case A is about 85%. We show later that the majority of the accretors in the slow Case A phase are tidally synchronised. A comparison of time spent in the slow Case A phase between models that merge during the slow Case A phase vs models that survive the slow Case A phase reveals that our models predict  $\sim 70\%$  of Algols binaries are expected to merge during their main sequence.

Fig. F.2 shows the mass transfer efficiency of individual models in our grid for an initial donor mass of  $\sim 16 M_{\odot}$  and  $\sim 40 M_{\odot}$ . We see that the mass transfer efficiency of the thermal timescale fast Case A and Case AB phase is low for the most of the  $16 M_{\odot}$  models. Owing to the increased tidal strength of higher mass donors, the mass transfer efficiency is near unity for the shortest period models of the  $40 M_{\odot}$  slice. We also see the dividing boundary as a function of orbital period and mass ratio at which the tidal strength is unable to counteract the spin-up of the accretor star. A lot more number of models undergo conservative slow Case A mass transfer, owing to the nuclear timescale mass transfer rate. Nevertheless, we again see a reasonably clear boundary between efficient and nonefficient mass transfer in the slow Case A mass transfer phase too.

We note that the amount of mass lost and gained during the slow Case A phase can be up to  $\sim 6 M_{\odot}$  for the models (Fig. F.4) with an initial donor mass of  $40 M_{\odot}$ , due to efficient mass accretion during the slow Case A phase. Another  $\sim 4 M_{\odot}$  of mass can be lost during the Case AB mass transfer phase (Fig. F.5) in our models. Also, a very small number of models with highest initial donor masses can undergo efficient Case AB mass transfer.

### 3.3. Life-time of Case A mass transfer

Here, we look at the amount of time spent by the binary models in the Case A mass transfer phase. Figure 4 assesses the fraction of the main sequence lifetime our models spent in the Case A mass transfer phase,  $\tau_{\text{Case A}}$ , with the Case A mass transfer phase as defined in Sect. 3.1. Here, we define the main sequence lifetime ( $\tau_{\text{MS}}$ ) of a binary model as the hydrogen burning lifetime of the binary component which completes hydrogen burning first, or, for those binary models which merge during Case A evolution, the main sequence lifetime of a single star with half the total mass of the binary model. The number fraction  $f$  in each fractional main sequence ( $\tau_{\text{Case A}}/\tau_{\text{MS}}$ ) bin  $[a, b]$  is given as

$$f(a < \tau_{\text{Case A}}/\tau_{\text{MS}} < b) = \frac{\sum_{m=1}^N \delta_{\text{ab},m} W_m}{\sum_{m=1}^N W_m}, \quad (8)$$

where  $\delta_{\text{ab},m} = 1$  if the fraction of the main sequence lifetime spent by the model in Case A mass transfer phase is between  $a$  and  $b$ , and  $\delta_{\text{ab},m} = 0$  otherwise.

Figure 4 only includes models that spend more than 0.1% of their main sequence lifetime in the Case A mass transfer phase, which is of the order of the thermal timescale of the mass donors. This removes about 60% of all models that undergo Case A mass transfer, whose fate is to merge during fast mass transfer (green models in Fig. 1). Figure 4 shows that the shorter period binaries spend more time in the Case A mass transfer phase. Many of these models also go through a contact phase as denoted by the star hatching. The hatched versus unhatched part of each bin in this figure indicates the fraction of the models in any bin go through a contact phase, but is not indicative of the time spent in the respective phases.

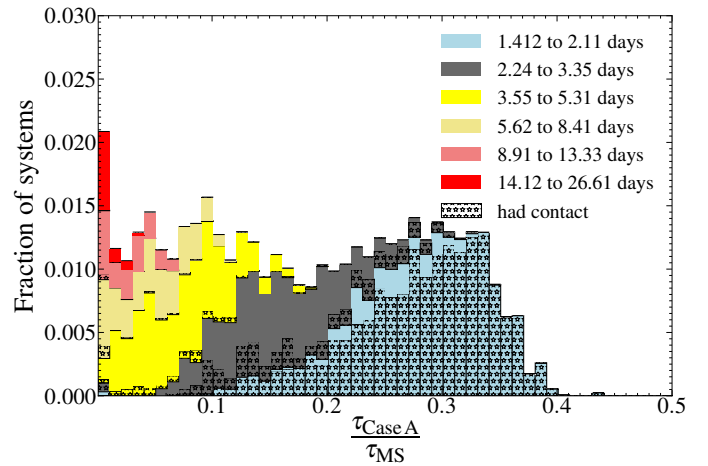


**Fig. 4.** Distribution of the fractional main sequence lifetime spent in the Case A mass transfer phase ( $\tau_{\text{Case A}}/\tau_{\text{MS}}$ ; see text for the exact definition) of models with  $\tau_{\text{Case A}}/\tau_{\text{MS}} > 0.001$ . The colour coding differentiates between models arising from different ranges of initial orbital periods. The star hatching in each fractional main sequence lifetime bin denotes the relative number fraction of models in that bin that go through a contact phase during Case A mass transfer.

We find that Case A models can spend up to a third of their main sequence lifetime in the semi-detached configuration. Usually, once Roche-lobe overflow occurs during core hydrogen burning in binary, the binary spends most of the remaining main sequence lifetime of the donor in the semi-detached configuration (Fig. 2). However, we find that binaries in which Roche-lobe overflow occurs very early in their main sequence lifetime, the binary enters into a contact configuration and eventually merges via L2 overflow. This is why we do not find our Case A models to spend more than 40% of their main sequence lifetimes in the slow Case A phase. We assess the number of semi-detached massive binaries in the LMC which is expected from our models in Sect. 6.3.

## 4. Observable properties of semi-detached models

Here, we evaluate the distributions of observable properties of our binary models while they are in a semi-detached configuration. Besides our theoretical predictions, many of the plots in this section already include information about observed semi-detached binaries. However, we perform a comparison of our results with observations separately, in Sect. 6.

### 4.1. Orbital period and mass ratio distribution

Figure 5 shows the predicted orbital period distribution of our Case A binary models during the semi-detached (unhatched) and contact (hatched with stars) phases of their evolution. The histogram is weighted by the binary birth probability (see Sect. 2.2), and their time spent in each orbital period bin during their semi-detached or contact phase. Comparing the contributions from the semi-detached phase and the contact phase shows that  $\sim 96\%$  of the interacting Case A binaries in our grid are in the semi-detached configuration. However, our assessment of the contact binary parameter space is incomplete as our lowest initial orbital period is  $\sim 1.4$  d. Including models with shorter initial periods leads to a larger predicted fraction of contact systems (see Sect. 6.3 and Menon et al. 2021).



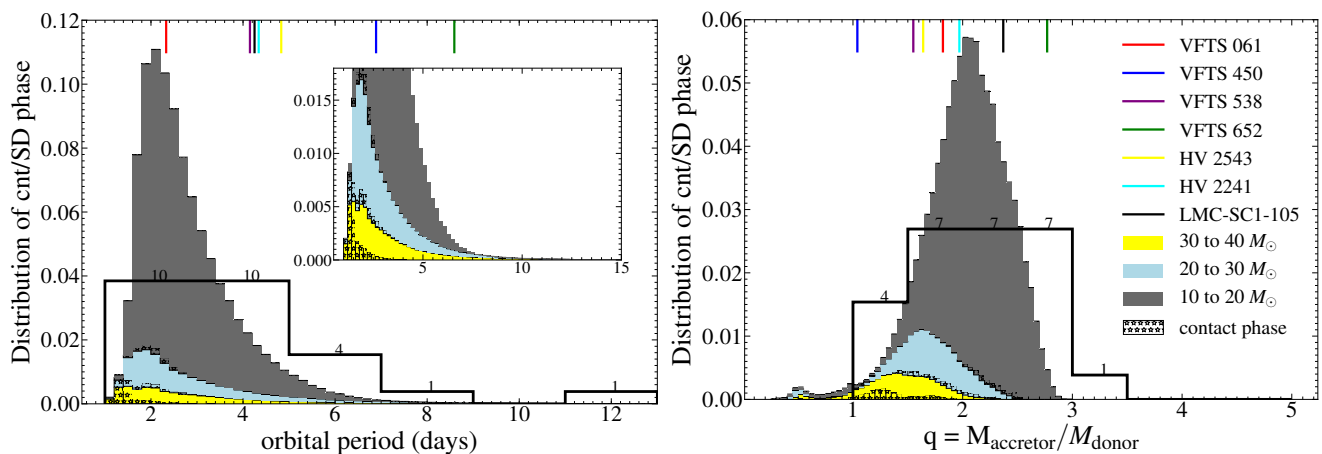


**Fig. 5.** Distribution of orbital periods (left panel) and mass ratios (right panel) of our models during the semi-detached phase (unhatched) or contact phase (hatched with stars) of Case A mass transfer. Colour coding marks three different initial mass ranges, as indicated. The ordinate values are normalised such that the sum of the number fractions in all bins equals unity. Vertical lines at the top of the plots denote the orbital periods and mass ratios of observed Algol systems in the LMC (Table 1), identified through their colour (see legend, same for both panels). The inset in the left panel shows a zoomed-in distribution of the yellow and blue models. The black step-histogram denotes the distribution of orbital periods and mass ratios of 26 observed massive Algol systems in the Milky Way (Table 2). It is normalised such that the area under both the histograms is same. The number of stars contributing to each bin is given on top of each bin.

The drop in the period distribution of the semi-detached systems towards the shortest periods in Fig. 5 is, however, not due to our lower initial period cut-off. We see from Fig. 1 that the shortest period models in our grid do not survive the Case A mass transfer phase as binaries. Amongst these presumable mergers, the models with shortest orbital periods spend increasingly more time in the contact than in the semi-detached configuration. Consequently, our semi-detached model population is essentially complete, for the investigated mass range.

For models with longer orbital periods, Case A mass transfer starts comparatively later during the main sequence evolution of the donor. Once the slow Case A mass transfer starts, it continues until the end of the main sequence evolution of the donor. Since the histogram is weighted by the lifetime of the models in the Case A mass transfer phase, the longer period models do not contribute to the same extent as the shorter period models. Moreover, fewer long orbital period models undergo Case A mass transfer (depending on the initial donor mass, c.f. Fig. F.1). Hence, the distribution drops off at higher orbital periods. The contribution from models in the contact phase keep increasing towards shorter periods and our grid is not ideal to investigate this phase. We predict to find most semi-detached systems around an orbital period of  $\sim 1.5$ -4 d.

Figure 5 (right panel) shows the predicted distribution of the mass ratios of our Case A models during the semi-detached and contact phases. Since the mass ratio is inverted during fast Case A, the models do not spend much time at mass ratios below unity. A significant fraction of time is spent in the slow Case A mass transfer phase, where the mass ratio has already inverted. Hence, we see a large peak at mass ratios of  $\sim 2$ . For more massive systems, the peak moves to smaller mass ratios due to the larger core mass fraction at higher mass.

The smaller peak near  $q = 0.5$  arises from the shortest period models where a thermal timescale contact occurs, followed by a nuclear timescale inverse slow Case A mass transfer. For example, a system with parameters  $(M_{1,i}, q_i, P_{\text{orb},i}) = (28.3 M_{\odot}, 0.800, 1.41 \text{ d})$  evolves as follows. The initially more massive star undergoes fast Case A mass transfer, followed by slow Case A. During the slow Case A mass transfer episode, the then more massive accretor fills its Roche lobe and contact

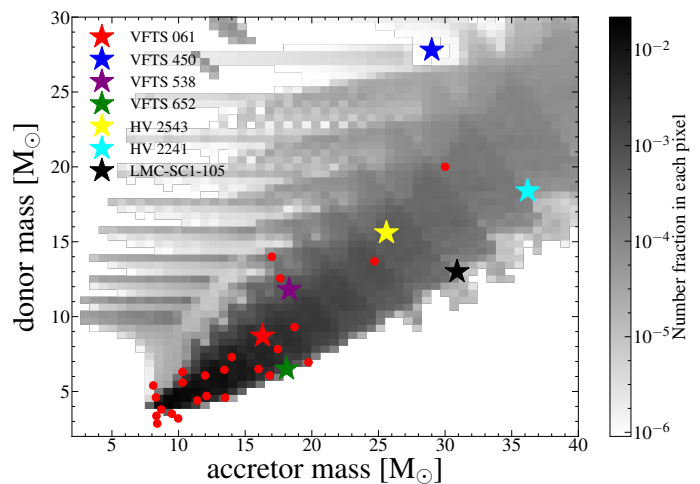


**Fig. 6.** Probability distribution of the donor and accretor masses that is predicted to be observed in the semi-detached configuration of the Case A mass transfer phase based on the model grid. The different coloured ‘stars’ denote the position of observed semi-detached systems in the LMC (Table 1). Grey-scale: See description in Fig. 7. The red circles denote the parameters for the Galactic Algol systems (Table 2).

occurs, which initiates inverse mass transfer. Shortly after the onset of contact, the initially more massive star shrinks below its Roche lobe radius, and the inverse slow Case A mass transfer occurs in a semi-detached configuration. Their expected number is small. However, they open a small chance to find Algol systems with mass flow from the currently more massive to the currently less massive star (e.g. VFTS 176, see Mahy et al. 2020a).

Figure 6 shows distribution of the absolute donor and accretor masses during the semi-detached phase. We see that the donor masses are significantly lower than the accretor masses, which is consistent with the fact that mostly the Roche-lobe filling star is the lower mass star of the binary. The highest probabilities for the lowest masses come from the combined

effect of the IMF weight on the distribution functions and the fact that the lower mass donors spend more time in the Case A mass transfer phase. We see a broader range of accretor masses for a given donor mass since more massive systems avoid merging during Case A evolution for a larger initial mass ratio range (cf., Fig. F.1).

Notably, the increase in orbital period after the Case AB phase (Fig. F.6) is highest in the lower initial donor mass models because of the smaller core size of the lower mass donors. Owing to the higher envelope to core ratio, a comparatively larger fraction of mass is transferred in the lower mass models, which increases the mass ratio of the binary and the orbital period also increases more.

#### 4.2. Surface abundances

In massive stars, the enrichment of helium and nitrogen is related, because both are products of the CNO-cycle (Kippenhahn & Weigert 1990). Within the convective core, CNO equilibrium is established quickly, such that nitrogen obtains its CNO equilibrium value while only little hydrogen has been converted into helium. However, the convective core of massive main sequence stars is receding with time, and leaves a transition region within which the hydrogen abundance drops from its initial value to the value currently inside the convective core. In stars above  $\sim 15 M_{\odot}$ , this transition layer is slowly mixed with overlying unprocessed matter by semiconvection, which extends the transition layers to regions above the initial convective core, and leads to layers in which both, helium and nitrogen are enhanced, but with a nitrogen abundance below the CNO equilibrium value (Langer 1991). In addition to that, the temperature above even the extended transition layer is high enough to allow for incomplete CNO burning, where some carbon is transformed into nitrogen, but oxygen is not. In our donor stars, all these layers appear successively at the surface and determine the abundances of the matter accreted by the accretor star, whose entire envelope undergoes thermohaline mixing as soon as even a small helium enrichment is present in the accreted matter.

Figure 7 shows the surface helium mass fraction ( $Y_s$ , left panel) and the ratio of the surface nitrogen mass fraction ( $N_s$ ) to the initial surface nitrogen mass fraction (right panel, which we call surface nitrogen mass fraction enhancement), of our donor and accretor models in the semi-detached configuration. It shows that the mass donors emerge from fast Case A mass transfer with essentially all of the unenriched part of their envelopes removed. A mild nitrogen enrichment is present in almost all donors, which results from CN-processing occurring above the H/He-transition layers in the donor star. At the beginning of the semi-detached phase, helium is still practically unenriched at the mass donor's surface (cf., Panel 'e' of Fig. 2).

During the further evolution, mass transfer from the donor during the slow Case A phase gradually brings layers from the hydrogen-helium gradient region of the donor to its surface, which raises its surface helium mass fraction appreciably (see also Fig. 2). However, the helium surface mass fraction of the donor stars usually remain below  $Y_s \approx 0.45$ . Correspondingly, the surface nitrogen mass fraction enhancement increases and eventually reaches the CNO equilibrium value of  $\sim 35$  for the LMC during the slow Case A phase. This indicates that during slow Case A mass transfer, layers start to be uncovered which were part of the convective core earlier in the evolution.

The enrichment of the surface of the mass gainers is mediated by thermohaline mixing, and therefore remains

significantly smaller than that of the donor. We see from Fig. 7 that their helium mass fraction remains mostly below  $Y_s \approx 0.29$  (the initial value is 0.256), whereas the nitrogen enrichment does not exceed a factor of 10 in the vast majority of cases. Core hydrogen burning in the accretors has already created a strong mean molecular weight gradient by the time the Roche-lobe overflow begins, which prevents a strong nitrogen enrichment due to rotational mixing even in rapidly rotating accretors (Wang et al. 2020).

In a small fraction of our models, the mass gainers reach rather high enrichment, that is, helium surface mass fractions in the range 0.30 . . . 0.38, and nitrogen mass fraction enhancements of up to 22 (Fig. 7). In Appendix B, we provide similar plots, but separately for three mass bins (Fig. B.2). This shows that the highly enriched mass gainers are restricted to systems with larger initial masses.

From investigating the Case A models that survive or eventually merge during slow Case A, separately, we find that the latter contain mass donors with surface nitrogen mass fraction enhancement below  $\sim 8$  for  $\sim 75\%$  of the time. Models that survive the slow Case A phase have donors whose surface nitrogen mass fraction enhancement is above  $\sim 8$  for  $\sim 90\%$  of the time they spend as semi-detached systems. Since both groups of binaries experience a nuclear timescale mass transfer phase, we expect observational counterparts to both these kinds of systems. In Sect. 3.2, we had shown that models that eventually merge during slow Case A phase contribute to  $\sim 70\%$  of the predicted observable binaries in the semi-detached phase.

Now, the fraction of models that survive vs merge during the slow Case A phase depends on the response of accretor radius to mass accretion. We know that accretors with inefficient semiconvective mixing (as in our models) are larger in radius than accretors with efficient semiconvective mixing (c.f. model 47 and 48 of Wellstein et al. 2001). This implies that our models are more likely to enter contact during slow Case A mass transfer than models with efficient semiconvection (such as the models of Menon et al. 2021). Hence, the predicted fraction of mergers during the slow Case A phase depends on, amongst other factors, the semiconvective efficiency.

Our binary models predict that in a sample of 100 observed massive Algol binaries, at least 52.5 (75% of 70% of 100 binaries) of the donors should show surface nitrogen mass fraction enhancement less than a factor of 8. On the other hand, at most 27 (90% of 30% of 100) donors can show surface nitrogen mass fraction enhancement greater than a factor of 8. If these number cut-offs ('at least 52.5' and 'at most 27') in the observed sample are largely different from our predictions, we can use this as another observational constraint to constrain the efficiency of semiconvection used in stellar models, via the close massive binary evolution channel (see also Schootemeijer et al. 2019).

The small group of models below the orange lines in Fig. 7 arises from the small number of models undergoing inverse slow mass transfer (cf., Sect. 4.1). In these models, mass flows back to the original donor star from its currently more massive and less enriched companion. These binaries arise from very short period models and eventually merge via L2 overflow after a nuclear timescale inverse slow Case A mass transfer phase followed by a contact phase.

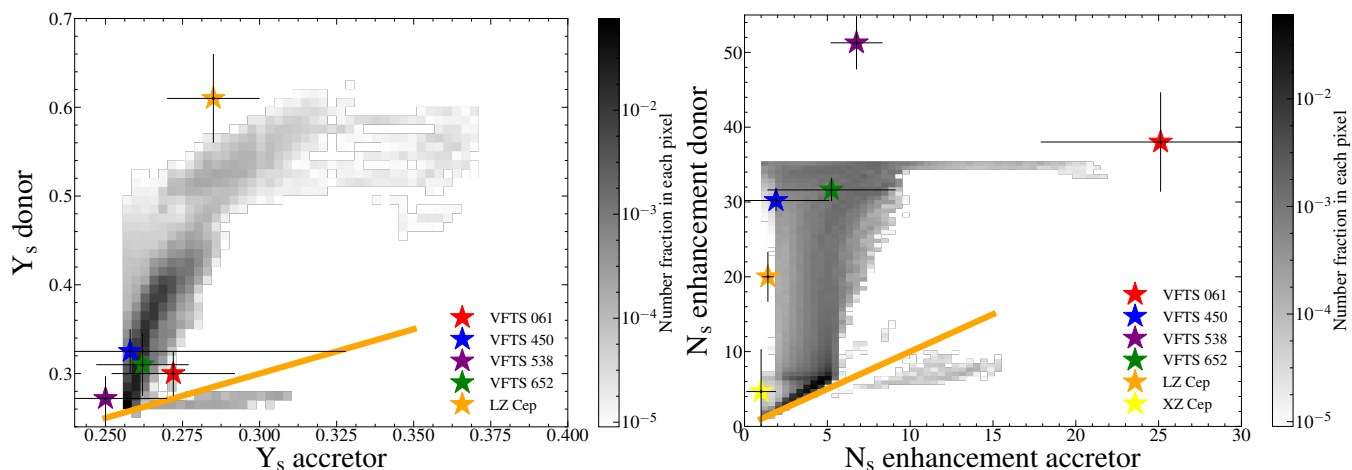


**Fig. 7.** Probability distribution of the surface helium mass fraction ( $Y_s$ , left panel) and surface nitrogen mass fraction ( $N_s$ , right panel, see text) of donor vs the accretor that is predicted to be observed in the semi-detached configuration of the Case A mass transfer phase based on the model grid. The different coloured ‘stars’ with error bars denote the position of the semi-detached systems of the TMBM survey and Galaxy. The surface nitrogen mass fraction enhancement of the LMC systems are evaluated w.r.t. to the LMC nitrogen abundance baseline, while the enhancement for LZ Cep and XZ Cep are evaluated w.r.t. to the Solar baseline. The grey-scale gives the probability fraction in each pixel. The total probability is normalised such that the integrated sum over the entire area is 1. The orange line indicates where the surface helium mass fraction or surface nitrogen enrichment of the donor and accretor is the same.

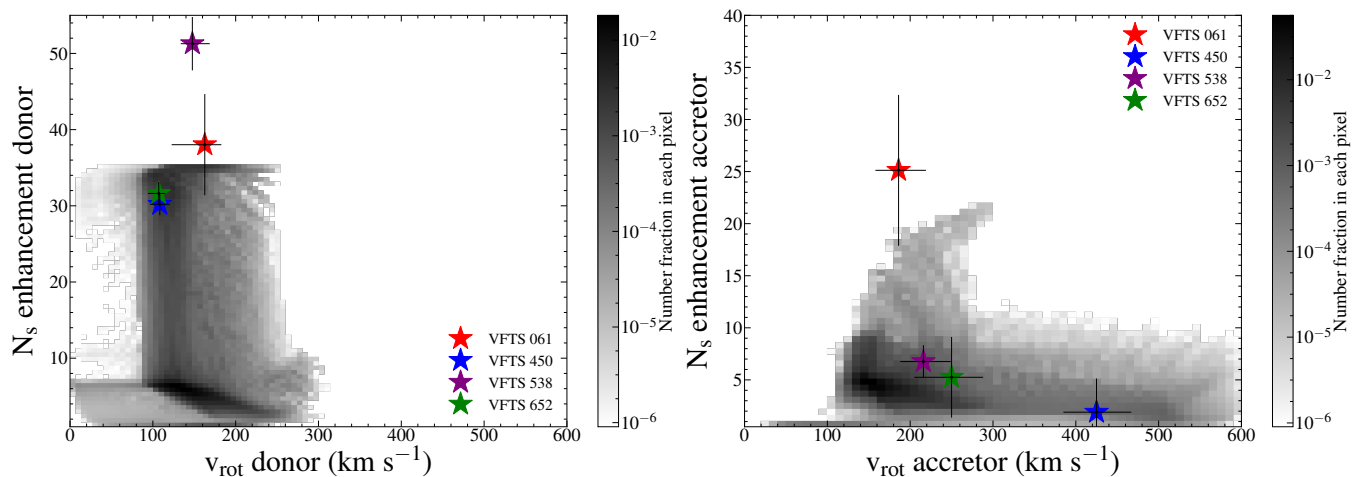


**Fig. 8.** Probability distribution of the surface nitrogen mass fraction enhancement vs rotational velocity of the donor (*left panel*) and accretor (*right panel*) during the semi-detached phase. The different coloured stars with error bars denote the position of the semi-detached systems of the TMBM survey (Table 3). Grey-scale: See description in Fig. 7.

#### 4.3. Effects of stellar rotation on nitrogen mass fraction enhancement

In single stars, the enhancement of surface nitrogen mass fraction gets higher with the increase in rotational velocity and mass of the rotating star, as internal mixing is more efficient in more massive and faster rotating stars (for a review, see [Maeder & Meynet 2000](#)). In binaries however, the donors can undergo envelope stripping which can expose layers of CNO processed material to the surface, increasing the surface abundance of nitrogen. Hence, it is essential to understand and differentiate between the contribution from internal mixing and envelope stripping to the observed surface nitrogen mass fraction enhancement in massive binaries.

Figure 8 shows the distribution of the surface nitrogen mass fraction enhancements of donor and accretor during the semi-detached phase as function of their surface rotational velocity. The surface rotational velocity of the donors is set by the orbital

motion of the binaries, as their rotation is synchronised to the orbital revolution.

The shortest orbital period binaries have the highest surface rotational velocities in our grid, owing to tidal locking at short orbital periods and the fact that we initialise the initial spins of the binary components to be equal to that of the orbit. In contrast to the single star picture, the donors rotating the fastest do not show the highest surface nitrogen mass fraction enhancement because the nitrogen enhancement in these binary models is not an outcome of rotational mixing but of envelope stripping. The donors with the highest rotational velocities ( $300 \text{ km s}^{-1}$ ) during the semi-detached phase arise from binaries with the shortest initial orbital period, go into a contact phase with an episode of inverse slow Case A mass transfer and eventually merge during their main sequence lifetime. It is hence likely that these models will not undergo significant envelope stripping by Case A mass transfer and do not show very high nitrogen enrichment until they merge.

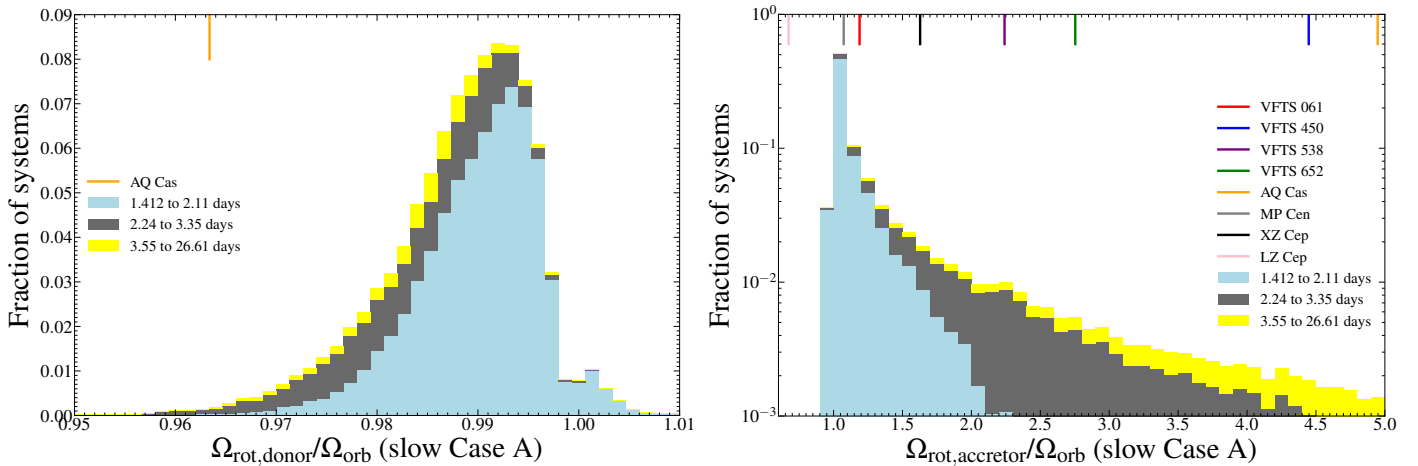


**Fig. 9.** Probability distribution of the ratio of spin to orbital angular velocity for the mass donor (left panel) and the mass accreting star (right panel) in our models during the semi-detached configuration, weighted by the birth probability of each system and the lifetime in the respective bin. The colour coding indicate the initial orbital period ranges indicated in the legend. The coloured vertical lines at the top of the right plot indicate the ratio of spin to orbital angular velocity of some of the observed massive Algol binaries where both parameters were found in the literature (Table 3). The Y-axis of the right panel is in log scale.

Donors with surface rotational velocities between  $\sim 100$ - $250$   $\text{km s}^{-1}$  have relatively higher initial orbital periods, where the binaries survive the slow Case A mass transfer and the envelope of the donors are efficiently stripped and the surface nitrogen mass fraction enhancement reaches CNO equilibrium values towards the end of the slow Case A phase (see vertical column of increasing surface nitrogen abundance near  $X \approx 150$ - $250$   $\text{km s}^{-1}$ ). We see two islands of higher probability of surface nitrogen enhancement, one at ordinate values of  $\approx 2$ - $6$  and the other near the CNO equilibrium value for the LMC (i.e.  $\approx 35$ ). As already discussed, the lower enhancement peak comes from models that eventually merge during slow Case A and the high surface enhancement peak comes from models that survive the entire Case A mass transfer phase. Hence, we expect the lower enhancement to be the result of rotational mixing (see also Maeder & Meynet 2000), while the enhancement all the way up to CNO equilibrium is from envelope stripping.

Surface rotational velocities less than  $90$   $\text{km s}^{-1}$  occur for a very brief time during the fast Case A mass transfer phase in our models when a large amount of mass is lost by the donor while tidal forces cannot instantaneously synchronise the rotation to the orbit. The light grey shading indicates that the amount of time spent in this region of the parameter space is very low. We also see two islands of surface nitrogen enhancement where the rotational velocity is below  $90$   $\text{km s}^{-1}$ . This dichotomy arises typically from low and high mass models whereby in lower mass models, the envelope is not very efficiently stripped, leading to low surface nitrogen mass fraction enhancement (c.f. Panel ‘f’ in Fig. 2) during and just after the fast Case A phase. In higher mass models, the envelope stripping is much more efficient, owing to the larger core to envelope mass, such that the surface nitrogen enrichment becomes very high right from the fast Case A mass transfer phase.

The right panel of Fig. 8 shows the distribution of the surface nitrogen mass fraction enhancement of the accretor versus their equatorial rotation velocity. As we shall see (Fig. 9, right panel), most of the accretors in our grid are tidally locked during the slow Case A phase. The increase in surface rotational velocity around  $200$ - $250$   $\text{km s}^{-1}$  with the increase in surface nitrogen mass fraction enhancement from  $15$ - $22$  indicates that these accretor stars only spin up slightly, not up to critical rotation,

towards the end of slow Case A mass transfer phase. These models having surface nitrogen enhancement  $> 15$  have orbital periods less than  $\sim 4$  days and survive the Case A mass transfer phase. Hence, the secondaries are able to accrete the N-rich matter transferred by the donor while not spinning up all the way to critical rotation during the late stages of the slow Case A mass transfer phase.

Accretors with rotational velocities above  $300$   $\text{km s}^{-1}$  are not found to be tidally locked. Hence they undergo inefficient slow Case A mass transfer (see Fig. F.2) and the surface nitrogen abundance is not as highly enhanced as for accretors that are rotating synchronously. We note that the probability fraction of accretors that are tidally synchronised is much higher than the accretors that are not tidally locked, consistent with Fig. 9 later.

#### 4.4. Tidal synchronization

Our mass transfer efficiency depends on the extent to which tidal forces can halt the spin-up of the mass accreting star (Sect. 2). For very short period binaries, tides can be strong enough to keep the mass accreting star rotating synchronously with the orbital velocity, enabling conservative mass transfer in our model grid. The strength of tidal forces implemented in our models can be tested by comparing the degree of synchronisation of our accretors during the slow Case A mass transfer phase as a function of orbital period to the degree of synchronisation of the accretors in observed massive Algol systems.

The tidal synchronization timescale of a mass donor decreases as the star expands to fill its Roche lobe. Figure 9 (left panel) shows the distribution of the ratio between spin and orbital angular velocity of the mass-donating star during the semi-detached phase. As these stars persist to fill their Roche lobes during this phase, we see that all our donors are effectively rotating fully synchronised during the entire semi-detached phase.

The right panel of Fig. 9 shows the distribution of the degree of synchronization of the mass accreting star during the semi-detached phase. We see that most of the mass accreting stars are rotating synchronously since the biggest contribution to the semi-detached phase comes from short period models where tidal interaction is strong. For higher orbital periods where

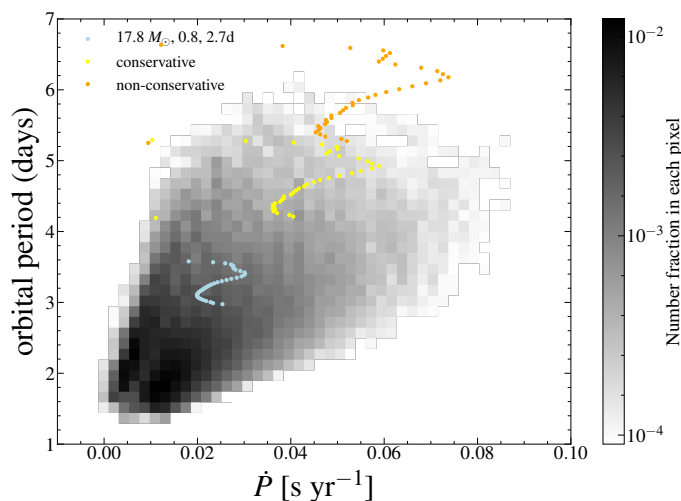


**Fig. 10.** Probability distribution of the orbital period and its derivative that is predicted to be observed in the semi-detached configuration of the Case A mass transfer phase based on the model grid. The lightblue coloured dots show the evolution of the orbital period and its derivative during the semi-detached phase for our example model in Fig. 2. The yellow and orange dots show the evolution for the same model if the mass transfer phase was modelled as totally conservative (Eq. 5) or totally non-conservative with the mass lost via isotropic re-emission (eq. 29 of Quast et al. 2019), respectively. The dots are placed at intervals of 50000 years with the first dots of each colour having the lowest orbital period. Grey-scale: See description in Fig. 7.

tidal synchronization is inefficient, the accretors rotate super-synchronously. As expected, the degree of super-synchronicity is higher for longer orbital periods.

#### 4.5. Orbital period derivatives

The orbital period derivative helps us assess the degree to which mass and angular momentum are lost from the binary and thus determine the efficiency of mass transfer in the binary system. Figure 10 shows the distribution of the orbital period and its time derivative during the slow Case A mass transfer phase. The period derivative value is very tightly constrained between 0.004-0.03 secs/year. This value of the orbital period derivative is related to the mass and angular momentum lost from the binary and the mass transfer efficiency during the slow Case A phase. We have seen that the mass transfer efficiency during the slow Case A phase in our models is largely conservative (Fig. 3).

The orbital period and its derivative if the entire Case A mass transfer was modelled as purely conservative or purely non-conservative with isotropic re-emission from the surface of the accretor can be analytically derived (eq. 30 or 29 of Quast et al. 2019, respectively), with deviations coming from the mass and angular momentum lost due to stellar winds. Both the orbital period and its derivative is higher for the case of totally conservative mass transfer (yellow dots) or totally non-conservative mass transfer with isotropic re-emission (orange dots) than our models.

We note that we implement non-conservative mass transfer in our models as an increase in wind mass loss rather than isotropic re-emission from the accretor (c.f. eq. 14 and 15 of Quast et al. 2019). As such, the orbital period in our models do not increase to the same extent as for the case of isotropic re-emission from the accretor. Comparing eq. 29 and 30 of Quast

et al. (2019) we can see that the orbital period derivative for the case of non-conservative mass transfer via isotropic re-emission becomes positive before the mass ratio is inverted and is higher than for the conservative case, as is seen in Fig. 10.

Hence, one can expect to test the mass transfer efficiency during the slow Case A phase and the implementation of non-conservative mass transfer for the overall Case A mass transfer phase in our models from measurements of the orbital period derivative of observed Algol systems over a few years. We note that the orbital period measurements are more constrained (Mahy et al. 2020a) than the values of orbital period derivatives we find during the semi-detached phase. For the mass dependence of this orbital period derivative during the slow Case A phase, see Fig. E.1.

## 5. Binary properties after Case AB mass transfer

After the slow Case A mass transfer, which is terminated by core hydrogen exhaustion of the donor star (Fig. 2), the donor star's envelope still contains several solar masses of hydrogen-rich matter (Fig. F.5). The contracting helium core therefore leads to an envelope expansion, which initiates another thermal timescale mass transfer phase, named Case AB. We find that 99.2% of the models that survive the slow Case A mass transfer also survive the Case AB mass transfer.

While this paper focusses on the semi-detached phase of evolution, we also briefly discuss the properties of our binary models after the Case AB mass transfer here. At this stage, they consist of a main sequence star with a stripped-envelope star as companion. Observations of such binaries are difficult, since the stripped star is very hot and hard to detect next to the brighter OB companion (Wellstein et al. 2001; Schootemeijer et al. 2018; Götberg et al. 2020; Wang et al. 2021). Only for the most massive systems in our model grid, it is expected that the stripped stars develop an optically thick wind and appear as Wolf-Rayet stars. According to Pauli et al. (2021, in prep), who analyse the WR+O star phase for a model grid with primary masses of up to  $\sim 90 M_{\odot}$ , this occurs for primary masses above  $\sim 28 M_{\odot}$  (see also, Shenar et al. 2020) at the metallicity of the LMC. In the following, we do not distinguish stripped stars with and without optically thick winds.

In our models, no mass transfer occurs during core helium burning and hence their orbital period and mass ratio does not change significantly throughout the core helium burning phase of the mass donor (c.f. Fig. 2, panel 'b' and 'g'). The orbital period increases slightly due to wind mass-loss while the mass ratio change remains small. Also, the surface properties of the individual binary components undergo only moderate changes. For our analysis, we sample the properties of our post Case AB models at a time when the core helium mass fraction of the mass donor (the stripped star) has decreased to 0.90 due to helium burning (except for Fig. G.1).

Figure 11 (top left panel) shows the orbital period and mass ratio distribution of our models after the Case AB mass transfer phase. Due to the additional mass transfer, the mass ratios of our post Case AB models are larger than during the slow Case A phase (cf., Fig. 5), with values up to  $q = 5$ . Since during Case AB, mass flows from a less massive to a more massive star (see panel 'h' of Fig. 2), the orbital period also increases significantly compared to models in the slow Case A phase, to values of  $\sim 15$  days and more. At the same time, since the Case AB mass transfer in our models is highly non-conservative (cf., Fig. F.5), orbital periods and mass ratios in our models

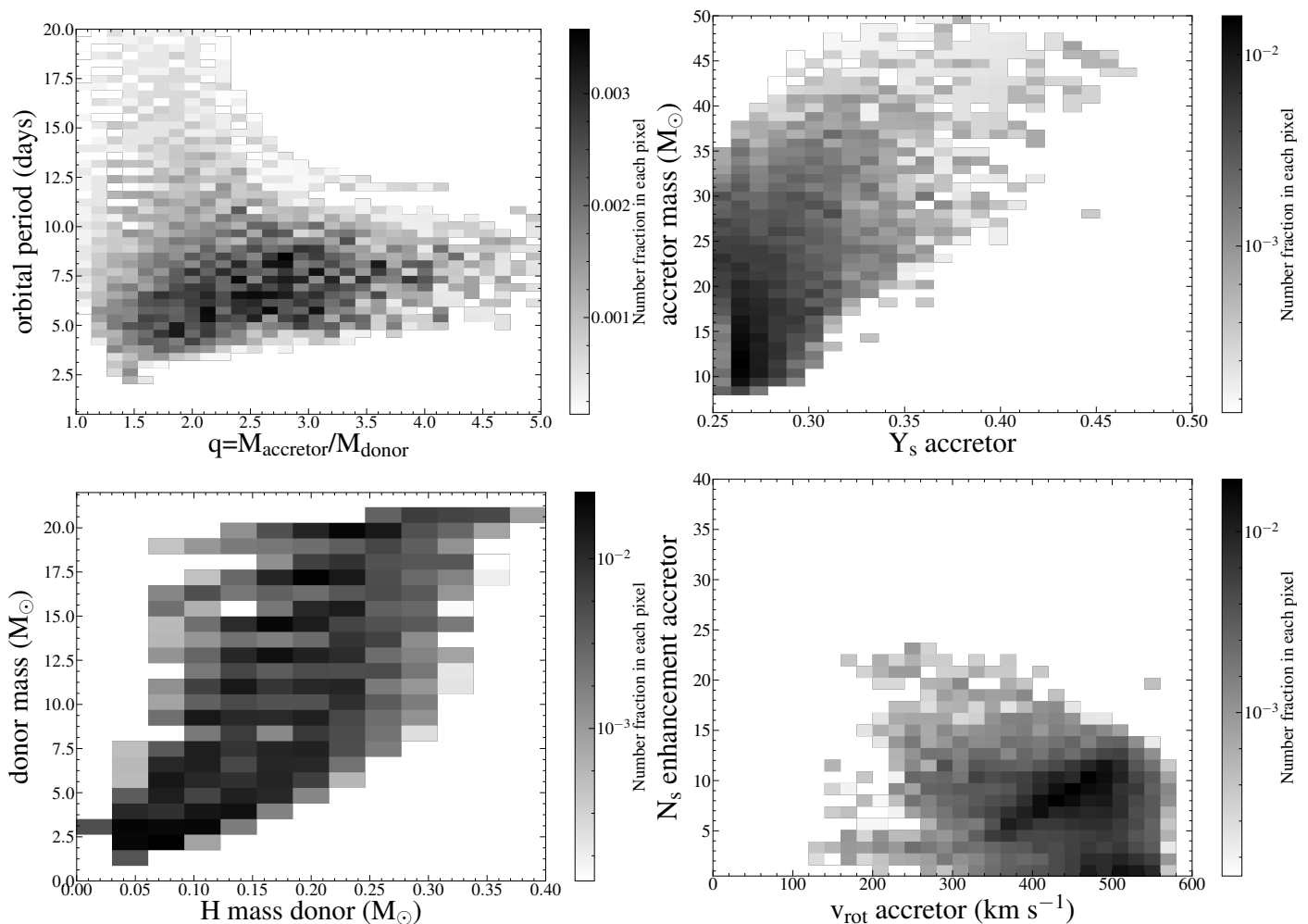


**Fig. 11.** Probability density distribution of several properties of our binary models after Case AB mass transfer, when the central helium mass fraction of the donor has decreased to 0.90: orbital period versus mass ratio (top left), surface helium abundance and mass of the mass gainer (top right), leftover hydrogen mass in the donor and donor mass (bottom left), and surface nitrogen mass fraction enhancement versus rotational velocity of the mass gainer (bottom right).

remain significantly smaller than in fully conservative models (e.g. Wellstein et al. 2001).

The top right panel of Fig. 11 displays the distribution of the surface helium mass fraction and stellar mass of our mass gainers. A comparison with Fig. 7 shows that the helium mass fraction is increased by a few percent compared to the semi-detached phase. Still, most mass gainers contain only a mild surface helium enrichment. However, more massive mass gainers tend to be more helium enriched, although there is a large spread for every considered mass. This is so because during core hydrogen burning, more massive stars have larger convective core mass fractions.

The surface helium mass fraction of the donors at the considered time is 0.70-0.90, and is most drastically reduced for the most massive systems, in which the donors become Wolf-Rayet stars (cf., Pauli et al. 2021 in prep). Figure 11 (bottom left panel) shows the distribution of remaining hydrogen mass in the post Case AB mass donors, as function of their mass. We compute the remaining hydrogen mass ( $M_H$ ) in the donor as  $M_H = \int_0^M X(m) dm$ . At most  $\sim 0.4 M_\odot$  of hydrogen remains in any of our models. We see the overall trend that the remaining hydrogen mass increases with the donor mass (see also, Yoon

et al. 2017). The wind stripping during the core helium burning phase of the mass donor is illustrated by Fig. G.1. A comparison with Fig. 11 shows that many of the most massive donors manage to lose all their hydrogen, whereas some hydrogen remains in all donors below  $\sim 12 M_\odot$ .

After Case AB mass transfer, many of the mass gainers may observationally appear as single stars because the high mass ratios and longer orbital periods make binary detection more elusive). Hence, it is interesting to consider the distribution of their surface nitrogen mass fraction enhancements and rotational velocities (Fig. 11, bottom right panel). The surface nitrogen mass fraction enhancement is higher than it was in the Algol phase (cf., Fig. 8), but far from its CNO equilibrium value of  $\sim 35$ . Whereas the matter that is transferred during Case AB does contain CNO equilibrium abundances, the mass transfer efficiency is low (cf., Fig. 3), and thermohaline mixing dilutes the small amounts of accreted matter in the massive envelope of the accretor.

Compared to the semi-detached phase (Fig. 8), where most of the mass accretors are tidally locked, Fig. 11 shows that the Case AB mass transfer spins them up considerably. This is so because the orbital periods increase rapidly during the

Case AB phase, rendering tidal braking inefficient in most cases. However, whereas many of our accretor models end Case AB mass transfer very close to critical rotation, tides remain strong enough to spin down most of our models over their core helium burning evolution (see Fig. G.1). For our most massive models, stellar winds also help to spin down the accretors. Therefore, our models provide only a small contribution to the overall population of Be stars, in particular compared to massive binary models undergoing mass transfer after core hydrogen burning (Case B, e.g. see Wang et al. 2020). We also note that the parameter space for Case A mass transfer is smaller than that for Case B mass transfer (Fig. 2 of Langer et al. 2020).

## 6. Comparison with observations

### 6.1. Observed Algol binaries in the LMC

The Tarantula Massive Binary Monitoring (TMBM) survey (Almeida et al. 2017; Mahy et al. 2020a,b) investigated  $\sim 100$  massive binaries in the Tarantula region of the LMC. Mahy et al. (2020a,b) classified six of them as semi-detached. From those, we find four to be in the Algol configuration, where the less massive star transfers mass to its more massive companion, and shows surface helium and nitrogen enrichment.

The other two systems (VFTS 176 and VFTS 094) have their more massive stars filling its Roche lobe, and are therefore not in the Algol configuration. Furthermore, none of the components shows any surface enrichment. Both systems have a very short orbital period (1.77 days and 2.25 days, respectively). It appears plausible that VFTS 176 and VFTS 094 evolved previously through a thermal timescale contact phase and are currently undergoing inverse nuclear timescale slow Case A mass transfer (see discussion in Sect. 4.1 for VFTS 176 and ‘System 2’ type evolution of contact binaries in Menon et al. 2021 for VFTS 094). Due to the lack of a concrete understanding of the current evolutionary stage of these two systems, we left these two systems out of our comparison with the predictions obtained from the model grid of binary models for the Algol phase. We list the observed properties of the classical TMBM Algol systems in Table 1, along with those of three massive Algols in the LMC described in the literature.

### 6.2. Observed Algol binaries in the Milky Way

In order to enhance the statistical basis of the comparison of our models with observations, we also consider observed Galactic massive Algol systems. We do this despite the metallicity difference between Milky Way and LMC, because the physics of mass transfer has no known direct metallicity dependence. However, we caution that an indirect impact of metallicity is possible, due to three effects. Firstly, stars of higher metallicity are slightly less compact (Brott et al. 2011a), such that longer orbital period binaries can contribute to the semi-detached phase at higher metallicity. Secondly, stellar winds are stronger in the Milky Way compared to the LMC (Mokiem et al. 2007), which may be relevant in particular for the most massive binaries discussed here. And thirdly, the most massive stars in our samples may be sufficiently close to the Eddington limit that envelope inflation may occur (Sanyal et al. 2015, 2017). While the first effect remains at the level of  $\sim 10\%$  (Brott et al. 2011b), the other two effects may be larger, especially for the most massive binaries discussed here. No metallicity dependence in the orbital period-mass ratio distribution of massive contact binaries has been predicted by Menon et al. (2021) between the

LMC and SMC, although they expect envelope inflation to play a role in explaining some of the observed long period ( $\geq 5$  d) massive contact binaries in the Milky Way.

Malkov (2020) performed a comprehensive literature survey of semi-detached double line eclipsing binaries in the Milky Way. He listed 119 semi-detached systems, of which 32 have at least one component with a stellar mass above  $8 M_{\odot}$  (Table 2). Investigation into the individual systems (see systems with footnotes in Table 2) reveals that GT Cep is in triple system, RZ Sct and BY Cru have an accretion disc that makes accurate determination of their masses very challenging, the mass ratio of TU Mon is highly debated in the literature, V453 Cyg is now considered as a detached system, V729 Cyg is a potential contact system and BY Cru shows evidence of very heavy interactions and contain an F type supergiant donor. As such, we do not include these six systems in our analysis. These systems will be very interesting for follow-up observations.

For four galactic Algol systems, an estimate of the projected rotational velocities of the component stars and for the orbital inclination was available in the literature. We list their parameters, together with those of the four classical TMBM Algols, in Table 3. We assume that the inclination of the orbital plane is the same as the inclination of the stellar spin axes. As such, we calculate the rotational velocity of the binary components from the projected rotational velocity and the orbital inclination (see Fig. 8). The orbital inclinations for the Algol binaries are taken from the references given in Table 2.

### 6.3. The number of semi-detached binaries in the LMC

To compare the expected number of semi-detached binaries from our grid of binary models with observations, we note that the Tarantula Massive Binary Monitoring (TMBM) survey (Almeida et al. 2017; Mahy et al. 2020a,b) has observations of 102 O type massive binary candidates with orbital periods in the range 1-1000 days. The TMBM sample was based on binary detections in the Very Large Telescope Flames Tarantula survey (Evans et al. 2011). Sana et al. (2013) showed that the binary detection probability is a function of the orbital period. It goes from 95% at 2 d to 87% at 10 d to 70% at 100 d to 25% at 1000 d. It is however beyond the scope of this paper to find this in our analysis. Hence, we consider all models in our grid that have initial orbital periods of less than 1000 days. This includes many models that do not undergo Case A mass transfer. To filter out the semi-detached models, we only consider those in which mass transfer during core hydrogen burning lasts for more than three times the thermal timescale of the mass donor (calculated at the onset of mass transfer). This way we find that 16% of all models with orbital periods less than 1000 d to undergo nuclear timescale Case A mass transfer.

We then find the sum of the weighted duration of the Case A mass transfer phase relative to the main sequence lifetime for each model as

$$F2 = \frac{\sum_{m=1}^{N_g} \tau_{\text{Case A}} W_m}{\sum_{m=1}^{N_g} \tau_{\text{MS}} W_m}, \quad (9)$$

where  $\tau_{\text{MS}}$  is as defined for Eq. (8) (cf., Sect. 3.3 and Fig. 4),  $N_g$  is the number of models in the grid with initial orbital periods below 1000 days, and  $W_m$  represents the birth probability of each system according to Eq. (3). We find that  $F2 \simeq 0.03$ , which implies that we expect 3 out of every 100 main sequence binaries originating from initial donor masses between 10-40  $M_{\odot}$  and orbital periods of 1.41-1000 days to be observed in the slow

**Table 1.** Semi-detached double-lined eclipsing binaries observed in the LMC with at least one component having a mass greater than  $8 M_{\odot}$ .

| Name (colour<br>in plots) | Period<br>days | $M_a$<br>$M_{\odot}$ | $M_d$<br>$M_{\odot}$ | q    | $R_a$<br>$R_{\odot}$ | $R_d$<br>$R_{\odot}$ | $T_a$<br>kK | $T_d$<br>kK | References<br># |
|---------------------------|----------------|----------------------|----------------------|------|----------------------|----------------------|-------------|-------------|-----------------|
| VFTS 061 (red)            | 2.33           | 16.3±1.4             | 8.7±0.6              | 1.87 | 7.2±0.2              | 7.30±0.3             | 33.5±0.9    | 32.9±0.7    | [1]             |
| VFTS 652 (green)          | 8.59           | 18.1±3.9             | 6.5±1.1              | 2.78 | 15.4±0.7             | 16.8±0.7             | 32.1±0.9    | 23.9±0.5    | [1]             |
| VFTS 538 (purple)         | 4.15           | 18.3±1.9             | 11.8±1.4             | 1.55 | 7.9±0.6              | 14.7±1.0             | 35.6±1.7    | 32.0±0.3    | [2]             |
| HV 2543 (yellow)          | 4.83           | 25.6±0.7             | 15.6±1.0             | 1.64 | 15.5±0.4             | 14.0±0.4             | 35.3±0.6    | 28.7±0.5    | [3]             |
| VFTS 450 (blue)           | 6.89           | 29.0±4.1             | 27.8±3.9             | 1.04 | 13.0±3.0             | 22.2±0.4             | 33.8±2.3    | 28.3±0.3    | [1]             |
| SC1-105 (black)           | 4.25           | 30.9±1.0             | 13.0±0.7             | 2.37 | 15.1±0.2             | 11.9±0.2             | 35.0±2.5    | 32.5±2.5    | [4]             |
| HV 2241 (cyan)            | 4.34           | 36.2±0.7             | 18.4±0.7             | 1.96 | 14.9±0.4             | 13.7±0.4             | 38.4±1.4    | 29.5±1.2    | [5]             |

**References.** (1) Mahy et al. (2020a); (2) Almeida et al. (2017); Mahy et al. (2020b); (3) Ostrov et al. (2000); (4) Bonanos (2009); (5) Ostrov et al. (2001);.

**Notes.** Subscripts ‘a’ and ‘d’ denote the accretor and donor star respectively. The systems are ordered by increasing mass of the mass gainer.

Case A mass transfer phase. This is in good agreement with the VFTS-TMBM survey, where we find four binaries to be in the Algol configuration amongst the 102 observed binaries.

Table 4 gives the contribution from each initial donor mass in our grid to the total of 3% (2nd column), in comparison to the expected contribution if it would simply scale with the Salpeter IMF (3rd column). It shows that while more massive systems contribute less to the total synthetic Algol population than less massive ones, their contribution is larger than expected according to the IMF, with  $40 M_{\odot}$  binaries contributing three times as much. This estimate needs to be amended by the fact that  $10 M_{\odot}$  stars live about five times longer than  $40 M_{\odot}$  stars, which implies a  $\sim 15$  times larger contribution of our most massive systems than naively expected. It reflects the fact that, for a given initial primary mass, the period and mass ratio range of surviving Case A binary models is much larger for larger initial primary mass, as can be seen when comparing the blue coloured areas in the upper and lower panels of Fig. F.1.

About 25% of all massive stars in the LMC are associated with the Tarantula region, with the estimated number of O-type stars being 570 (Doran et al. 2013; Crowther 2019). Extrapolating, we expect about 2000 O-type stars in the LMC. This accounts for a total of  $\sim 1000$  O-type star binaries in the LMC, assuming a binary fraction of 50% (Sana et al. 2013). We found in our model grid that 3% of all massive main sequence binaries are in the semi-detached phase. Therefore, we expect around 30 binaries that contain an O-type star in the semi-detached phase in the LMC, from our binary parameter space.

At the same time, in our parameter space, the ratio of models expected to be observed in the contact phase to the semi-detached phase is  $\sim 1/19$  (see discussion of Fig. 5). This implies that we expect  $\sim 1.6$  O-type contact binaries in the LMC originating from our initial parameter space. However, our initial orbital period range does not cover the shortest period contact systems, which have the longest contact lifetimes (Menon et al. 2021). Therefore, our number is smaller than the result of Menon et al. (2021), who, based on their evolutionary grids of contact binary models, and for a binary fraction of 50%, predict  $\sim 8$  O-type contact binaries in the LMC. B stars above  $\sim 10 M_{\odot}$  live roughly twice as long as average O stars, and accounting for a Salpeter initial mass function, we expect about 60 Algol binaries and 3 contact binaries amongst the  $\sim 4000$  B stars above  $10 M_{\odot}$  in the LMC.

#### 6.4. Orbital periods and mass ratios

Figure 5 compares the observed orbital periods of the semi-detached binaries with the predicted period distribution. Whereas observed and predicted period ranges agree well, there are more systems observed at larger period than expected from the theoretical distribution, in particular in the LMC sample. We note however that, while the distribution in Fig. 5 is dominated by the lower mass systems due to the steepness of the IMF, the observed Algol binaries in the LMC are very massive (see Fig. 6), and the predicted orbital period distributions stretch to significantly larger values for higher masses (Fig. C.1). On the other hand, we find the peak of the distribution of the Galactic Algol systems to be in good agreement, but again have more high period systems than predicted. While the significance of this mismatch remains unclear due to the unknown observational biases, we find one systems in the LMC (VFTS 652) and two in the Galaxy (V356 Sgr and BM Ori) each with orbital periods above 8 d but with accretor masses below  $20 M_{\odot}$ . Concerning the mass ratios, we find a reasonable match with most of the observed semi-detached binaries in the LMC and the Galaxy (Fig. 5). There is one systems (IZ Per) with a mass ratio above 3 that is not explained by our model grid.

Figure 12 (top panel) shows the probability distribution of the predicted orbital period and mass ratio of our Algol models simultaneously. We also estimate the distribution of Algol binaries from our models in the  $P-q$ -plane if, in retrospect, mass transfer had been assumed to be fully conservative (cf. Sect. 3.1; middle panel), and in the conservative models (of Wellstein et al. 2001, bottom panel). For our *pseudo* conservative approximation (middle panel), we assume that the binary will merge during Case A mass transfer if the mass transfer rate from the donor is greater than the mass divided by the thermal timescale of the accretor ( $M_{\text{acc}}/\tau_{\text{KH,acc}}$ ).

We see that in all the three panels, there is a sharp borderline leading to an absence of predicted high mass ratio models at the shortest orbital periods. This occurs since the shortest-period models in our grid are nearly conservative, and the retained mass and angular momentum during the mass transfer leads to a simultaneous increase of mass ratio and orbital period. Figure 12 shows further that for orbital periods above  $\sim 4$  d, our models predict a confinement of Algols to smaller mass ratios for larger periods (top panel). This occurs due to the fact that tides becomes weaker for larger periods, which leads to a smaller mass transfer efficiency (cf., Sect. 3). In the conservative case (middle and lower panel of Fig. 12), the opposite trend is seen.

We note that our *pseudo* conservative approximation predicts a maximum mass ratio of  $\sim 3.6$  while the maximum mass ratio



**Table 2.** Semi-detached double-lined eclipsing binaries observed in the Galaxy with at least one component exceeding  $8 M_{\odot}$ .

| Name                   | Period<br>d | $M_a$<br>$M_{\odot}$ | $M_d$<br>$M_{\odot}$ | $q$  | $R_a$<br>$R_{\odot}$ | $R_d$<br>$R_{\odot}$ | $T_a$<br>kK | $T_d$<br>kK | References<br># |
|------------------------|-------------|----------------------|----------------------|------|----------------------|----------------------|-------------|-------------|-----------------|
| TT Aur                 | 1.33        | 8.10                 | 5.40                 | 1.50 | 3.90                 | 4.20                 | 24.8        | 18.2        | [1]             |
| $\mu_1$ Sco            | 1.44        | 8.30±1.00            | 4.60±1.00            | 1.80 | 3.90±0.30            | 4.60±0.40            | 24.0±1.0    | 17.0±0.7    | [2]             |
| SV Gem                 | 4.00        | 8.34                 | 3.37                 | 2.47 | 4.87                 | 6.70                 |             |             | [3]             |
| V454 Cyg               | 2.31        | 8.40                 | 2.86                 | 2.93 | 4.99                 | 4.64                 |             |             | [1]             |
| BF Cen                 | 3.69        | 8.70                 | 3.80                 | 2.29 | 5.10                 | 7.10                 | 12.9        | 9.4         | [1]             |
| BM Ori                 | 6.47        | 9.50                 | 3.51                 | 2.70 | 4.47                 | 8.94                 |             |             | [3]             |
| IZ Per                 | 3.68        | 9.97±0.55            | 3.20±0.17            | 3.11 | 7.51±0.13            | 6.90±0.12            | 19.0±0.5    | 9.5±0.5     | [4]             |
| AI Cru                 | 1.41        | 10.30±0.20           | 6.30±0.10            | 1.63 | 4.95±0.06            | 4.43±0.05            | 24.2±0.5    | 17.7±0.5    | [5]             |
| SX Aur                 | 1.21        | 10.30±0.40           | 5.60±0.30            | 1.84 | 5.17±0.09            | 3.90±0.07            |             |             | [3]             |
| MP Cen                 | 2.99        | 11.40±0.40           | 4.40±0.20            | 2.59 | 7.70±0.10            | 6.60±0.10            | 18.7±0.4    | 12.4±0.1    | [6]             |
| IU Aur                 | 1.81        | 11.99±0.08           | 6.07±0.04            | 1.97 | 6.30±0.20            | 5.20±0.20            | 33.3±0.1    | 28.8±0.2    | [7]             |
| V356 Sgr               | 8.89        | 12.10                | 4.70                 | 2.57 | 7.40                 | 14.00                | 19.1        | 8.8         | [1]             |
| V Pup <sup>a</sup>     | 1.45        | 12.85±0.50           | 6.33±0.30            | 2.03 | 5.48±0.18            | 4.59±0.06            | 28.2±1.0    | 26.6±1.0    | [8]             |
| V498 Cyg               | 3.48        | 13.44                | 6.45                 | 2.08 | 6.81                 | 8.12                 |             |             | [1]             |
| GN Car                 | 4.34        | 13.49                | 4.59                 | 2.94 | 7.14                 | 8.29                 |             |             | [1]             |
| LZ Cep                 | 3.07        | 16.00±9.80           | 6.50±2.40            | 2.46 | 11.70±3.30           | 9.40±2.60            | 32.0±1.0    | 28.0±1.0    | [9]             |
| $\delta$ Pic           | 1.67        | 16.30                | 8.60                 | 1.89 | 7.62                 | 5.05                 | 25.2        | 21.4        | [10]            |
| XX Cas                 | 3.06        | 16.85                | 6.07                 | 2.77 | 8.28                 | 7.19                 |             |             | [1]             |
| HH Car                 | 3.23        | 17.00                | 14.00                | 1.21 | 6.10                 | 10.70                | 35.5        | 29.9        | [1]             |
| V337 Aql               | 2.73        | 17.44±0.31           | 7.83±0.18            | 2.22 | 9.86±0.06            | 7.48±0.04            | 28.0±0.5    | 23.6±0.5    | [11]            |
| AQ Cas                 | 11.70       | 17.63±0.91           | 12.50±0.81           | 1.41 | 13.40±0.64           | 23.50±0.73           | 27.0±1.0    | 16.7±0.4    | [12]            |
| XZ Cep                 | 5.09        | 18.70±1.30           | 9.30±0.50            | 2.01 | 14.20±0.10           | 14.20±0.10           | 28.0±1.0    | 24.0±3.0    | [13]            |
| 29 CMa <sup>b</sup>    | 4.39        | 19.00                | 16.00                | 1.20 | 10.00                | 13.00                | 29.0        | 33.7        | [14]            |
| AB Cru                 | 3.41        | 19.75±1.04           | 6.95±0.65            | 2.84 | 10.50±0.32           | 8.85±0.32            | 35.8        | 27.2        | [15]            |
| V448 Cyg               | 6.51        | 24.70±0.70           | 13.70±0.70           | 1.80 | 7.80±0.20            | 16.30±0.30           | 30.5±0.1    | 20.3±0.1    | [16]            |
| QZ Car <sup>c</sup>    | 5.99        | 30.00±3.00           | 20.00±3.00           | 1.50 | 10.00±0.50           | 20.00±1.00           | 36.0        | 30.0        | [17]            |
| *GT Cep <sup>d</sup>   | 4.90        | 10.70±0.50           | 2.58±0.14            | 4.14 | 6.34±0.19            | 6.98±0.11            | 22.4±1.0    | 10.9±0.3    | [18]            |
| *RZ Sct <sup>e</sup>   | 15.20       | 11.70                | 2.49                 | 4.68 | 15.00                | 15.90                | 19.0        | 6.5         | [1]             |
| *TU Mon <sup>f</sup>   | 5.04        | 12.00                | 2.50                 | 4.80 | 5.50                 | 7.20                 | 19.0        | 8.1         | [1]             |
| *V453 Cyg <sup>g</sup> | 3.89        | 14.36±0.20           | 11.10±0.13           | 1.29 | 8.55±0.06            | 5.49±0.06            | 26.6±0.5    | 25.5±0.8    | [1]             |
| *V729 Cyg <sup>h</sup> | 6.60        | 36.00±3.00           | 10.00±1.00           | 3.60 | 27.00±1.00           | 15.00±0.60           |             |             | [19]            |
| *BY Cru <sup>i</sup>   | 106.40      | 9-11                 | 1.80                 | 5.30 |                      |                      |             |             | [20]            |

**References.** (1) Surkova & Svechnikov (2004); (2) Budding et al. (2015); (3) Budding et al. (2004); (4) Hilditch et al. (2007); (5) Bell et al. (1987); (6) Terrell et al. (2005); (7) Surina & Kang (2009); (8) Stickland et al. (1998); (9) Mahy et al. (2011); (10) Evans (1974); (11) Tüysüz et al. (2014); (12) Ibanoglu et al. (2013); (13) Martins et al. (2017); (14) Bagnuolo et al. (1994) (15) Lorenz et al. (1994); (16) Djurašević et al. (2009); (17) Walker et al. (2017); (18) Çakırlı (2015); (19) Rauw et al. (1999); (20) Daems & Waelkens (1997).

**Notes.** Subscripts ‘a’ and ‘d’ refer to the mass accretor and mass donor, respectively. The list is adopted from the work of Malkov (2020) and Surkova & Svechnikov (2004). Systems without effective temperature estimates have only photometric orbit solutions and mass estimates. Comments on individual systems marked with superscripts: <sup>(a)</sup> Masses and radii taken from Budding et al. (2021). <sup>(b)</sup> May be a contact system (Mahy et al. in prep.). <sup>(c)</sup> Is a part of SB2+SB2 system, see Morrison & Conti (1979); Blackford et al. (2020). <sup>(d)</sup> Possibly a triple system, see discussion in text. <sup>(e)</sup> The more massive star is rapidly rotating and has an accretion disc. See Wilson et al. (1985). <sup>(f)</sup> Debate about the mass ratio of this system exists in the literature. See the discussion in Cester et al. (1977). <sup>(g)</sup> Recent studies now consider this as a detached system. See Southworth et al. (2004). <sup>(h)</sup> A potential contact system (Yaşarsoy & Yakut 2014) and a part of a hierarchical triple system (Rauw et al. 2019). <sup>(i)</sup> A highly interacting binary with an F type supergiant donor, with the accretor invisible due to an accretion disc around it. The long orbital period suggests it may be undergoing thermal timescale Case AB or Case B mass transfer. As such, we do not compare our model predictions with six (d,e,f,g,h,i) observed systems marked with an asterisk.

from self-consistent conservative models can go above 4. This is primarily because the conservative models of (Wellstein et al. 2001) do not include overshooting while our models do. This leads to the availability of a larger envelope mass of the donor that can be transferred to the accretor in the self-consistent conservative models and a lighter stripped donor star. This leads to a higher mass ratio for the self-consistent models towards the end of the slow Case A mass transfer.

In a large unbiased observational sample, we expect to find ~90% of the semi-detached systems in the LMC in the orbital period range 1.5-5 d and with mass ratios between one and three. About 75% of the observed Algol binaries do fall into these

ranges. Of the remaining ones, we find four Galactic systems just below our short period cut-off of 1.4 d, which may have undergone a short-lived contact phase (Menon et al. 2021). However, while this means that the bulk of the observed systems are well reproduced by our models (top panel), we see that this is also true for the conservative models (middle panel).

A preference between the two sampled mass transfer efficiency assumptions must be based on those Algol systems which are outliers. Of these, V454 Cyg ( $P, q=2.3$  d, 2.93) is missed in both cases. However, a handful of systems at the high mass ratio side, in particular IZ Per ( $P, q=3.7$  d, 3.11), V356 Sgr ( $P, q=8.9$  d, 2.57), and VFTS 652 ( $P, q=8.6$  d, 2.78) are missed by

**Table 3.** Orbital velocities, rotational velocities, and luminosities of the semi-detached double-lined eclipsing binaries, whenever available.

| Name     | Period<br>days | $v_{\text{rot,a}} \sin i$<br>km/s | $v_{\text{rot,d}} \sin i$<br>km/s | $\Omega_{\text{rot,a}}/\Omega_{\text{orb}}$ | $\Omega_{\text{rot,d}}/\Omega_{\text{orb}}$ | $\log L_{\text{a}}$<br>$L_{\odot}$ | $\log L_{\text{d}}$<br>$L_{\odot}$ | Inclination $i$<br>degrees |
|----------|----------------|-----------------------------------|-----------------------------------|---|---|------------------------------------|------------------------------------|----------------------------|
| VFTS 061 | 2.33           | $174^{+33}_{-28}$                 | $152^{+20}_{-40}$                 | 1.18  | 1.02  | $4.77 \pm 0.04$                    | $4.75 \pm 0.05$                    | $69.1^{+0.9}_{-0.9}$       |
| MP Cen   | 2.99           | $140^{+12}_{-12}$                 | $95^{+15}_{-15}$                  | 1.07  | 0.85  | $3.80 \pm 0.20$                    | $3.00 \pm 0.20$                    | $82.2^{+0.2}_{-0.2}$       |
| LZ Cep   | 3.07           | $130^{+10}_{-10}$                 | $80^{+10}_{-10}$                  | 0.67  | 0.51  | $5.11 \pm 0.19$                    | $4.69 \pm 0.19$                    | $48.1^{+2.0}_{-0.7}$       |
| VFTS 538 | 4.15           | $158^{+28}_{-33}$                 | $108^{+14}_{-21}$                 | 2.24  | 0.82  | $4.96 \pm 0.08$                    | $5.31 \pm 0.06$                    | $47.0^{+5.0}_{-5.0}$       |
| XZ Cep   | 5.09           | $230^{+15}_{-15}$                 | $110^{+12}_{-12}$                 | 1.62  | 0.78  | $5.05 \pm 0.06$                    | $4.79 \pm 0.22$                    | $80.0^{+2.0}_{-2.0}$       |
| VFTS 450 | 6.89           | $380^{+42}_{-40}$                 | $97^{+12}_{-12}$                  | 4.44  | 0.66  | $5.30 \pm 0.21$                    | $5.46 \pm 0.04$                    | $63.5^{+1.7}_{-1.2}$       |
| VFTS 652 | 8.59           | $224^{+38}_{-45}$                 | $96^{+10}_{-13}$                  | 2.75  | 1.08  | $5.35 \pm 0.06$                    | $4.92 \pm 0.06$                    | $63.7^{+0.9}_{-4.8}$       |
| AQ Cas   | 11.70          | $287^{+10}_{-10}$                 | $98^{+11}_{-11}$                  | 4.94  | 0.96  | $4.94 \pm 0.08$                    | $4.59 \pm 0.05$                    | $84.4^{+4.0}_{-4.0}$       |

**Notes.** The references to each individual system are the same as in Table 1 and 2. The subscript ‘a’ denotes the accreting star and ‘d’ denotes the Roche lobe filling mass donating star.

**Table 4.** Contribution from models at each initial donor mass ( $M_{\text{d,i}}$ ) to the total percentage (3%) of all massive main sequence binaries that is predicted to be found in the semi-detached configuration.

| $M_{\text{d,i}} (M_{\odot})$ | fraction (%) | IMF (%) | Relative excess |
|------------------------------|--------------|---------|-----------------|
| 10.0                         | 0.33         | 0.33    | 1.0             |
| 11.2                         | 0.31         | 0.28    | 1.1             |
| 12.6                         | 0.29         | 0.24    | 1.2             |
| 14.1                         | 0.27         | 0.20    | 1.3             |
| 15.8                         | 0.26         | 0.18    | 1.4             |
| 17.8                         | 0.26         | 0.15    | 1.7             |
| 19.9                         | 0.24         | 0.13    | 1.8             |
| 22.4                         | 0.21         | 0.11    | 1.9             |
| 25.1                         | 0.20         | 0.09    | 2.2             |
| 28.2                         | 0.18         | 0.08    | 2.3             |
| 31.6                         | 0.17         | 0.07    | 2.4             |
| 35.5                         | 0.16         | 0.06    | 2.7             |
| 39.8                         | 0.15         | 0.05    | 3.0             |

**Notes.** The third column gives the relative IMF weights for the initial donor masses, normalised to 0.33% for  $10 M_{\odot}$ . The last column gives the relative excess (column 2/column 3) of binaries predicted in the semi-detached configuration relative to the case where the contribution from the different masses would simply scale with the Salpeter IMF.

our calculations but are well covered by the conservative models. On the other hand, several low- $q$  systems are better reproduced by our non-conservative models, such as HH Car (3.2 d, 1.21), 29 CMa (4.39 d, 1.20), QZ Car (6.0 d, 1.50), VFTS 450 (6.9 d, 1.04), and AQ Cas (11.7 d, 1.41).

An obvious cure to these discrepancies would be to assume that mass transfer is more efficient in the first group (at high mass ratio), while retaining the low mass transfer efficiency otherwise. Notably, recovering HH Car and VFTS 450 needs a very non-conservative evolution. We note that while one could tune the mass transfer efficiency directly in binary model calculations, assuming more efficient tidal coupling would likely serve the same purpose in our models, as it would diminish the spin-up of the accretor and thus allow for more accretion.

Recently, Justesen & Albrecht (2021) found evidence for a higher efficiency of tidal circularization in binaries with temperatures between 6250 K and 10000 K. A higher efficiency of tidal coupling in the 4-10 d orbital period range than implemented in our models would lead to a higher mass

transfer efficiency in this orbital period range, which could help reproduce the high mass ratio outliers in Fig. 12 (top panel).

We note from Fig. F.2 that the transition from conservative to non-conservative mass transfer in our Case A models is a function of all three initial binary parameters, the donor mass, orbital period and mass ratio. The self-consistently generated boundary line between conservative and non-conservative mass transfer is also different for different phases of the mass transfer (i.e. fast Case A, slow Case A and Case AB). These boundary lines essentially denote the orbital period (for binaries of a certain initial donor mass and mass ratio) at which tidal forces are unable to halt the spin-up of our accretor models.

The above self-consistently derived mass transfer efficiency from our models can be easily implemented as an orbital period dependent mass transfer efficiency prescription in rapid binary evolution models. Then, quick tests on the extent to which the strength of tidal interactions needs to be increased can be gauged so as to reproduce some of the highest mass ratio Algols. This can be done by varying the boundary between efficient and inefficient mass transfer in the rapid codes, and looking at the maximum mass ratios attained by the models during the Algol phase. We also note that a completely non-conservative mass transfer at all orbital periods would not fit the observations as then we would underpredict the mass ratios of the very short period (1-3 d) semi-detached models that undergo fairly conservative mass transfer in our original model grid.

When looking at the mass dependence of the predictions (Fig. C.1), for the most massive binary Algol systems we find that at the highest considered accretor masses (above  $30 M_{\odot}$ ) the peak in the mass ratio distribution is much closer to one, and the orbital period distribution predicts a considerable fraction of Algol binaries above 5 d. Indeed, Fig. C.1 does not reveal any problem with our mass transfer scheme, where most of the observed Algols rather seem to be restricted to the lowest considered accretor mass interval (less than  $20 M_{\odot}$ ).

### 6.5. Surface abundances

The four Roche lobe filling donor stars of the TMBM sample which we assume to be in the slow Case A mass transfer phase have observed surface nitrogen abundances consistent with CNO cycle equilibrium (Fig. 7). These systems also show surface helium enrichment, signifying that their hydrogen-helium gradient region is exposed to the surface. We have shown (Fig. B.1) that the models that survive the Case A mass transfer

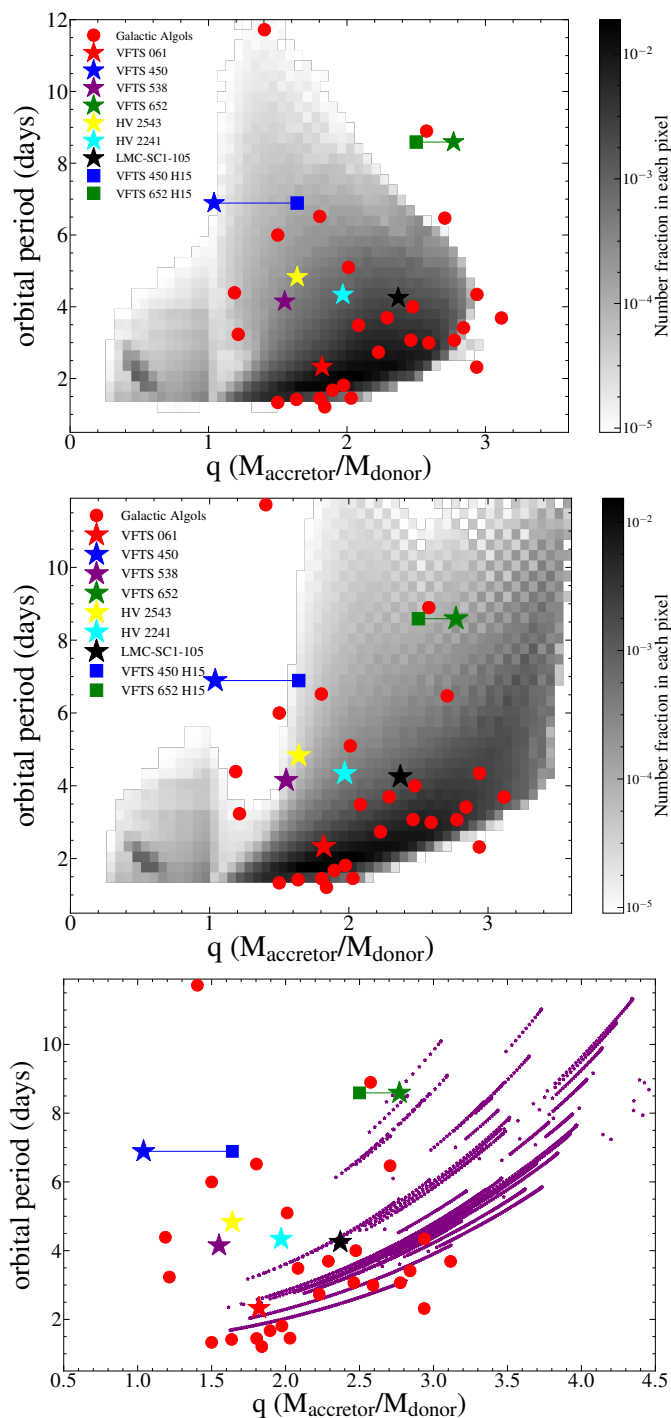


**Fig. 12.** *Top panel:* Probability distribution of orbital periods and mass ratios of our synthetic population of semi-detached binaries. For the grey scale, see description in Fig. 7. *Middle panel:* As the top panel, but with the retrospect assumption of fully conservative mass transfer (see text). *Bottom panel:* The evolution of orbital period versus mass ratio during the semi-detached phase of the 41 conservative Case A models of Wellstein et al. (2001), with primary masses of  $12 M_{\odot}$ ,  $16 M_{\odot}$  and  $25 M_{\odot}$  is marked by small purple stars. The small purple stars are placed with a time difference of 50 000 yrs. In all three plots, the different coloured star symbols denote the position of the semi-detached systems in the LMC (Table 1), and squares denote the binary parameters of VFTS 450 and 652 derived by Howarth et al. (2015). The colour coding is as in Fig. 5. Red circles denote the parameters for the Galactic Algol systems.

phase show high surface nitrogen enrichment. We conclude that these systems will likely survive the Case A mass transfer without merging.

On the other hand, there are two more VFTS systems (VFTS 094 and VFTS 176) in the semi-detached phase which we did not include in our analysis (cf., Sect. 6.1) that do not show surface helium and nitrogen enrichment (Mahy et al. 2020b). These systems have very short orbital periods (Mahy et al. 2020a). As we have shown in Sect. 4.2, a very mild surface nitrogen mass fraction enhancement in our donor models occurs only in very short period model systems that undergo inverse mass transfer and subsequently a contact evolution before merging during the slow Case A phase. Hence, these two systems are likely not following the classical Case A evolution, and may be progenitors of binary mergers.

In our models, a surface nitrogen enrichment above 5 is usually associated with an increase in surface helium mass fraction, as the slow Case A mass transfer exposes the hydrogen-helium gradient region. But this is not seen in VFTS 538, where the donor is consistent with no helium enhancement, while its nitrogen enrichment is seemingly even above the CNO equilibrium value. On the other hand, VFTS 061 has a short orbital period and shows high nitrogen enrichment in both components. This is consistent with the region of our parameter space that predicts high surface nitrogen mass fraction enhancement in both donors and accretors (Fig. 7), which occurs in our most conservative models.

Carbon deficiencies have also been observed in the more massive components of Algol binaries (Tomkin et al. 1993), signifying that CNO cycled material has been transferred from the currently lower mass star. A high surface enrichment is also observed in several Galactic Algol binaries. Mahy et al. (2011) find that the Roche lobe filling component of the semi-detached system LZ Cep shows a strong helium and nitrogen mass fraction enhancement. HD 149404 (Raucq et al. 2016) and XZ Cep (Martins et al. 2017) contain Roche lobe filling stars with surface abundances close to CNO equilibrium.

Overall, these observations reflect the range of enhancements we find in our models. While our donor models slowly increase their surface nitrogen abundance during the slow Case A evolution (see Figs. B.1 and B.2), they can reach values near CNO equilibrium during the second half of Case A mass transfer (cf., Fig. 3.1; see also Wang et al. 2017). A statistically significant Algol sample is needed to test whether additional physics assumptions are required, such as tidally induced mixing in close binaries (Hastings et al. 2020), to understand their surface abundances.

## 6.6. Synchronization

For eight observed Algol binaries (Table 3), the projected rotational velocities and inclination angles are available in the literature. For those, we determine the deviation of both components from synchronous rotation. We obtain the spin angular velocity ( $v_{\text{rot,a/d}}$ ) from the measured projected rotational velocity ( $v_{\text{rot,a/d}} \sin i$ ), the stellar radius and the inclination angle  $i$ , while the orbital angular velocity is derived from orbital period and orbital separation.

We find that the spins of three of the Roche lobe filling donors, VFTS 061, VFTS 652 and AQ Cas, to be synchronised with the orbit to within 10%. The remaining five donor stars seem to rotate slower than synchronous, by 15...50%. In our models, the donors do not deviate by more than 4% from synchronous rotation (Fig. 9, left panel). The largest deviations

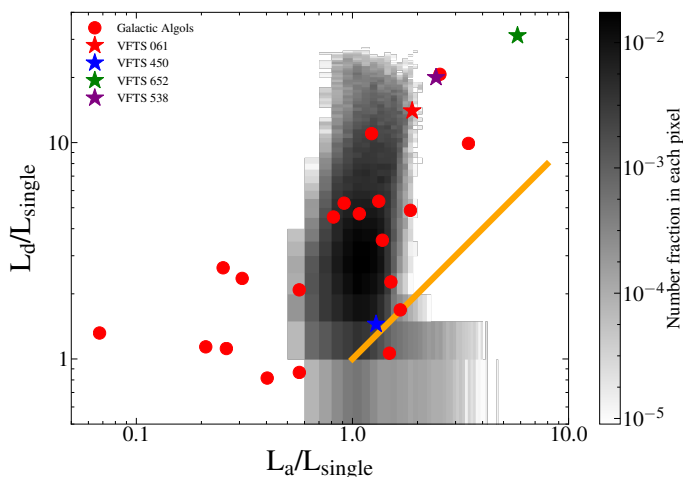


**Fig. 13.** Probability distribution of the ratios of the luminosities of the Algol donor and accretor models over the luminosities of single star models of the same mass and effective temperature (grey-scale, cf., description in Fig. 7). Red circles and coloured star symbols denote the corresponding parameters for the Galactic and LMC Algol systems, respectively (see Table 5). The orange line shows where the luminosity ratios of donor and accretor are equal.

are found for Galactic Algols (most extreme for LZ Cep) for which the derived radius may depend on the adopted distance. The resolution of this discrepancy needs a deeper investigation than is done here.

The vertical dashes on the top in the right panel of Fig. 9 denote the asynchronicities of the observed accretors (Table 3). All but one (LZ Cep) rotate super-synchronously, with an average value of 2.4 times synchronous rotation, and a maximum value of 5. Also a trend of stronger super-synchronicity with larger orbital period is apparent from the data (Table 3), which could imply that in closer systems, the accretion-induced spin-up is reduced by tidal interaction. Notably, the observed range of super-synchronicities, and its trend with orbital period, appears to be well reproduced by our models (Fig. 9, right panel). We note, however, that Derviřođlu et al. (2010) found in Algols of much lower mass, that the accretor rotates only at 10-40% of their critical velocity, even though their orbital periods exceed 5 d.

### 6.7. Overluminosity

We compare the luminosity of the individual stellar components of the observed semi-detached binaries in the LMC and Galaxy to the luminosity of a single star that has the same mass and effective temperature. For this, we use the single star models of Brott et al. (2011a) with initial rotational velocity of  $\sim 200$  km/s. We create 50,000 points with random masses between  $3-8 M_{\odot}$  and random ages between zero and terminal age main sequence. Through interpolation we assign a luminosity and effective temperature to each of the 50,000 points. Finally, we use the mass and effective temperature of an observed Algol binary component to find the nearest point on the stellar mass-effective temperature plane and note its luminosity. The ratio of the observed luminosity to this single star luminosity defines our overluminosity.

Table 5 lists the luminosities of the observed semi-detached binaries and the derived overluminosities; see also Fig. 13. We find that the observed mass donors are generally significantly

overluminous for their mass. Exceptions are AI Cru and  $\delta$  Pic, but their underluminosity is so small (10 and 20%, respectively) that an overluminosity can not be excluded. On average, the donors are overluminous by a factor of seven, with the record holder (VFTS 652) showing a factor of 30.

Such large overluminosities are expected for stars whose average mean molecular weight  $\mu$  is much larger than in single stars, since for chemical homogeneous stellar models of mass  $M$ , their luminosity  $L$  behaves as  $L \sim M^{\alpha} \mu^{\beta}$  (Kippenhahn & Weigert 1990), where, in the mass range  $10 \dots 30 M_{\odot}$ , the exponent  $\beta$  is  $5 \dots 2.5$  (Gräfenner et al. 2011; Köhler et al. 2015). As the mean molecular weight in the stellar core increases by a factor of  $\sim 2.2$  during hydrogen burning, and as the donor stars may be almost entirely stripped of their hydrogen envelope, we expect overluminosities of up to a factor of 50 for the donor stars (Wellstein et al. 2001). The observed large overluminosities are therefore a direct confirmation of the loss of a large fraction of the envelope of the Roche-lobe filling components of the Algol systems.

For the accretors, we expect a much smaller effect, since most of the transferred matter from the donor is comprised of its unenriched envelope. The accretor could be slightly underluminous in case it does not undergo complete rejuvenation (Braun & Langer 1995), or it could be slightly overluminous due to the accretion of some helium-enriched material, but both effects are expected to be small.

Figure 13 shows the distribution of the overluminosities of our Algol model components in comparison with the observed values. We see that the accretors cluster around an overluminosity factor of one. However, we find several stars with significantly smaller and larger values. Here, we can only speculate about the reasons for this mismatch. One interesting feature is that the smallest overluminosity factors of the accretors occur in systems which also have small overluminosities of their donors, and the most overluminous accretors are accompanied by the most overluminous donors. The cloud of points is stretched in the direction parallel to the yellow line, which indicates equal donor and accretor mass. Potentially, any error in the distance would move observed points in this direction. While such errors could well affect the location of the Galactic Algols in this diagram, this is unlikely for the VFTS binaries in the LMC. On the other hand we note that most of the observational data for the Galactic Algols has been obtained and analysed several decades ago<sup>3</sup>. As it stands, the average of the observationally derived overluminosities of the accretors does agree with our model prediction, but the observed distribution is much broader.

## 7. Comparison with earlier work

### 7.1. Properties before Case AB mass transfer

Previous studies on the Case A mass transfer phase were focussed on low to intermediate mass Algol binaries having masses  $0.1 \dots 8 M_{\odot}$  (Mennekens & Vanbeveren 2017; Negu & Tessema 2018). Mennekens & Vanbeveren (2017) compared the observed Algol systems having B-type companions with binary stellar evolution models in the solar neighbourhood. We note that while their models reached up to  $17 M_{\odot}$  for the initial donor mass, the observed binaries that they compare their models to

<sup>3</sup> For example, McSwain et al. (2008) note on the most extreme outlier in Fig. 13, BF Cen, that ‘Even the eclipsing double-lined spectroscopic binary BF Centauri (=HD 100915), a member of NGC 3766, has been largely neglected by modern spectroscopic observations.’

**Table 5.** Overluminosity of observed Algol binaries in the Galaxy and the LMC, whenever available.

| Name         | Period<br>days | $M_a$<br>$M_\odot$ | $M_d$<br>$M_\odot$ | $\log L_a$ | $\log L_d$ | $L_a/L_{\text{single}}$ | $L_d/L_{\text{single}}$ | $\log(L_a/M_a)$ | $\log(L_d/M_d)$ | Ref  |
|--------------|----------------|--------------------|--------------------|------------|------------|-------------------------|-------------------------|-----------------|-----------------|------|
| TT Aur       | 1.33           | 8.10               | 5.40               | 3.72       | 3.24       | 1.7                     | 1.7                     | 2.81            | 2.51            | [1]  |
| $\mu_1$ Sco  | 1.44           | 8.30±1.00          | 4.60±1.00          | 3.66       | 3.20       | 1.4                     | 3.5                     | 2.74            | 2.54            | [2]  |
| BF Cen       | 3.69           | 8.70               | 3.80               | 2.82       | 2.55       | 0.06                    | 1.3                     | 1.88            | 1.97            | [1]  |
| IZ Per       | 3.68           | 9.97±0.55          | 3.20±0.17          | 3.85       | 2.57       | 0.5                     | 2.3                     | 2.85            | 2.06            | [3]  |
| AI Cru       | 1.41           | 10.30±0.20         | 6.30±0.10          | 3.88       | 3.24       | 0.6                     | 0.9                     | 2.87            | 2.44            | [4]  |
| MP Cen       | 2.99           | 11.40±0.40         | 4.40±0.20          | 3.80       | 3.00       | 0.25                    | 2.63                    | 2.74            | 2.35            | [5]  |
| IU Aur       | 1.81           | 11.99±0.08         | 6.07±0.04          | 4.64       | 4.22       | 3.4                     | 9.9                     | 3.56            | 3.43            | [6]  |
| V356 Sgr     | 8.89           | 12.10              | 4.70               | 3.81       | 3.02       | 0.3                     | 2.3                     | 2.73            | 2.35            | [1]  |
| V Pup        | 1.45           | 14.00±0.50         | 7.30±0.30          | 4.28       | 3.97       | 1.7                     | 8.1                     | 3.13            | 3.10            | [7]  |
| $\delta$ Pic | 1.67           | 16.30              | 8.60               | 4.32       | 3.68       | 0.4                     | 0.8                     | 3.10            | 2.74            | [8]  |
| HH Car       | 3.23           | 17.00              | 14.00              | 4.73       | 4.91       | 1.8                     | 4.8                     | 3.50            | 3.76            | [1]  |
| V337 Aql     | 2.73           | 17.44±0.31         | 7.83±0.18          | 4.73       | 4.20       | 1.1                     | 4.7                     | 3.49            | 3.30            | [9]  |
| AQ Cas       | 11.70          | 17.63±0.91         | 12.50±0.81         | 4.94       | 4.59       | 1.48                    | 1.1                     | 3.69            | 3.49            | [10] |
| XZ Cep       | 5.09           | 18.70±1.30         | 9.30±0.50          | 5.05       | 4.79       | 1.3                     | 11                      | 3.78            | 3.82            | [11] |
| AB Cru       | 3.41           | 19.75±1.04         | 6.95±0.65          | 5.21       | 4.58       | 2.5                     | 20.6                    | 3.91            | 3.74            | [12] |
| V448 Cyg     | 6.51           | 24.70±0.70         | 13.70±0.70         | 4.63       | 4.57       | 0.3                     | 1.1                     | 3.23            | 3.43            | [13] |
| QZ Car       | 5.99           | 30.00±3.00         | 20.00±3.00         | 5.18       | 5.46       | 0.9                     | 5.2                     | 3.70            | 4.16            | [14] |
| VFTS 061     | 2.33           | 16.30±1.40         | 8.70±0.60          | 4.77       | 4.75       | 1.9                     | 14                      | 3.55            | 3.81            | [15] |
| VFTS 652     | 8.59           | 18.10±3.90         | 6.50±1.10          | 5.35       | 4.92       | 5.8                     | 31                      | 4.09            | 4.10            | [15] |
| VFTS 538     | 4.15           | 18.30±1.90         | 11.80±1.40         | 4.96       | 5.31       | 2.4                     | 20                      | 3.70            | 4.24            | [15] |
| VFTS 450     | 6.89           | 29.00±4.10         | 27.80±3.90         | 5.30       | 5.46       | 1.3                     | 1.5                     | 3.84            | 4.01            | [15] |

**References.** (1) [Surkova & Svechnikov \(2004\)](#); (2) [Budding et al. \(2015\)](#); (3) [Hilditch et al. \(2007\)](#); (4) [Bell et al. \(1987\)](#); (5) [Terrell et al. \(2005\)](#); (6) [Surina & Kang \(2009\)](#); (7) [Stickland et al. \(1998\)](#); (8) [Evans \(1974\)](#); (9) [Tüysüz et al. \(2014\)](#); (10) [Ibanoglu et al. \(2013\)](#); (11) [Martins et al. \(2017\)](#); (12) [Lorenz et al. \(1994\)](#); (13) [Djurašević et al. \(2009\)](#); (14) [Walker et al. \(2017\)](#); (15) [Mahy et al. \(2020a,b\)](#).

**Notes.** We give here the luminosity of the accretors ( $L_a$ ) and donors ( $L_d$ ) of massive semi-detached double-lined eclipsing binaries in the Galaxy and the LMC, and derive the ratio of their respective luminosity to that of single star models ( $L_{\text{single}}$ ) of the same mass and effective temperature. Masses and luminosities are in Solar units.

reached a maximum mass of  $\sim 8 M_\odot$ . They found evidence for non-conservative mass transfer.

In the low to intermediate star mass range, their models predict a peak in orbital periods of Algols between 5-10 d, and mass ratios (inverting their definition of mass ratio to match with ours) around 2. While their predicted mass ratio distribution matches with ours, we note that the most probable orbital periods are higher in their predictions. At the same time, the orbital period distribution of the observed Algol binaries, that they compare their model predictions to, has a peak between 2.5-4 d, which is closer to our predicted distribution of orbital periods. They conclude that the mass transfer in the intermediate-mass Algol binaries is non-conservative (see also [van Rensbergen et al. 2010](#)).

Evidence of low mass transfer efficiency was found in the study by [Petrovic et al. \(2005\)](#), who compare observations of three short-period WR+O binaries with their binary models. Investigation into the mass transfer efficiency (Fig. 3) of our models also reveals that models that do not merge during the main sequence have typically low mass transfer efficiencies and, as an outcome of how our mass transfer is calculated, decreases with increasing orbital period. However, we note that we predict the shortest period observed Algol binaries might have undergone a largely conservative mass transfer and is destined to eventually merge later during the slow Case A mass transfer phase.

Evidence of an orbital period dependent mass transfer efficiency was found by [de Mink et al. \(2007\)](#), who compared observed massive Algol binaries in the Small Magellanic Cloud to detailed binary evolution models. They found that the mass transfer efficiency of their models, that can reproduce the

observations, has to decrease with increasing orbital period. We have shown that our accretor spin-up dependent mass transfer efficiency does reproduce this orbital period dependency naturally (Fig. 3), giving additional credibility to our modelling of the mass transfer phase.

[de Mink et al. \(2014\)](#) studied the effects of a binary population on a synthetic massive star population assuming a binary fraction of 0.7. They assumed that, in their standard simulation, binaries with initial mass ratios less than 0.65 merge. They found that 3% of their total population of models to be binaries in the semi-detached phase. We also predicted the same fraction of such systems from our binary model grid, which can be said to be well in harmony with the former study, when the uncertainties related to mass transfer efficiency, angular momentum loss are taken into consideration. In our models, the dividing line (in initial mass ratio) between stable and unstable mass transfer depends on the initial donor mass (c.f. Fig. 1, upper and lower panels of F.1), with more low initial mass ratio binaries undergoing stable Case A mass transfer at higher initial donor masses. By inspection, we found that lower initial mass ratio models spend less time in the slow Case A mass transfer phase, such that the overall prediction of the properties of Algol systems are not significantly affected by the smaller initial mass ratio models that also undergo stable mass transfer in our binary grid.

The predicted velocity semi-amplitude of the semi-detached models in [de Mink et al. \(2014, fig. 2\)](#) matches well with the orbital velocity distribution of the accretors in our model grid (Fig. D.1). However, the orbital velocities of the donor are considerably higher on average than predicted by the former study. This is in part due to the fact that [de Mink et al. \(2014\)](#)

accounted for the random 3D orientation of the plane of the orbit, while we only report the absolute value of the orbital velocity.

However, incorporating this randomness in orientation will also reduce the average orbital velocity of the accretors and the resolution of this conflict requires a deeper investigation than we do here. We also note that the calculation of this phase in [de Mink et al. \(2014\)](#) was done using a rapid binary stellar evolution code, which does not calculate in detail through the mass transfer phase but rather uses fitting recipes ([Tout et al. 1997](#); [Hurley et al. 2002](#)) to simulate the properties of the stars during and after the mass transfer phase.

The general properties of our models (Sect. 2.3) are in agreement with the binary models of [Pols \(1994\)](#) who find that their models having initial donor mass of  $16 M_{\odot}$  and orbital periods below 1.6 d enter into contact during the slow Case A mass transfer phase (c.f. Fig. F.1). Moreover, as in [Pols \(1994\)](#), we also see that our models having low orbital periods and low mass ratios enter into a thermal timescale contact during the fast Case A mass transfer phase (compare hatching in bottom panel of Fig. F.1 with black frames around coloured squares in right-middle panel of Fig. F.2).

## 7.2. Properties after Case AB mass transfer

Recently, [Langer et al. \(2020\)](#) investigated the properties of black hole+OB star binaries in the LMC using the same grid of binary evolution models as is used in our work. Comparing their predictions of the mass ratio and orbital period of black hole+OB binaries arising from Case A mass transfer (figs. 4 & 6), we find that our prediction of the most probable mass ratios and orbital periods (Fig. 11) after the Case AB mass transfer phase are very similar to their predicted distribution. We expect this to be the case because the models do not go through any more mass transfer phases, before the collapse of the initially more massive star, that can significantly alter the binary properties (see however [Laplace et al. 2020](#)). Likewise, predictions of surface nitrogen mass fraction enhancement and rotational velocity of the mass accretor after the Case AB mass transfer (Fig. 11) are very similar to the corresponding properties of the OB star companions to the BHs in [Langer et al. \(2020, fig. 8 & 9\)](#).

## 8. Conclusions

Semi-detached binaries pose a crucial test for massive binary evolution models. On one hand, their evolution is typically simpler than that of the shortest period binaries, whose components may swap mass back-and-forth and evolve through long-lived contact stages ([Marchant et al. 2016](#); [Menon et al. 2021](#)). On the other hand, longer-period binaries undergo thermal timescale mass transfer after the donor star has exhausted hydrogen in its core, after which their binary nature remains elusive ([de Mink et al. 2014](#)).

The nuclear timescale semi-detached phase leads to the prediction that about 3% of all massive binaries in the LMC, with initial donor masses  $10 \dots 40 M_{\odot}$  and orbital periods above 1.4 d, should be found in this stage, which corresponds to a significant population in any star-forming galaxy. They are easily identified, since they are photometrically variable and show large radial velocity variations. While they undergo nuclear-timescale mass transfer currently, they underwent a phase of thermal timescale mass transfer previously. It is the latter which leads to the most drastic changes of the binary properties. This thermal timescale mass transfer is crucial for all mass transferring binaries, and the semi-detached binaries allow us to examine its consequences.

Based on our large grid of  $\sim 10\,000$  detailed binary evolution models ([Marchant 2017](#)), we predict the distribution functions of the orbital properties of massive semi-detached binaries (orbital period, period derivative, orbital velocities, mass ratio) as well as the surface properties of both stellar components (luminosity, temperature, chemical composition, spin). A comparison with the available observations evidently confirms the classical Algol scenario ([Crawford 1955](#); [Kopal 1971](#)) for most of the observed massive semi-detached systems, most spectacularly by the observed large overluminosities of the donor stars by up to a factor of 30 (Fig. 13). These, as most other observables, are found in fair agreement with the model predictions.

Some necessary corrections of our models are also signified by the observations. The observed period and mass ratio distribution demonstrates that some semi-detached binaries did undergo nearly conservative mass transfer, while others can only be explained assuming very non-conservative evolution (Fig. 12). This empirical range of accretion efficiencies is well reproduced by our models (cf., Appendix F). But a more efficient mass accretion in the lowest considered mass range ( $10 \dots 20 M_{\odot}$ ; Fig. C.1), perhaps mediated by a stronger tidal coupling than the one adopted here, could help to understand the Algol systems with the highest mass ratios. New binary models are required to explore this.

However, the impetus from the current models can not yet be fully harvested, since the number of well observed massive Algol systems is small. For the LMC, large progress has been made by the TMBM ([Almeida et al. 2017](#)) and BBC ([Villaseñor et al. 2021](#)) surveys. Through detailed analyses, [Mahy et al. \(2020a,b\)](#) derived the most relevant observational constraints for our models for four TMBM targets. However, in agreement with our predictions, the Algol binaries comprise only a few percent of the targets in these surveys. Of the putative 90 LMC Algols above  $10 M_{\odot}$ , we have basic data for seven, and highest quality analyses for four. While we know more massive Algols in the Milky Way, the data here is scarce, very heterogeneous and often without error estimates. This calls for a high quality multi-epoch survey dedicated to massive Algol binaries.

When confronted with the results of such a survey, we expect more crisp constraints on the input physics of our models (see App. A). In addition, model grids for solar and sub-LMC metallicity would form a big step forward to understand the impact of metallicity on the mass transfer process. While parameter variations are difficult for model grids as large as the one analysed here, the best studied Algol binaries could be attempted to be reproduced by tailored models where the input physics could be varied. As semi-detached massive binaries may be progenitors of magnetic main sequence stars ([Schneider et al. 2016, 2019](#); [Takahashi & Langer 2021](#)), hydrogen-poor supernovae ([Yoon et al. 2010](#); [Dessart et al. 2020](#); [Stanway et al. 2020](#)), neutron star and black hole binaries ([Tauris & van den Heuvel 2006](#); [Van Bever & Vanbeveren 2000](#); [Langer et al. 2020](#)), and double-compact binary mergers ([Eldridge & Stanway 2016](#); [Kruckow et al. 2018](#)), pursuing these routes promises to be fruitful.

*Acknowledgements.* We thank the anonymous referee, Dany Vanbeveren, Jan J. Eldridge and Mario Spera for helpful comments that refined the submitted version of the manuscript. SdM and AM acknowledge partial financial support from the European Union's Horizon 2020 research and innovation program (ERC, Grant agreement No. 715063), and from the Netherlands Organization for Scientific Research (NWO) as part of the Vidi research program BinWaves with project number 639.042.728. PM acknowledges support from the FWO junior postdoctoral fellowship No. 12ZY520N. AM was also supported by the Alexander von Humboldt foundation. LM thanks the European Space Agency (ESA) and the Belgian Federal Science Policy Office (BELSPO) for their support

in the framework of the PRODEX Program. This project has received funding from the European Research Council under European Union's Horizon 2020 research programme (grant agreement No 772225: MULTIPLES). This research has made use of NASA's Astrophysics Data System and the VizieR catalogue access tool, CDS, Strasbourg, France.

## References

- Abbott, B. P., Abbott, R., Abbott, T. D., et al. 2019, *Physical Review X*, 9, 031040
- Abdul-Masih, M., Sana, H., Sundqvist, J., et al. 2019, *ApJ*, 880, 115
- Almeida, L. A., Sana, H., Taylor, W., et al. 2017, *A&A*, 598, A84
- Asplund, M., Grevesse, N., & Sauval, A. J. 2005, in *Astronomical Society of the Pacific Conference Series*, Vol. 336, *Cosmic Abundances as Records of Stellar Evolution and Nucleosynthesis*, ed. I. Barnes, Thomas G. & F. N. Bash, 25
- Bagnuolo, William G., J., Gies, D. R., Hahula, M. E., Wiemker, R., & Wiggs, M. S. 1994, *ApJ*, 423, 446
- Banyard, G., Sana, H., Mahy, L., et al. 2021, arXiv e-prints, arXiv:2108.07814
- Belczynski, K., Kalogera, V., Rasio, F. A., et al. 2008, *ApJS*, 174, 223
- Bell, S. A., Kilkeny, D., & Malcolm, G. J. 1987, *MNRAS*, 226, 879
- Blackford, M., Walker, S., Budding, E., et al. 2020, *The Journal of the American Association of Variable Star Observers*, 48, 3
- Böhm-Vitense, E. 1960, in *IAU Symposium*, Vol. 12, *Aerodynamic Phenomena in Stellar Atmospheres*, ed. R. N. Thomas, 338–345
- Bonanos, A. Z. 2009, *ApJ*, 691, 407
- Braun, H. & Langer, N. 1995, *A&A*, 297, 483
- Breivik, K., Coughlin, S., Zevin, M., et al. 2020, *ApJ*, 898, 71
- Brott, I., de Mink, S. E., Cantiello, M., et al. 2011a, *A&A*, 530, A115
- Brott, I., de Mink, S. E., Cantiello, M., et al. 2011b, *VizieR Online Data Catalog*, J/A+A/530/A115
- Budding, E., Butland, R., & Blackford, M. 2015, *MNRAS*, 448, 3784
- Budding, E., Erdem, A., Çiçek, C., et al. 2004, *A&A*, 417, 263
- Budding, E., Love, T., Blackford, M. G., Banks, T., & Rhodes, M. J. 2021, *MNRAS*, 502, 6032
- Cantiello, M. & Langer, N. 2010, *A&A*, 521, A9
- Çakırlı, Ö. 2015, *New A*, 35, 71
- Cester, B., Fedel, B., Giuricin, G., Mardirossian, F., & Pucillo, M. 1977, *A&A*, 61, 469
- Choi, J., Dotter, A., Conroy, C., et al. 2016, *ApJ*, 823, 102
- Clark, J. S., Ritchie, B. W., Najarro, F., Langer, N., & Negueruela, I. 2014, *A&A*, 565, A90
- Crawford, J. A. 1955, *ApJ*, 121, 71
- Crowther, P. A. 2019, *Galaxies*, 7, 88
- Daems, K. & Waelkens, C. 1997, *A&A*, 327, 640
- de Mink, S. E., Cantiello, M., Langer, N., et al. 2009, *A&A*, 497, 243
- de Mink, S. E., Langer, N., Izzard, R. G., Sana, H., & de Koter, A. 2013, *ApJ*, 764, 166
- de Mink, S. E., Pols, O. R., & Hilditch, R. W. 2007, *A&A*, 467, 1181
- de Mink, S. E., Sana, H., Langer, N., Izzard, R. G., & Schneider, F. R. N. 2014, *ApJ*, 782, 7
- Dervişoğlu, A., Tout, C. A., & Ibanoglu, C. 2010, *MNRAS*, 406, 1071
- Deschamps, R., Braun, K., Jorissen, A., et al. 2015, *A&A*, 577, A55
- Dessart, L., Yoon, S.-C., Aguilera-Dena, D. R., & Langer, N. 2020, *A&A*, 642, A106
- Detmers, R. G., Langer, N., Podsiadlowski, P., & Izzard, R. G. 2008, *A&A*, 484, 831
- Djurašević, G., Vince, I., Khruzina, T. S., & Rovithis-Livaniou, E. 2009, *MNRAS*, 396, 1553
- Doran, E. I., Crowther, P. A., de Koter, A., et al. 2013, *A&A*, 558, A134
- Dunstall, P. R., Dufton, P. L., Sana, H., et al. 2015, *A&A*, 580, A93
- Eldridge, J. J. & Stanway, E. R. 2016, *MNRAS*, 462, 3302
- Eldridge, J. J., Stanway, E. R., Xiao, L., et al. 2017, *PASA*, 34, e058
- Evans, C. J., Taylor, W. D., Hénault-Brunet, V., et al. 2011, *A&A*, 530, A108
- Evans, R. G. 1974, *MNRAS*, 167, 517
- Ge, H., Webbink, R. F., Chen, X., & Han, Z. 2020, *ApJ*, 899, 132
- Giacobbo, N., Mapelli, M., & Spera, M. 2018, *MNRAS*, 474, 2959
- Gorda, S. Y. & Svechnikov, M. A. 1998, *Astronomy Reports*, 42, 793
- Göteborg, Y., Korol, V., Lamberts, A., et al. 2020, *ApJ*, 904, 56
- Gräfener, G., Vink, J. S., de Koter, A., & Langer, N. 2011, *A&A*, 535, A56
- Hastings, B., Langer, N., & Koenigsberger, G. 2020, *A&A*, 641, A86
- Heger, A., Langer, N., & Woosley, S. E. 2000, *ApJ*, 528, 368
- Heger, A., Woosley, S. E., & Spruit, H. C. 2005, *ApJ*, 626, 350
- Hilditch, R. W., Hill, G., & Lister, T. A. 2007, *The Observatory*, 127, 33
- Hilditch, R. W., Howarth, I. D., & Harries, T. J. 2005, *MNRAS*, 357, 304
- Howarth, I. D., Dufton, P. L., Dunstall, P. R., et al. 2015, *A&A*, 582, A73
- Hurley, J. R., Tout, C. A., & Pols, O. R. 2002, *MNRAS*, 329, 897
- Ibanoglu, C., Çakırlı, Ö., & Sipahi, E. 2013, *New A*, 25, 68
- Iglesias, C. A. & Rogers, F. J. 1996, *ApJ*, 464, 943
- Izzard, R. G., Dray, L. M., Karakas, A. I., Lugaro, M., & Tout, C. A. 2006, *A&A*, 460, 565
- Janssens, S., Shenar, T., Mahy, L., et al. 2021, *A&A*, 646, A33
- Johnston, C., Pavlovski, K., & Tkachenko, A. 2019, *A&A*, 628, A25
- Justesen, A. B. & Albrecht, S. 2021, *ApJ*, 912, 123
- Kippenhahn, R. & Weigert, A. 1990, *Stellar Structure and Evolution*
- Kobulnicky, H. A., Kiminki, D. C., Lundquist, M. J., et al. 2014, *ApJS*, 213, 34
- Köhler, K., Langer, N., de Koter, A., et al. 2015, *A&A*, 573, A71
- Kopal, Z. 1971, *PASP*, 83, 521
- Kruckow, M. U., Tauris, T. M., Langer, N., Kramer, M., & Izzard, R. G. 2018, *MNRAS*, 481, 1908
- Langer, N. 1991, *A&A*, 252, 669
- Langer, N. 1997, in *Astronomical Society of the Pacific Conference Series*, Vol. 120, *Luminous Blue Variables: Massive Stars in Transition*, ed. A. Nota & H. Lamers, 83
- Langer, N. 2012, *ARA&A*, 50, 107
- Langer, N., Schürmann, C., Stoll, K., et al. 2020, *A&A*, 638, A39
- Langer, N., Wellstein, S., & Petrovic, J. 2003a, in *IAU Symposium*, Vol. 212, *A Massive Star Odyssey: From Main Sequence to Supernova*, ed. K. van der Hucht, A. Herrero, & C. Esteban, 275
- Langer, N., Wellstein, S., & Petrovic, J. 2003b, in *IAU Symposium*, Vol. 212, *A Massive Star Odyssey: From Main Sequence to Supernova*, ed. K. van der Hucht, A. Herrero, & C. Esteban, 275
- Laplace, E., Göteborg, Y., de Mink, S. E., Justham, S., & Farmer, R. 2020, *A&A*, 637, A6
- Lorenz, R., Mayer, P., & Drechsel, H. 1994, *A&A*, 291, 185
- Lubow, S. H. & Shu, F. H. 1975, *ApJ*, 198, 383
- Maeder, A. & Meynet, G. 2000, *ARA&A*, 38, 143
- Mahy, L., Almeida, L. A., Sana, H., et al. 2020a, *A&A*, 634, A119
- Mahy, L., Martins, F., Machado, C., Donati, J. F., & Bouret, J. C. 2011, *A&A*, 533, A9
- Mahy, L., Sana, H., Abdul-Masih, M., et al. 2020b, *A&A*, 634, A118
- Malkov, O. Y. 2020, *MNRAS*, 491, 5489
- Mandel, I. & de Mink, S. E. 2016, *MNRAS*, 458, 2634
- Marchant, P. 2017, PhD thesis, University of Bonn, Germany
- Marchant, P., Langer, N., Podsiadlowski, P., Tauris, T. M., & Moriya, T. J. 2016, *A&A*, 588, A50
- Marchant, P., Pappas, K. M. W., Gallegos-Garcia, M., et al. 2021, *A&A*, 650, A107
- Martins, F., Mahy, L., & Hervé, A. 2017, *A&A*, 607, A82
- Massey, P. 1981, *ApJ*, 244, 157
- Massey, P., Penny, L. R., & Vukovich, J. 2002, *ApJ*, 565, 982
- McSwain, M. V., Huang, W., Gies, D. R., Grundstrom, E. D., & Townsend, R. H. D. 2008, *ApJ*, 672, 590
- Mennekens, N. & Vanbeveren, D. 2017, *A&A*, 599, A84
- Menon, A., Langer, N., de Mink, S. E., et al. 2021, *MNRAS*, 507, 5013
- Milone, A. P., Marino, A. F., Di Criscienzo, M., et al. 2018, *MNRAS*, 477, 2640
- Moe, M. & Di Stefano, R. 2017, *ApJS*, 230, 15
- Mokiem, M. R., de Koter, A., Vink, J. S., et al. 2007, *A&A*, 473, 603
- Morrison, N. D. & Conti, P. S. 1979, in *Mass Loss and Evolution of O-Type Stars*, ed. P. S. Conti & C. W. H. De Loore, Vol. 83, 277–280
- Negu, S. H. & Tessema, S. B. 2018, *Astronomische Nachrichten*, 339, 709
- Nelson, C. A. & Eggleton, P. P. 2001, *ApJ*, 552, 664
- Niemela, V. S. & Moffat, A. F. J. 1982, *ApJ*, 259, 213
- Ostrov, P. G., Lapasset, E., & Morrell, N. I. 2000, *A&A*, 356, 935
- Ostrov, P. G., Morrell, N. I., & Lapasset, E. 2001, *A&A*, 377, 972
- Packet, W. 1981, *A&A*, 102, 17
- Pavlovski, K., Southworth, J., & Tamajo, E. 2018, *MNRAS*, 481, 3129
- Pavlovskii, K., Ivanova, N., Belczynski, K., & Van, K. X. 2017, *MNRAS*, 465, 2092
- Paxton, B., Bildsten, L., Dotter, A., et al. 2011, *ApJS*, 192, 3
- Paxton, B., Cantiello, M., Arras, P., et al. 2013, *ApJS*, 208, 4
- Paxton, B., Marchant, P., Schwab, J., et al. 2015, *ApJS*, 220, 15
- Paxton, B., Schwab, J., Bauer, E. B., et al. 2018, *ApJS*, 234, 34
- Petrovic, J., Langer, N., & van der Hucht, K. A. 2005, *A&A*, 435, 1013
- Podsiadlowski, P., Joss, P. C., & Hsu, J. J. L. 1992, *ApJ*, 391, 246
- Pols, O. R. 1994, *A&A*, 290, 119
- Pols, O. R., Tout, C. A., Schröder, K.-P., Eggleton, P. P., & Manners, J. 1997, *MNRAS*, 289, 869
- Qin, Y., Marchant, P., Fragos, T., Meynet, G., & Kalogera, V. 2019, *ApJ*, 870, L18
- Quast, M., Langer, N., & Tauris, T. M. 2019, *A&A*, 628, A19
- Raucq, F., Rauw, G., Gosset, E., et al. 2016, *A&A*, 588, A10
- Rauw, G., Nazé, Y., & Campos, F. 2019, *A&A*, 627, A2
- Rauw, G., Vreux, J. M., & Bohannan, B. 1999, *ApJ*, 517, 416
- Ritchie, B. W., Clark, J. S., Negueruela, I., & Langer, N. 2010, *A&A*, 520, A48
- Salpeter, E. E. 1955, *ApJ*, 121, 161
- Sana, H., de Koter, A., de Mink, S. E., et al. 2013, *A&A*, 550, A107
- Sana, H., de Mink, S. E., de Koter, A., et al. 2012, *Science*, 337, 444

- Sanyal, D., Grassitelli, L., Langer, N., & Bestenlehner, J. M. 2015, *A&A*, 580, A20
- Sanyal, D., Langer, N., Szécsi, D., -C Yoon, S., & Grassitelli, L. 2017, *A&A*, 597, A71
- Schneider, F. R. N., Ohlmann, S. T., Podsiadlowski, P., et al. 2019, *Nature*, 574, 211
- Schneider, F. R. N., Podsiadlowski, P., Langer, N., Castro, N., & Fossati, L. 2016, *MNRAS*, 457, 2355
- Schootemeijer, A., Göteborg, Y., de Mink, S. E., Gies, D., & Zapartas, E. 2018, *A&A*, 615, A30
- Schootemeijer, A., Langer, N., Grin, N. J., & Wang, C. 2019, *A&A*, 625, A132
- Shenar, T., Gilkis, A., Vink, J. S., Sana, H., & Sander, A. A. C. 2020, *A&A*, 634, A79
- Soberman, G. E., Phinney, E. S., & van den Heuvel, E. P. J. 1997, *A&A*, 327, 620
- Southworth, J., Maxted, P. F. L., & Smalley, B. 2004, *MNRAS*, 351, 1277
- Spera, M., Mapelli, M., Giacobbo, N., et al. 2019, *MNRAS*, 485, 889
- Stanway, E. R., Eldridge, J. J., & Chrimes, A. A. 2020, *MNRAS*, 497, 2201
- Stevenson, S., Vigna-Gómez, A., Mandel, I., et al. 2017, *Nature Communications*, 8, 14906
- Stickland, D. J., Lloyd, C., Pachoulakis, I., & Koch, R. H. 1998, *The Observatory*, 118, 356
- Surina, F. & Kang, Y. W. 2009, *Astronomical Society of the Pacific Conference Series*, Vol. 404, *Absolute Dimensions of Four Eclipsing Binaries*, ed. S. J. Murphy & M. S. Bessell, 178
- Surkova, L. P. & Svechnikov, M. A. 2004, *VizieR Online Data Catalog*
- Takahashi, K. & Langer, N. 2021, *A&A*, 646, A19
- Tauris, T. M. & van den Heuvel, E. P. J. 2006, *Formation and evolution of compact stellar X-ray sources*, Vol. 39, 623–665
- Terrell, D., Munari, U., Zwitter, T., & Wolf, G. 2005, *MNRAS*, 360, 583
- Tomkin, J., Lambert, D. L., & Lemke, M. 1993, *MNRAS*, 265, 581
- Torres, G., Andersen, J., & Giménez, A. 2010, *A&A Rev.*, 18, 67
- Tout, C. A., Aarseth, S. J., Pols, O. R., & Eggleton, P. P. 1997, *MNRAS*, 291, 732
- Tüysüz, M., Soyduğan, F., Bilir, S., et al. 2014, *New A*, 28, 44
- Ulrich, R. K. & Burger, H. L. 1976, *ApJ*, 206, 509
- Valsecchi, F., Glebbeek, E., Farr, W. M., et al. 2010, *Nature*, 468, 77
- Van Bever, J. & Vanbeveren, D. 2000, *A&A*, 358, 462
- van der Hucht, K. A. 2001, *New A Rev.*, 45, 135
- van Rensbergen, W., De Greve, J. P., Mennekens, N., Jansen, K., & De Loore, C. 2010, *A&A*, 510, A13
- Vanbeveren, D., De Loore, C., & Van Rensbergen, W. 1998, *A&A Rev.*, 9, 63
- Villaseñor, J. I., Taylor, W. D., Evans, C. J., et al. 2021, *MNRAS*, 507, 5348
- Walker, W. S. G., Blackford, M., Butland, R., & Budding, E. 2017, *MNRAS*, 470, 2007
- Walter, R., Lutovinov, A. A., Bozzo, E., & Tsygankov, S. S. 2015, *A&A Rev.*, 23, 2
- Wang, C., Langer, N., Schootemeijer, A., et al. 2020, *ApJ*, 888, L12
- Wang, J., Song, H., & Li, Z. 2017, *Science China Physics, Mechanics, and Astronomy*, 60, 59521
- Wang, L., Gies, D. R., Peters, G. J., et al. 2021, *AJ*, 161, 248
- Wellstein, S. & Langer, N. 1999, *A&A*, 350, 148
- Wellstein, S., Langer, N., & Braun, H. 2001, *A&A*, 369, 939
- Williams, S. J., Gies, D. R., Henry, T. J., et al. 2008, *ApJ*, 682, 492
- Wilson, R. E., van Hamme, W., & Petter, L. 1985, *ApJ*, 289, 748
- Yaşarsoy, B. & Yakut, K. 2014, *New A*, 31, 32
- Yoon, S.-C., Dessart, L., & Clocchiatti, A. 2017, *ApJ*, 840, 10
- Yoon, S. C., Woosley, S. E., & Langer, N. 2010, *ApJ*, 725, 940
- Zahn, J. P. 1977, *A&A*, 500, 121



## Appendix A: Discussion and uncertainties

### Appendix A.1: Envelope inflation

Sanyal et al. (2015) investigated the single star models of Brott et al. (2011a) at LMC metallicity and found that models exceeding  $\sim 40 M_{\odot}$  reach their Eddington limit inside the stellar envelope during core hydrogen burning. This leads to a large expansion of the stellar envelope, which makes the star grow to red supergiant proportions during core hydrogen burning. Our models, with very similar physics assumptions as those of Brott et al. (2011a), are also expected to show similar behaviour. Indeed, for the next higher initial donor mass to be considered ( $44.7 M_{\odot}$ ), the envelope of the donor inflates and leads to unstable mass transfer which MESA is unable to calculate through. In this sense, the upper limit on the initial donor mass in our grid is a computational result. For a more comprehensive discussion of this topic, we refer the interested readers to sect. 4.1 of Langer et al. (2020). We discuss the parts relevant to our work.

The implication of inflation above  $\sim 40 M_{\odot}$  at the LMC metallicity is that all binary models having initial donor masses above  $\sim 40 M_{\odot}$  will undergo Case A mass transfer since the donors will expand to red supergiant proportions during core hydrogen burning. Such donors have inflated convective envelopes at the onset of Roche-lobe overflow (Sanyal et al. 2015). The subsequent mass transfer due to Roche-lobe overflow from stars with convective envelopes is expected to be unstable as the radius of a star with convective envelope increases when mass is lost from the envelope (Quast et al. 2019; Ge et al. 2020). Langer et al. (2020) assume that, in the absence of detailed model calculations, mass transfer due to Roche-lobe overflow from an inflated mass donor will lead to an unstable mass transfer and the binary would merge.

Due to inflation and the inability of MESA to calculate through the mass transfer phase of such models, our models cannot predict the observable properties of binary systems in semi-detached configurations originating from initial donor masses greater than  $\sim 40 M_{\odot}$ . In the TMBM sample of semi-detached systems, we find a system VFTS 094 in which both components have masses around  $\sim 30 M_{\odot}$ . This might be an observed system which shows evidence of stable mass transfer during fast Case A when the mass of the donor was arguably greater than  $\sim 40 M_{\odot}$ . However, the error bars are too big to draw any conclusive arguments. The system VFTS 450 also shows that both components have high dynamical masses  $\sim 30 M_{\odot}$  and is a possible candidate to have undergone stable mass transfer above the cut-off mass for inflation to set in our models.

We find another system LH 54-425 (Williams et al. 2008) in which the more massive component is estimated to have a mass of  $\sim 47 \pm 2 M_{\odot}$ . The binary system R136-38 (Massey et al. 2002) is estimated to have a star with mass  $\sim 56.9 \pm 0.6 M_{\odot}$ . We note that the 04f + 06V eclipsing binary system Sk—67°105 is found to have one component which has mass greater than  $40 M_{\odot}$ , and both the components are nearly filling their Roche lobe. The existence of these observed high mass systems provides a motivation for a comprehensive investigation of the mass transfer phase in mass donors with inflated envelopes.

However, we note that inflation at LMC metallicity sets in at  $40 M_{\odot}$  during the late stage of core hydrogen burning and the estimated age of LH 54-425 and R136 is 1.5-2 Myrs. Hence, these systems might not have inflated yet. On the other hand, the authors that studied Sk—67°105 reported that it is in a very distorted configuration and is likely that its components are undergoing very strong interactions.

If inflated stars do undergo stable mass transfer in nature, then the orbital period distribution of our semi-detached models can be taken as skewed to lower periods. However, the initial mass function and the empirical determination of the distribution of orbital periods in binaries are heavily weighted towards lower masses and orbital periods. Moreover, the time spent in Case A mass transfer phase decreases with the increase in the initial orbital period of the binary. Hence, we do not expect a significant impact on the predicted orbital period distributions as a whole. However, the properties of very massive binaries ( $> \sim 30 M_{\odot}$ ) in the Algol configuration can be quite different than comparatively lower mass Algol binaries (see for eg. Fig. 5).

### Appendix A.2: Mass transfer efficiency and stability of mass transfer

Observations of binary systems which have undergone a mass transfer phase indicate that the mass transfer efficiency varies from binary to binary. While some binaries require models to have low mass transfer efficiency (Langer et al. 2003b), others indicate a need for higher mass transfer efficiency (Wellstein & Langer 1999). It has also been argued that binaries with lower mass ratio experience lower mass transfer efficiency (Petrovic et al. 2005). de Mink et al. (2007) also find hints for a low mass transfer efficiency for higher period binaries. However, a recent study by Deschamps et al. (2015) reported that direct observational imprints of mass loss due to non-conservative mass transfer might not be visible in Algol systems.

Our mass transfer model based on the principle of decreasing mass transfer efficiency with increasing rotation of the mass accreting star does in theory take into consideration these variations and we do see a trend of decreasing mass transfer efficiency with increasing period and decreasing mass ratios. This model needs excess mass to be removed from the binary so that the mass gainer does not exceed critical rotation. We model this by requiring that the combined photon energy from both the stars in the binary is larger than the gravitational energy needed to remove the excess unaccretable mass due to the accretor reaching critical rotation. If this condition fails, the evolution of the model is stopped and assumed to merge. However, as already demonstrated, our mass transfer scheme is able to reproduce the observed population of Algol binaries in the Galaxy and LMC.

Our criterion to determine the stability of mass transfer is simple. The dividing line between stable and unstable mass transfer in our models is a function of the initial orbital period and mass ratio for a particular initial donor mass of the binary. For a discussion, we direct the interested reader to fig. 2 of Langer et al. (2020).

Wang et al. (2020) has shown that a large fraction of the Be star population in NGC 330 (Milone et al. 2018) is well represented by binary evolution models. To correctly predict their numbers in comparison to the number of mergers, however, they posit that the boundary between stable and unstable mass transfer has to be relaxed such that there are more models that can undergo stable mass transfer. Doing such would increase the number of Case A mass transfer systems with lower initial mass ratios. Inspection of our model grid shows that the time spent in the semi-detached phase decreases with lower mass ratios, such that models having initial mass ratio less than 0.5 spend less than 10% of their main sequence lifetime in the semi-detached phase. Hence, relaxing the criterion for stable mass transfer will not significantly affect the results we derive in this work.

### Appendix A.3: Semiconvection

We are aware that recent studies on single star models (Schootemeijer et al. 2019) argue for a higher efficiency of semiconvection in stellar models. We note that a higher semiconvective efficiency than what is implemented in our models will make the mass gaining stars rejuvenate (Braun & Langer 1995) and develop a core-envelope structure similar to that of a single star (Braun & Langer 1995). The core mass and stellar radius of rejuvenated accretors will be larger and smaller, respectively, compared to our nonrejuvenated models (compare model 47 and 48 of Wellstein et al. 2001). This implies that our binary models enter into a contact configuration and can undergo L2 overflow (purple models in Fig. 1) at longer orbital periods compared to models calculated with a higher semiconvective efficiency, due to the larger radii of our accretors (compare Fig. 1 to Fig. A1 of Menon et al. 2021).

Rejuvenated accretors also have a greater remaining core hydrogen burning lifetime than nonrejuvenated accretors. Accordingly, our binary models are more likely to undergo inverse mass transfer from a post main sequence accretor onto a main sequence donor (orange models in Fig. 1 than binary models calculated using a high semiconvective efficiency. After Case AB mass transfer, our nonrejuvenated accretors may live their core helium burning lifetime as a blue supergiant instead of a red supergiant (Podsiadlowski et al. 1992). However, the amount of increase in the core masses of mass gainers due to rejuvenation depends on the amount of mass that can be successfully accreted (Braun & Langer 1995). We showed that the mass transfer efficiency is low in most of our models that survive the Case A mass transfer phase (Fig. 3).

From the above discussion, we can speculate that more short period binaries will contribute to our predicted Algol population for models with efficient semiconvection. As such, the peak in the predicted orbital period distribution may be shifted to a lower value, although we cannot quantify it. The maximum lifespan of the slow Case A phase is also expected to increase since fewer models will merge due to L2 overflow during slow Case A mass transfer. This may increase our predicted number of Algol binaries in the LMC. As less binaries will undergo contact and inverse slow Case A mass transfer, the peak in the predicted surface abundance is also expected to increase to higher values, especially the nitrogen surface enhancement. Since shorter period binaries undergo more conservative Case A mass transfer in our mass transfer scheme, we expect more contribution from models that undergo conservative mass transfer to the population of WR/He+OB star binaries.

### Appendix B: Additional figures for surface abundances during slow Case A

Here, we show the prediction of surface helium mass fraction and surface nitrogen mass fraction enhancement for only the models that survive the Case A mass transfer phase (Fig. B.1) or only for models that merge during the Case A mass transfer (Fig. B.1). We also provide additional figures of the surface helium mass fraction and nitrogen mass fraction enhancement of donors and accretors during the slow Case A mass transfer phase, for different ranges of accretor masses of the binary during the semi-detached configuration (Fig. B.2).

### Appendix C: Mass dependence of orbital period and mass ratio during slow Case A

Here, we provide additional figures of the orbital period and mass ratio during the slow Case A mass transfer phase, for different ranges of accretor masses of the binary.

### Appendix D: Orbital velocities

Figure D.1 shows the probability distribution of the orbital velocities of the two components during the semi-detached phase. In the darker shaded regions, we see that the donor has a higher orbital velocity than the accretor. This indicates that the donor is currently the less massive component of the system.

### Appendix E: Orbital period derivatives

Figure E.1 shows the orbital period derivatives during the semi-detached phase for different ranges of initial donor masses.

### Appendix F: Summary of the outcome of binary models for different initial donor masses in our grid

We present the summary plots for different initial donor masses in our grid. Our work is mainly focussed on the systems that survive the Case A mass transfer phase (light blue models) or undergo an extended phase of interaction (orange and purple models) before merging on the main sequence (Fig. F.1).

### Appendix G: Binary properties after Case AB mass transfer

Here, we show the binary properties of post Case AB models when the central helium mass fraction of the donor is 0.10.

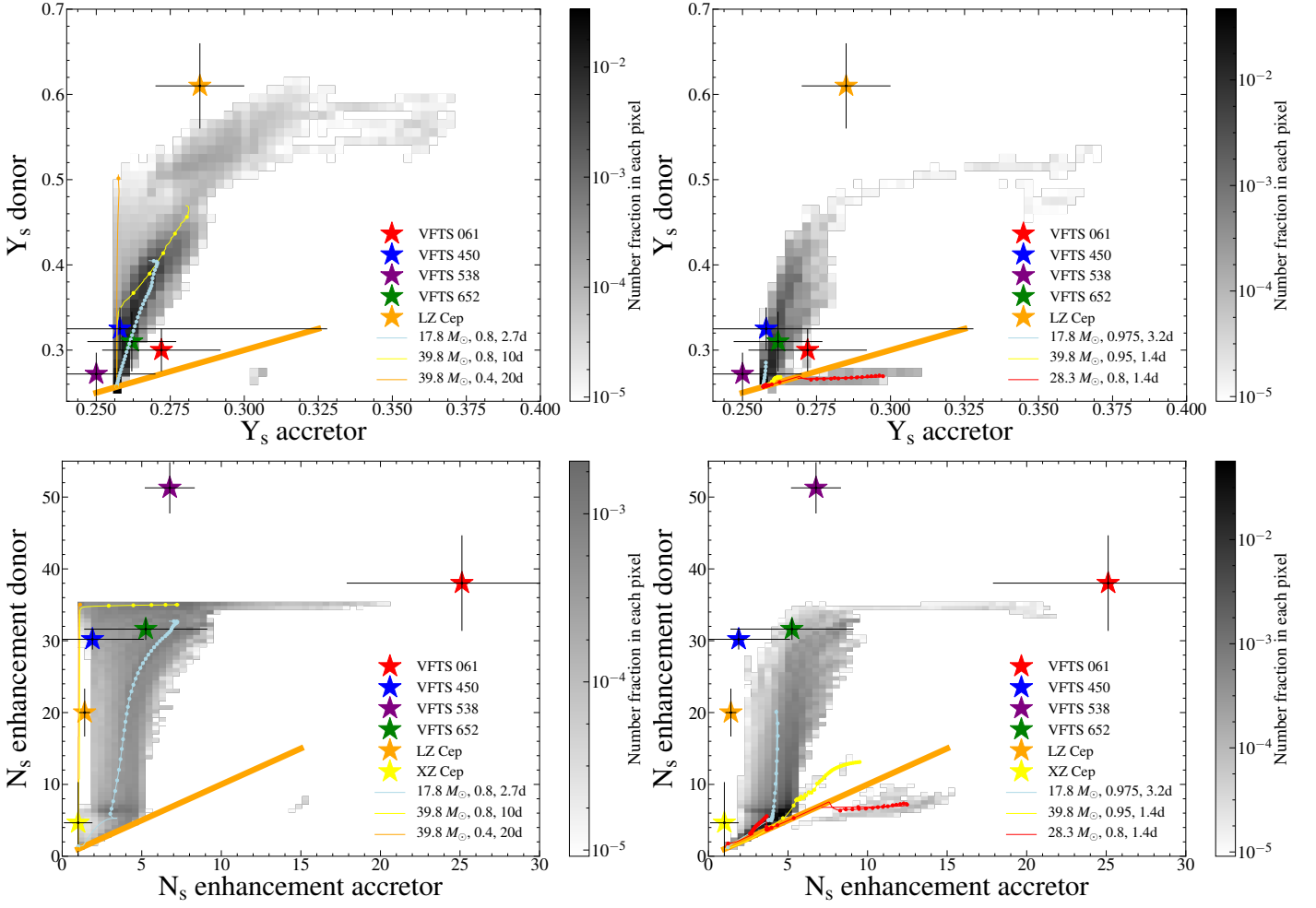


**Fig. B.1.** Probability distribution of the surface helium mass fraction (top panels) and surface nitrogen mass fraction enhancement (bottom panels) of donor vs the accretor that is predicted to be observed in the semi-detached configuration of the Case A mass transfer phase. The left panels show the contribution to Fig. 7 from models that survive the Case A mass transfer phase while the right panels show the contribution to Fig. 7 from models that eventually merge during the slow Case A phase. The different coloured ‘stars’ with error bars denote the position of the semi-detached systems of the TMBM survey (Mahy et al. 2020b) and Galaxy. The thick orange line indicates where the surface helium mass fraction or surface nitrogen enrichment of the donor and accretor is the same. The thin coloured lines show the evolution of surface abundances during the main sequence with initial parameters (donor mass, mass ratio, period) as given in the legend. The corresponding coloured dots are at 50000 years during the semi-detached phase. The grey-scale gives the probability fraction in each pixel. The total probability is normalised such that the integrated sum over the entire area is 1.

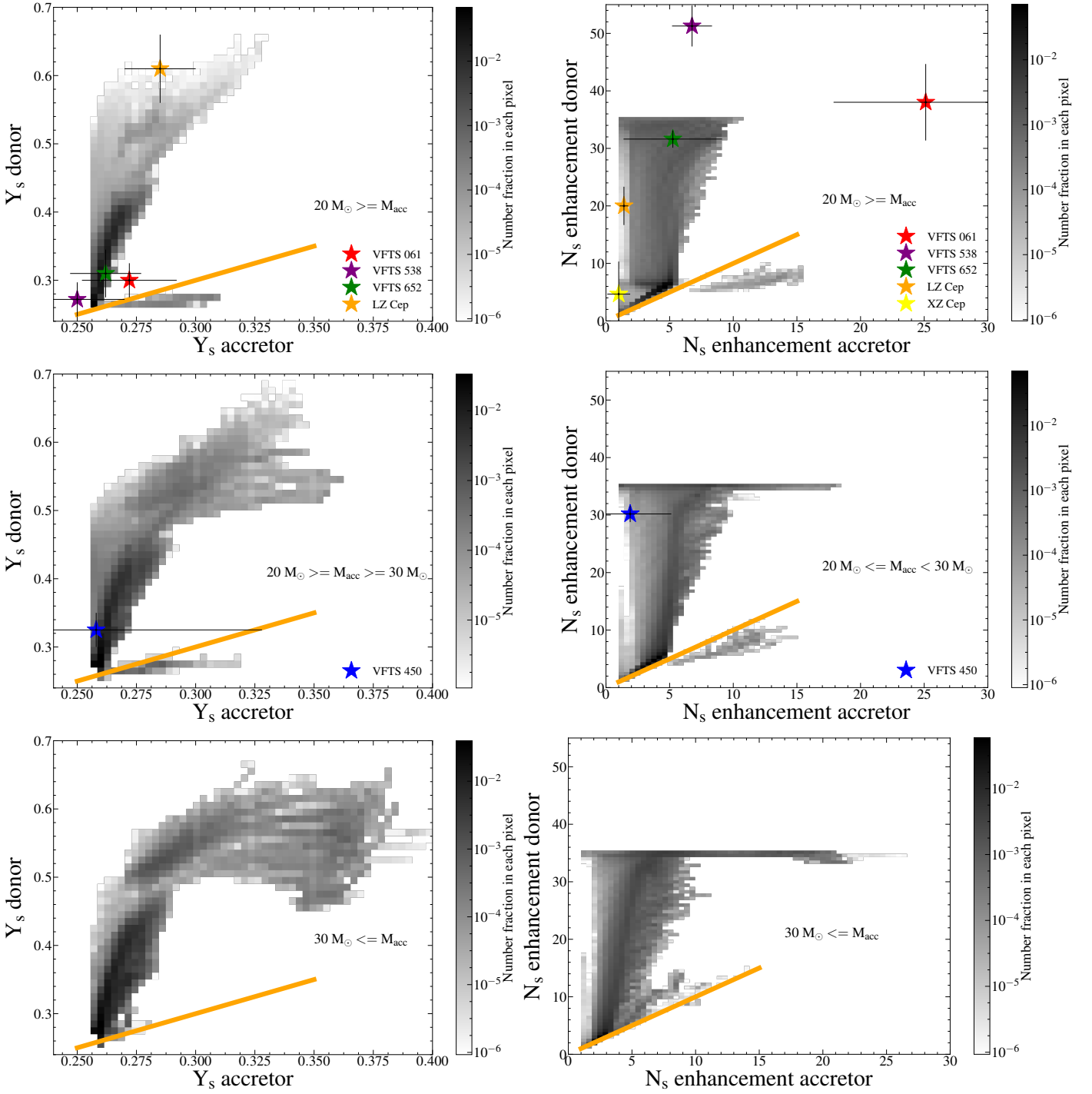


**Fig. B.2.** Probability distribution of the surface helium mass fraction (left three panels) and surface nitrogen mass fraction enhancement factors (right three panels) of the donor vs the accretor for different ranges of accretor masses during the semi-detached phase: below  $20 M_{\odot}$  (top panels),  $20\text{--}30 M_{\odot}$  (middle panels) and above  $30 M_{\odot}$  (bottom panels). The different coloured stars symbols with error bars denote the positions of the semi-detached systems from the TMBM survey (Mahy et al. 2020a,b). The orange line indicates where the donor and accretor abundances are the same. The grey-scale gives the probability fraction in each pixel. The total probability is normalised such that the sum over the entire area equals unity.

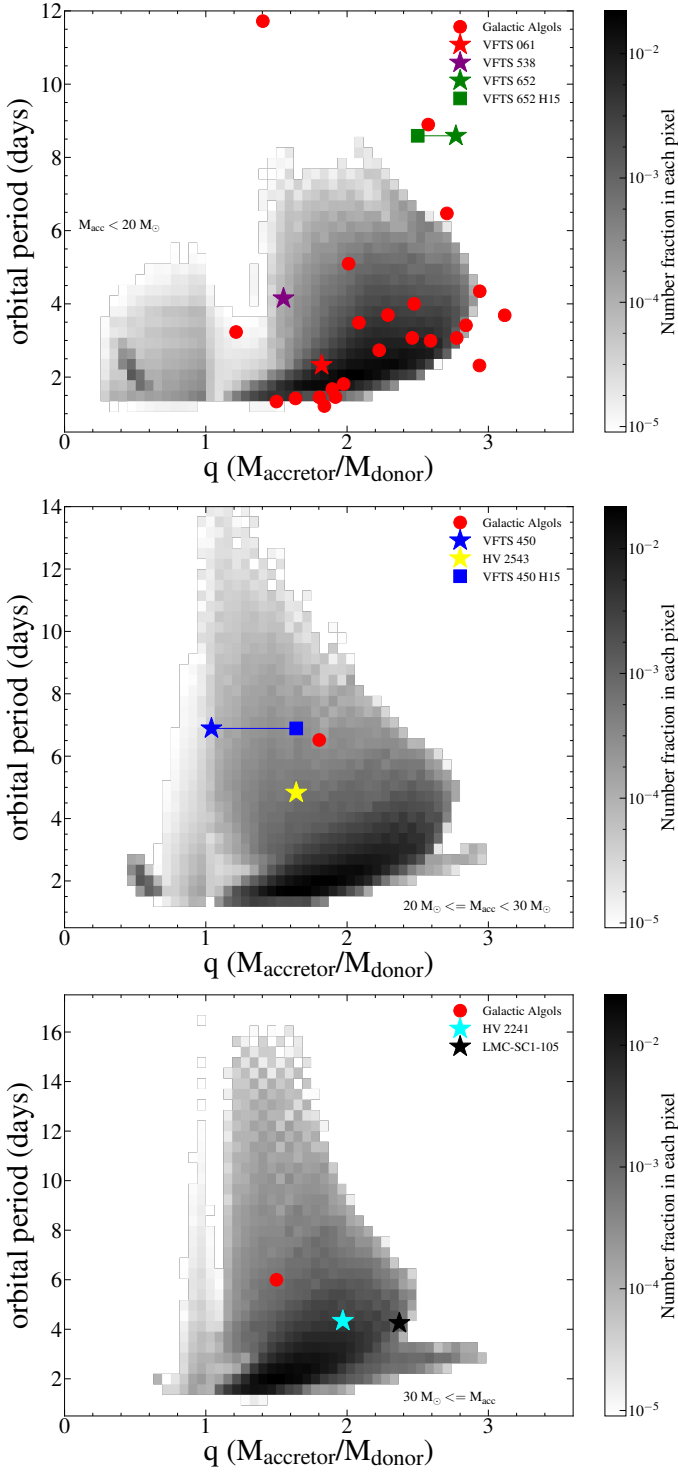


**Fig. C.1.** Probability distribution of the orbital period and mass ratio that is predicted to be observed in the semi-detached configuration of the Case A mass transfer phase for models with accretor mass below  $20 M_{\odot}$  (top panel),  $20\text{--}30 M_{\odot}$  (middle panel) and above  $30 M_{\odot}$  (bottom panel). The grey-scale gives the probability fraction in each pixel. The total probability is normalised such that the sum over the entire area is 1.

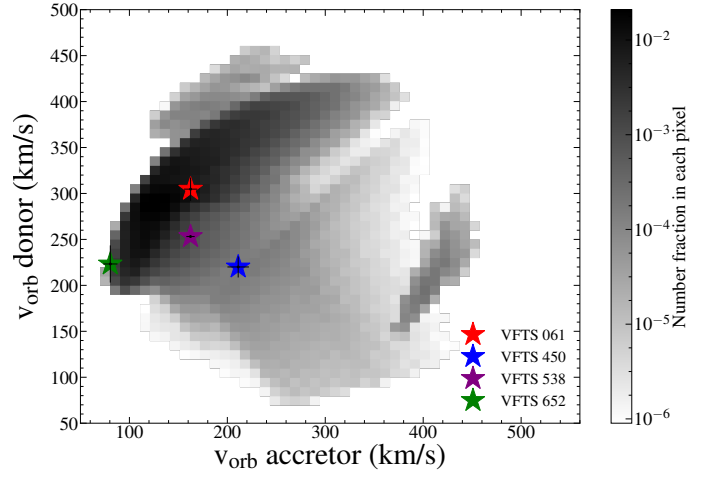


**Fig. D.1.** Probability distribution of the orbital velocities of the donor and the accretor in the semi-detached configuration. The different coloured stars with error bars denote the position of the semi-detached systems of the TMBM survey (Almeida et al. 2017). Grey-scale: See description in Fig. 7.

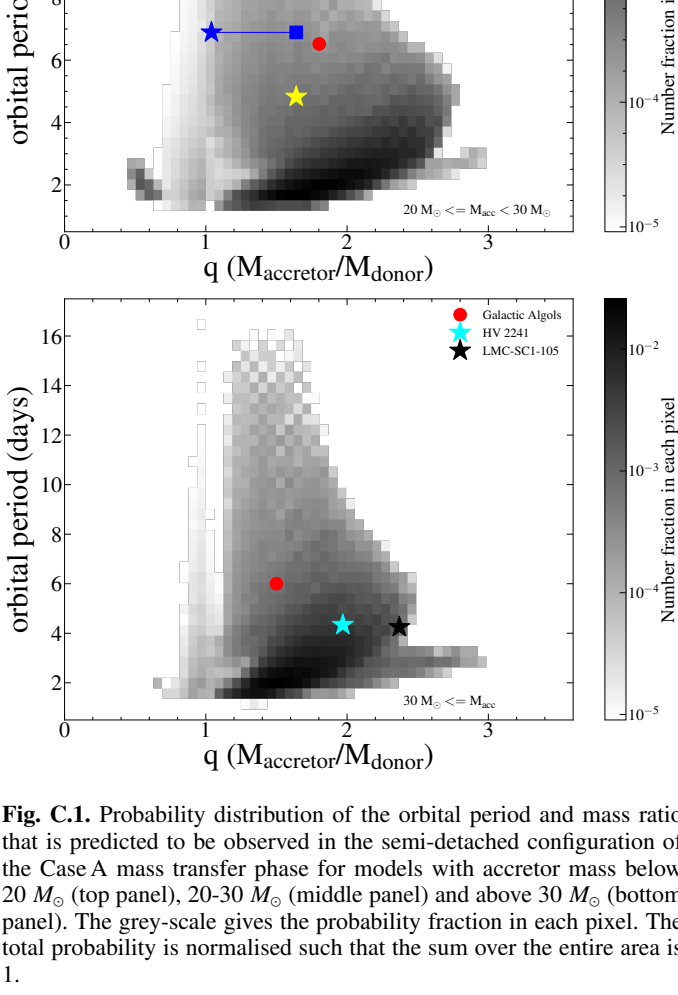


**Fig. E.1.** Same as Fig. 10, but only for initial donor mass of  $10\text{--}15 M_{\odot}$  (top panel) and  $30\text{--}40 M_{\odot}$  (bottom panel).

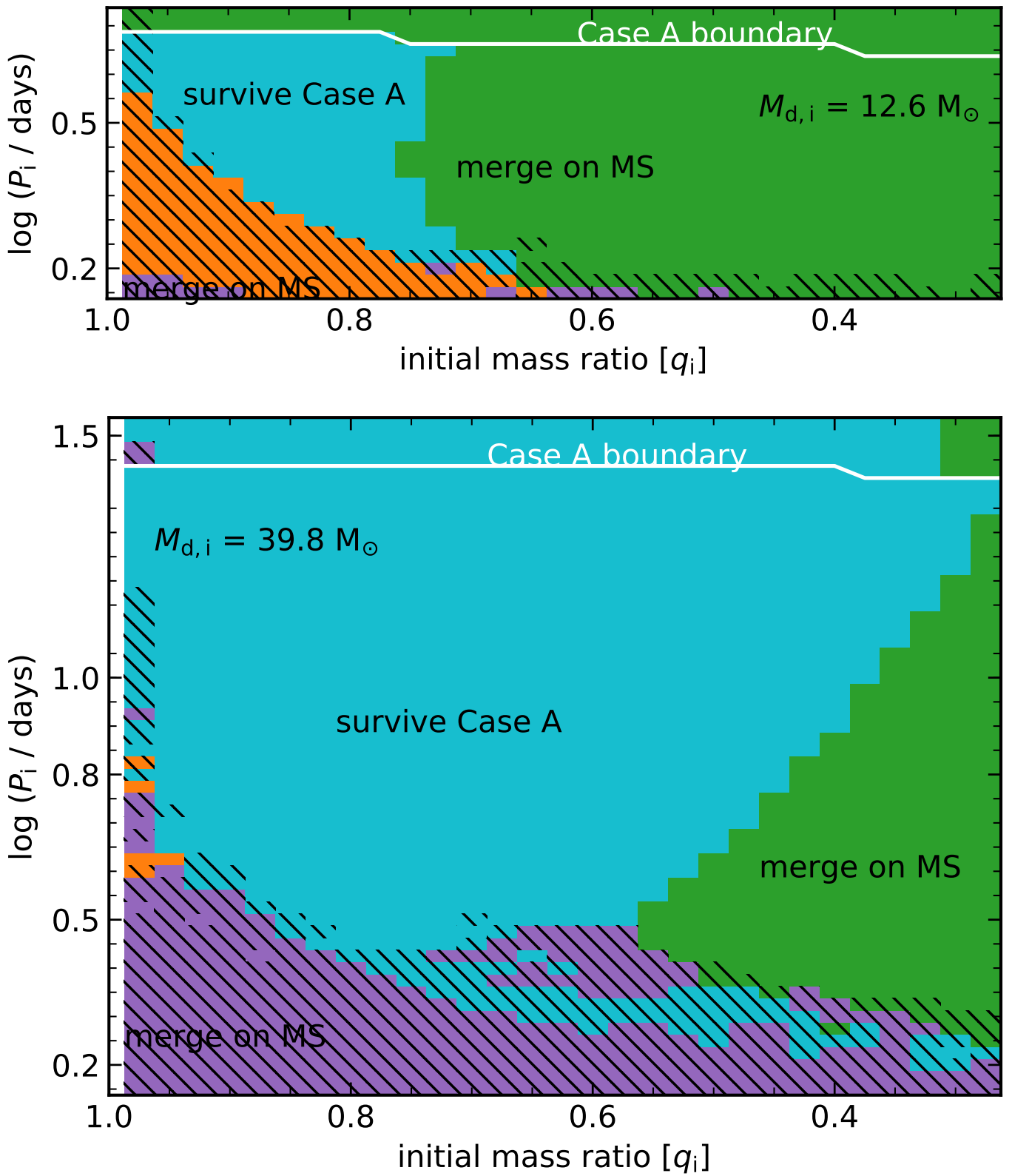


**Fig. F1.** Summary plot, same as Fig. 1, but for an initial donor mass of  $M \approx 12.6 M_\odot$  (top plot) and  $M \approx 39.8 M_\odot$  (bottom plot).

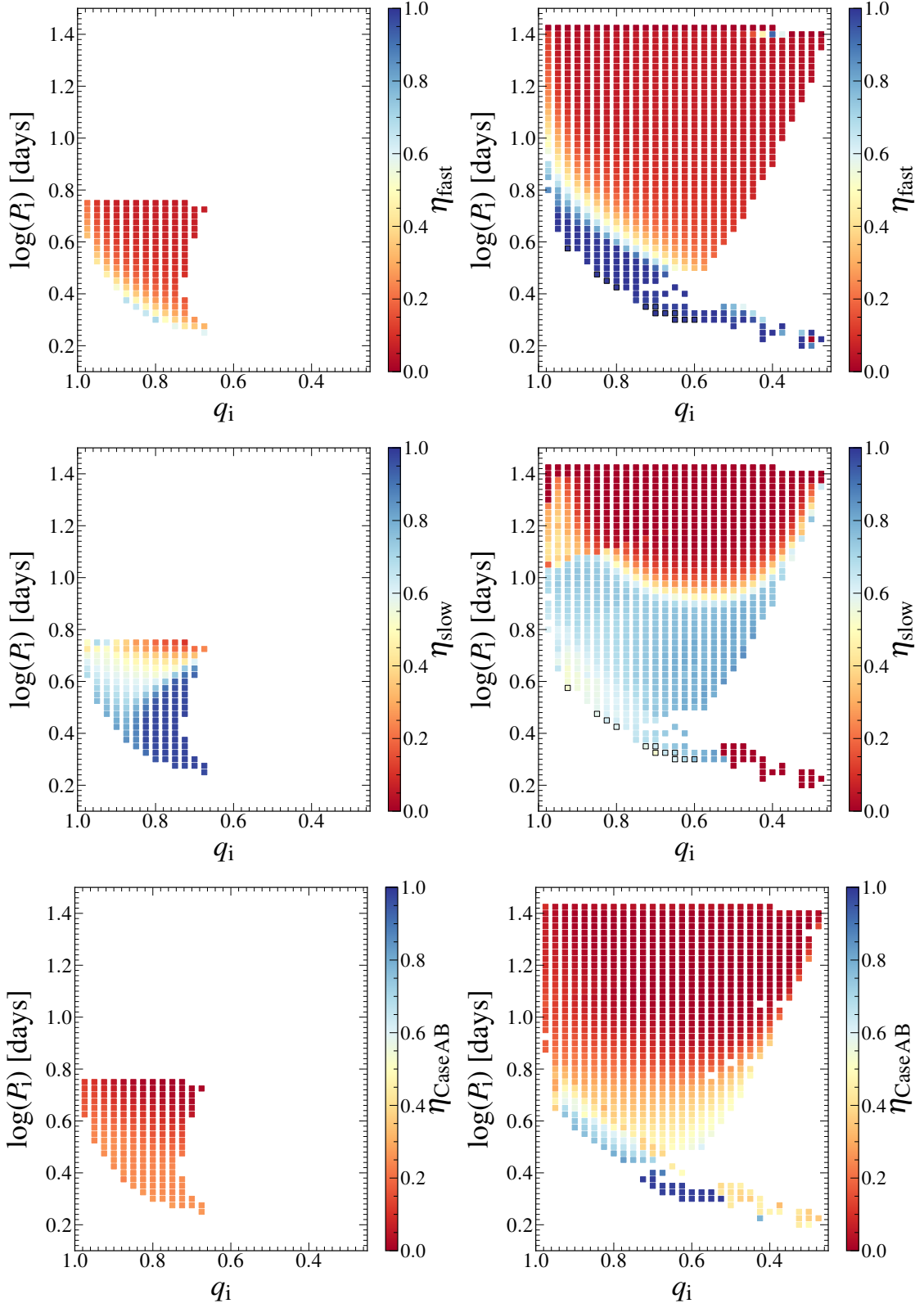


**Fig. F.2.** Mass transfer efficiency  $\eta$  (colour coded) during fast (top panels) and slow (middle panels) Case A, and during Case AB (bottom panels) as function of initial orbital period and initial mass ratio, for systems with initial donor masses of  $\sim 16 M_{\odot}$  and  $\sim 40 M_{\odot}$  in the left and right panels, respectively. Each coloured square represents one binary evolution model, with the colour denoting the mass transfer efficiency. Black frames around coloured square indicate models that has undergone a contact phase lasting more than three thermal timescales of the mass donor.

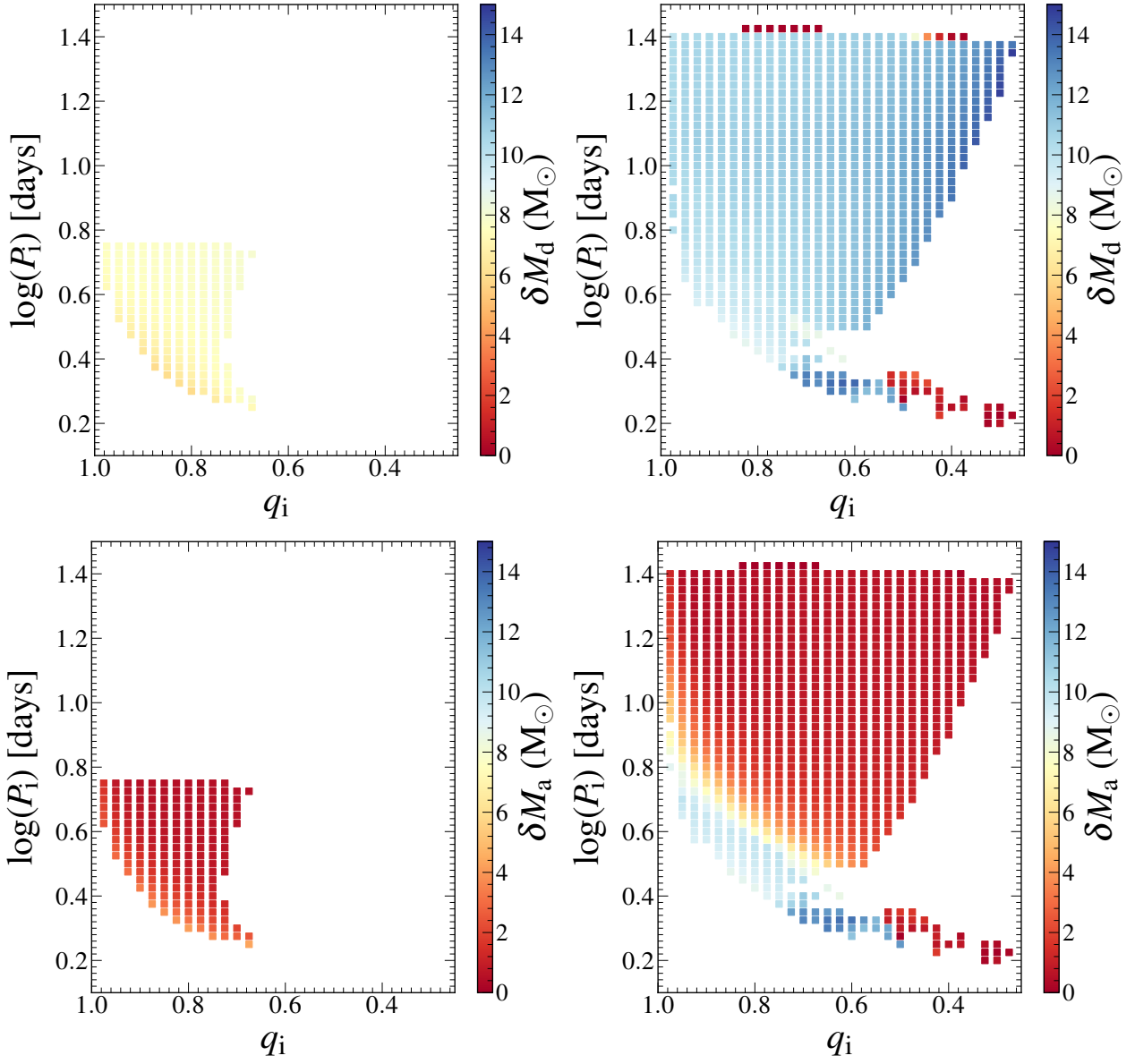


**Fig. F.3.** Amount of mass lost by the donor stars  $\delta M_d$  (top panels) and gained by the accretor  $\delta M_a$  (bottom panels) during fast Case A mass transfer phase, for systems with initial donor masses of  $\sim 16 M_\odot$  and  $\sim 40 M_\odot$  in the left and right panels, respectively.



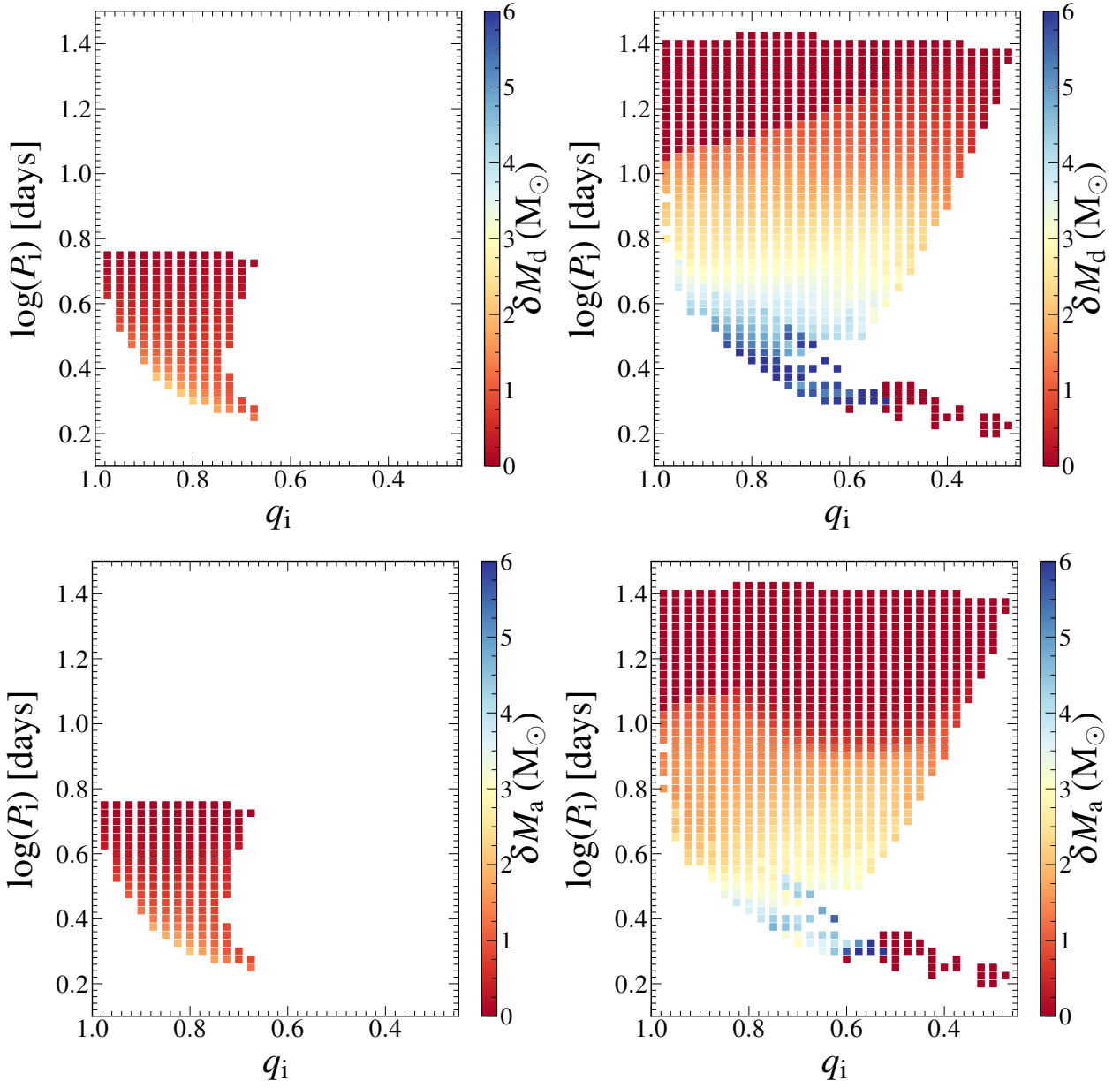


**Fig. F.4.** Amount of mass lost by the donor stars  $\delta M_d$  (top panels) and gained by the accretor  $\delta M_a$  (bottom panels) during slow Case A mass transfer phase, for systems with initial donor masses of  $\sim 16 M_\odot$  and  $\sim 40 M_\odot$  in the left and right panels, respectively.

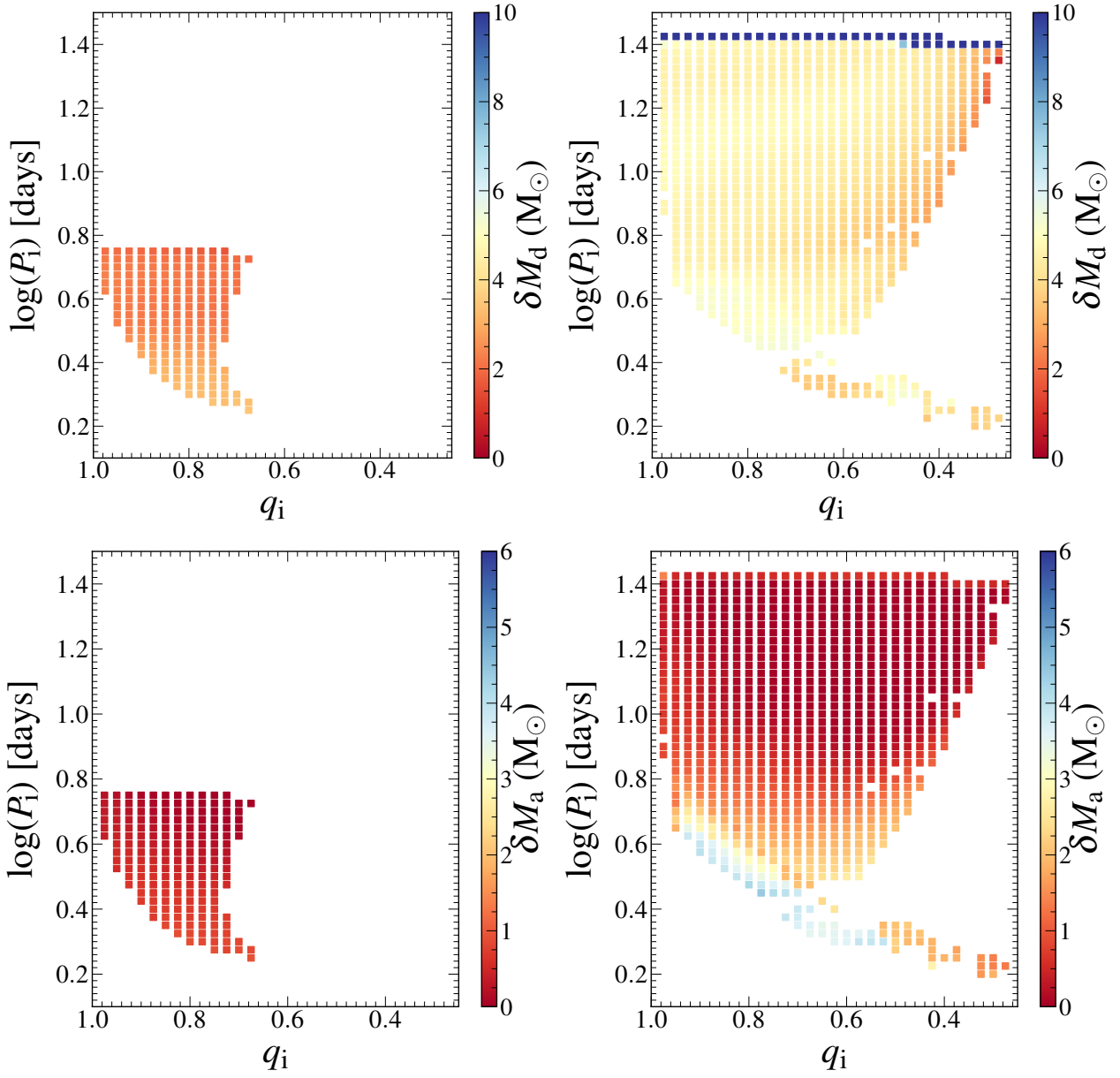


**Fig. F.5.** Amount of mass lost by the donor stars  $\delta M_d$  (top panels) and gained by the accretor  $\delta M_a$  (bottom panels) during Case AB mass transfer phase, for systems with initial donor masses of  $\sim 16 M_\odot$  and  $\sim 40 M_\odot$  in the left and right panels, respectively.

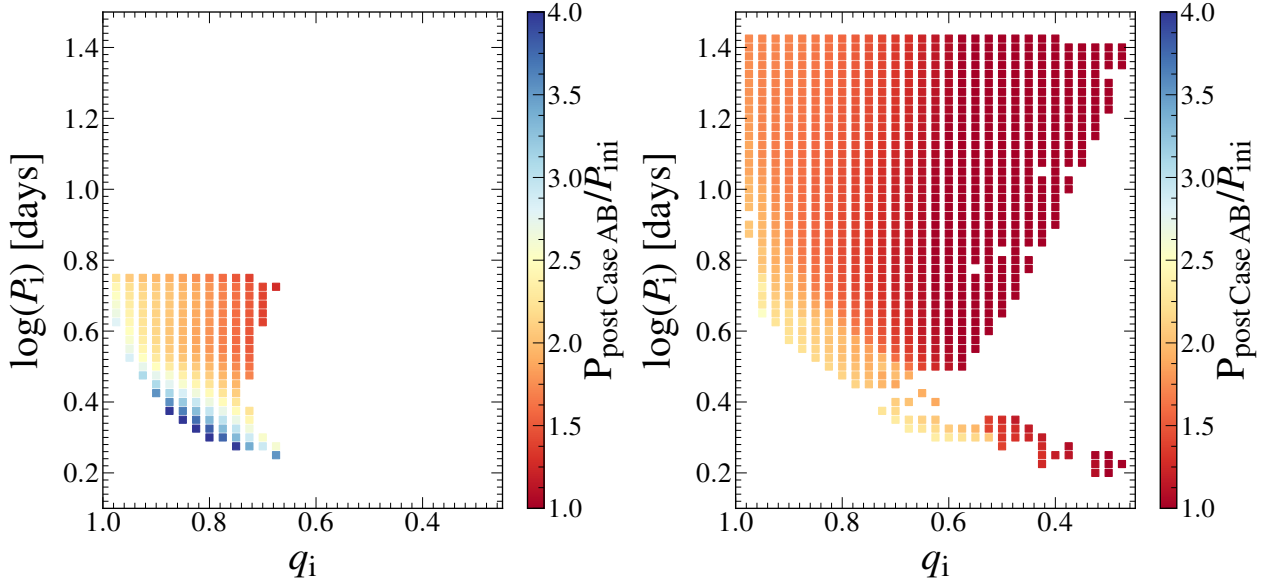


**Fig. F.6.** Ratio of the binary orbital period after Case AB mass transfer phase to the initial orbital period (colour coded) as function of initial orbital period and initial mass ratio, for systems with initial donor masses of  $\sim 16 M_{\odot}$  and  $\sim 40 M_{\odot}$  in the left and right panels, respectively.

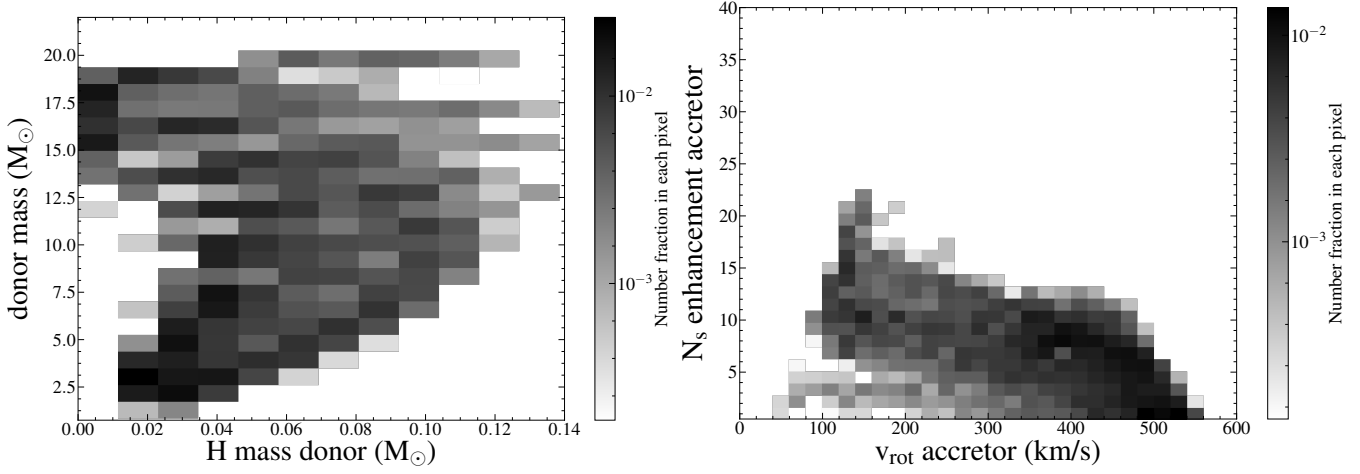


**Fig. G.1.** Probability density distribution the leftover hydrogen mass vs total stellar mass of the donor (left panel) and of the surface nitrogen mass fraction enhancement and rotational velocity for the mass gainer, for our binary models after the Case AB mass transfer phase. In contrast to Fig. 11, which depicts the same models at a time where the central helium mass fraction of the donors is 0.9, here we display the information for a donor central helium mass fraction of 0.1.